

Thin films of lithium ion conducting garnets and their properties

dem Fachbereich Biologie und Chemie
der Justus-Liebig-Universität Gießen

vorgelegte
Dissertation
zur Erlangung des Grades
Doktor der Naturwissenschaften
– Dr. rer. nat. –

von

Jochen Reinacher

geboren am 07.09.1984

Gießen 2014

Dekan / Dean	Prof. Dr. Holger Zorn
1. Gutachter / Reviewer	Prof. Dr. Jürgen Janek
2. Gutachter / Reviewer	Prof. Dr. Bruno K. Meyer

Arbeit eingereicht:	10.06.2014
---------------------	------------

Tag der mündlichen Prüfung:	11.07.2014
-----------------------------	------------

Abstract

Different lithium ion conducting garnet-type thin films were prepared by pulsed laser deposition. Of these garnet-type thin films $\text{Li}_6\text{BaLa}_2\text{Ta}_2\text{O}_{12}$, cubic $\text{Li}_{6.5}\text{La}_3\text{Zr}_{1.5}\text{Ta}_{0.5}\text{O}_{12}$ (additionally stabilized by Al_2O_3) and cubic $\text{Li}_7\text{La}_3\text{Zr}_2\text{O}_{12}$ stabilized by Ga_2O_3 were investigated in more detail. Conductivity measurements of these thin films performed in lateral geometry showed total conductivities of $\sigma = 1.7 \cdot 10^{-6} \text{ S} \cdot \text{cm}^{-1}$, $\sigma = 2.9 \cdot 10^{-6} \text{ S} \cdot \text{cm}^{-1}$ and $\sigma = 1.2 \cdot 10^{-6} \text{ S} \cdot \text{cm}^{-1}$, respectively. Electrochemical impedance spectroscopy was performed in axial geometry (orthogonal to the substrate), revealing conductivities of $\sigma = 3.3 \cdot 10^{-5} \text{ S} \cdot \text{cm}^{-1}$ for $\text{Li}_6\text{BaLa}_2\text{Ta}_2\text{O}_{12}$ which is comparable to the bulk conductivity of $\text{Li}_6\text{BaLa}_2\text{Ta}_2\text{O}_{12}$ ($\sigma = 4 \cdot 10^{-5} \text{ S} \cdot \text{cm}^{-1}$). The comparatively low lateral conductivity of the garnet-type material could be increased to a maximum of $\sigma = 2.8 \cdot 10^{-5} \text{ S} \cdot \text{cm}^{-1}$ for multilayer structures of two different alternating garnet-type materials ($\text{Li}_{6.5}\text{La}_3\text{Zr}_{1.5}\text{Ta}_{0.5}\text{O}_{12}:\text{Al}_2\text{O}_3$, $\text{Li}_7\text{La}_3\text{Zr}_2\text{O}_{12}:\text{Ga}_2\text{O}_3$). These investigations revealed a strong influence of the thin film microstructure on the total conductivity. Additionally the electronic partial conductivity of $\text{Li}_6\text{BaLa}_2\text{Ta}_2\text{O}_{12}$ as bulk and thin film material was determined. The garnet-type thin films were successfully tested as protective coatings and as ion-selective membranes in “hybrid battery cells” (liquid and solid electrolyte combined in one cell). The ion-selective membranes successfully suppressed the undesired polysulfide shuttle mechanism inside a lithium sulfur battery.

Keywords:

Lithium solid electrolyte, garnet, separator, solid state battery, hybrid battery, PLD

Zusammenfassung

Eine Reihe unterschiedlicher Lithium-ionenleitender Dünnschichten aus Oxiden vom Granat-Typ wurde mittels gepulster Laserdeposition abgeschieden. Hervorzuheben sind die Präparation von $\text{Li}_6\text{BaLa}_2\text{Ta}_2\text{O}_{12}$, kubischem $\text{Li}_{6,5}\text{La}_3\text{Zr}_{1,5}\text{Ta}_{0,5}\text{O}_{12}$, welches zusätzlich durch Al_2O_3 stabilisiert wurde, und kubischem $\text{Li}_7\text{La}_3\text{Zr}_2\text{O}_{12}$, stabilisiert durch Ga_2O_3 . Leitfähigkeitsmessungen in lateraler Geometrie ergaben für diese Materialien jeweils Gesamtleitfähigkeiten von $\sigma = 1,7 \cdot 10^{-6} \text{ S} \cdot \text{cm}^{-1}$, $\sigma = 2,9 \cdot 10^{-6} \text{ S} \cdot \text{cm}^{-1}$ und $\sigma = 1,2 \cdot 10^{-6} \text{ S} \cdot \text{cm}^{-1}$. Darüber hinaus wurde die Leitfähigkeit an einem $\text{Li}_6\text{BaLa}_2\text{Ta}_2\text{O}_{12}$ -Dünnschicht in axialer Geometrie (senkrecht zum Substrat) mit einem Wert von $\sigma = 3,3 \cdot 10^{-5} \text{ S} \cdot \text{cm}^{-1}$ bestimmt. Dieser Wert ist vergleichbar mit der Leitfähigkeit des Volumenmaterials von $\text{Li}_6\text{BaLa}_2\text{Ta}_2\text{O}_{12}$ ($\sigma = 4 \cdot 10^{-5} \text{ S} \cdot \text{cm}^{-1}$). Die vergleichsweise geringe laterale Leitfähigkeit der Granat-Typ-Dünnschichten konnte auf maximal $\sigma = 2,8 \cdot 10^{-5} \text{ S} \cdot \text{cm}^{-1}$ für Multilag-Dünnschichten bestehend aus zwei alternierenden Granat-Typ Phasen ($\text{Li}_{6,5}\text{La}_3\text{Zr}_{1,5}\text{Ta}_{0,5}\text{O}_{12}:\text{Al}_2\text{O}_3$, $\text{Li}_7\text{La}_3\text{Zr}_2\text{O}_{12}:\text{Ga}_2\text{O}_3$) erhöht werden. Weiterführende Experimente zeigten, dass die Mikrostruktur des Dünnschicht einen starken Einfluss auf die Gesamtleitfähigkeit hat. Zusätzlich wurde die elektronische Teilleitfähigkeit einer Volumenprobe und eines Dünnschicht, bestehend aus $\text{Li}_6\text{BaLa}_2\text{Ta}_2\text{O}_{12}$, bestimmt. Dünnschichten aus Lithium-Granaten wurden erfolgreich als Schutzschicht und als ionenselektive Membran in „Hybrid-Zellen“ (Kombination aus Flüssig- und Festelektrolyt in einer Zelle) getestet. Die ionenselektiven Membranen waren in der Lage, den unerwünschten Polysulfid-Shuttle-Mechanismus innerhalb einer Lithium-Schwefel-Zelle zu unterdrücken.

Stichwörter:

Lithium-Festelektrolyt, Granat, Separator, Festelektrolytbatterie, Hybrid-Batterie, PLD

Danksagung

An dieser Stelle möchte ich mich ganz herzlich bei all denjenigen bedanken, die mir während meiner Promotion zur Seite standen. Sie alle haben zum Gelingen dieser Arbeit beigetragen.

Herr Prof. Dr. Jürgen Janek hat mich in all den Jahren, die ich in seiner Arbeitsgruppe verbracht habe, tatkräftig unterstützt. Sei es durch anregende Diskussionen oder das Vertrauen in mich und meine Arbeit, welches er mir tagtäglich entgegen gebracht hat. Insbesondere dafür möchte ich mich an dieser Stelle bedanken.

Herr Prof. Dr. Bruno K. Meyer bin ich für die Übernahme des Korreferats und für die Zusammenarbeit im Bereich der Dünnschichtfestelektrolyte sehr dankbar.

Desweiteren gilt mein Dank Herrn Dr. Stefan Berendts und Herrn Dr. Joachim Sann für die wissenschaftliche Unterstützung während meiner Promotion.

Bei Sebastian Wenzel, Alexander Braun, Rabea Dippel, Martin Busche, Matthias Geiß, Dr. Bjoern Luerßen und Dr. Hany El Shinawi möchte ich mich für die gute und freundschaftliche Zusammenarbeit bedanken.

Einen großen Beitrag zum Gelingen des Projektes haben zudem die Werkstätten (Feinmechanik und Elektronik) geleistet. Ohne Harry Heidt, Gerd Pfeiffer und Harald Weigand hätte es einige Versuchsaufbauten sicherlich nicht gegeben.

Herrn Dr. Kiran Chakravadhanula und Herrn Dr. Christian Kübel vom „Institute of Nanotechnology“ (INT) des „Karlsruher Institute of Technology“ (KIT) möchte ich für die Zusammenarbeit im Bereich der TEM-Charakterisierung meinen Dank aussprechen.

Herrn Dr. Heino Sommer und Herrn Artur Schneider vom „Battery and Electrochemistry Laboratory“ (BELLA) des KIT möchte ich für die erfolgreiche Kooperation im Bereich der Lithium-Schwefel Zellen danken.

Teile dieser Arbeit wurden durch die finanzielle Unterstützung der BASF ermöglicht.

Meinen Eltern und meinem Bruder möchte ich meinen Dank ausdrücken für die immerwährende Unterstützung bei und neben der Promotion.

Meine Partnerin Gesche Mareike Müntze hat mich stets liebevoll unterstützt und es geschafft, mich auch dann aufzuheitern, wenn es mal nicht so gut lief. Nicht nur dafür sei ihr an dieser Stelle herzlich gedankt.

Table of Contents

Abstract	5
Danksagung	7
1. Introduction	1
2. Motivation	4
3. Fundamentals.....	6
3.1 Solid lithium ion conductors	6
3.2 Lithium ion conducting thin films	11
3.3 All solid state batteries	14
3.4 Ion conducting membranes.....	25
4. Experimental.....	30
4.1 Synthesis.....	30
4.1.1 Synthesis of garnet-type bulk materials.....	30
4.1.2 Synthesis of garnet-type thin films.....	32
4.2 Characterization	41
4.2.1 X-ray diffraction.....	41
4.2.2 Conductivity measurements of garnet-type bulk material	41
4.3 Characterization of garnet-type thin films.....	44
4.3.1 Scanning electron microscopy	44
4.3.2 Transmission electron microscopy	45
4.3.3 Conductivity measurements in lateral geometry	45
4.3.4 Conductivity measurements in axial geometry	46
4.3.5 Ion-selective membranes	48
5. Results and Discussion.....	52
5.1 Characterization of garnet-type bulk material	52
5.1.1 X-ray diffraction.....	52
5.1.2 Conductivity measurements	55
5.2 Characterization of garnet-type thin films.....	62
5.2.1 X-ray diffraction.....	62
5.2.2 Scanning electron microscopy	65
5.2.3 Transmission electron microscopy	69
5.2.4 Conductivity measurements in lateral geometry	72
5.2.5 Conductivity measurements in axial geometry	80
5.2.6 Conductivity model	88
5.2.7 Protective coatings.....	91
5.2.8 Ion-selective membranes	94

6. Summary and Conclusions.....	99
7. References.....	105
8. Appendix.....	115
8.1 List of abbreviations	115
8.2 List of symbols	117
8.3 List of peer-reviewed publications	119
8.4 Submitted patents	119
8.5 List of conference contributions.....	119
Declaration	119

1. Introduction

This thesis deals with the preparation and characterization of lithium ion conducting solid state garnet-type materials that can be used as electrolyte in lithium (ion) batteries. The resistance of an all solid state battery depends - among other quantities - on the ionic conductivity of the electrolyte. One way to reduce the resistance of the solid electrolyte in the cell is to reduce its thickness. Therefore, garnet-type solid electrolytes were mainly prepared as thin film in order to investigate whether the material is applicable for the use in batteries.

A battery is formed by the combination of more than one electrochemical cell which is able to transduce the chemical energy stored in the electrodes into electrical energy. In these electrochemical cells the chemically different electrodes are separated by an electrolyte. Under open circuit and charged conditions an electric potential difference arises between both electrodes. This measurable voltage has its origin in the driving force of a chemical reaction between both electrode materials. A requirement for the reaction to take place in an electrochemical cell is the transport of an appropriate ionic species from one electrode to the other. The mediator between both electrodes is the electrolyte, which can be liquid or solid, allowing the ionic species to move across the cell without parallel electron transport in the electrolyte. The electrons need to pass through an external circuit to reach the other electrode. Thus, the electron transport along an external circuit enables the usage of the electrical energy from a chemically driven reaction. The electrical power (P) output depends on two factors, i.e., the voltage (U) and the current (I) as described by Eq. 1.1.

$$P = U \cdot I \quad (1.1)$$

The open cell voltage (E – electromotive force) is thermodynamically determined by the change of Gibbs free energy (ΔG) divided by the number of elementary charges (z) multiplied with the Faraday constant (F):

$$E = -\frac{\Delta G}{zF} \quad (1.2)$$

Thus, the open cell voltage is determined exclusively by the electrode materials, and the electrolyte has ideally no influence on the cell thermodynamics. However, the current in Eq. 1.1 is strongly influenced by the electrolyte and the electrode kinetics. There is no theoretical limit for the current across an electrochemical cell. Nevertheless, internal resistances (R_{int}) limit the current and thereby the actual power output (P) as described by Eq. 1.3:

$$P = P(R_{\text{int}} \rightarrow 0) - R_{\text{int}} \cdot I^2 \quad (1.3)$$

There are three contributions to the internal resistance: the connector resistance (can often be neglected, if low-impedance contacts and wires are used), the reaction resistance of both electrodes and the electrolyte resistance. The term “electrolyte resistance” needs to be specified. Favorable are electrolytes that have a high ionic conductivity of the active ion, thus leading to a low resistance for these ions, and an ideally infinitely large resistance for electrons, i.e., negligible electronic conductivity. Liquid electrolytes tend to behave like ideal electrolytes, i.e., they show no electronic conductivity and the ionic conductivity is high. However, liquid electrolytes are not single ion conductors. Besides the preferred ionic species other ionic species are often also mobile in these liquid electrolytes, as there is always a joint ionic species with a charge contrary to the charge of the preferred active ionic species. In case of Li^+ (the solvation shell is not considered in this case) there will also be a solvated anionic species. This anionic species should not be involved in charge transport.

Another issue of batteries with liquid electrolyte is that the liquid electrolyte might be able to solve chemical species originating from another part of the cell, e.g., an electrode. A good example of this is the lithium sulfur cell [1, 2]. The pristine sulfur from the electrode is insoluble in the liquid electrolyte, but polysulfide anions formed during the cell reaction are soluble. Those polysulfide anions can then undergo an unwanted side reaction at the negative electrode. The polysulfide anions form lithium-sulfur species at the surface of the lithium electrode. These deposited lithium-sulfur species are insoluble and electronically inactive. In consequence, the capacity of the cell is irreversibly lowered [2].

In contrast to liquid electrolytes the solid electrolyte acts as a single ion-selective “filter”, with the drawback that electronic conductivity cannot be eliminated entirely from a solid material. However, for stoichiometric compounds with wide band gap, the electronic conductivity can be very low, so that it becomes insignificant. A fine introduction to solid lithium ion conductors is given in the review of Knauth [3]. Good ionic conductivity and low electronic conductivity are key features of a solid electrolyte [4]. A non-zero electronic current through the electrolyte would result in a decreased electronic potential difference between both electrodes. Furthermore, an electronic current (j_{e-}) consequently leads to self-discharge of the cell, as a corresponding current of ions (j_{Li+}) leads to a coupled flux of the neutral component (j_{Li}).

$$j_{Li} \triangleq j_{Li+} = j_{e-} \quad (1.4)$$

Besides the benefit of ion selectivity solid electrolytes are considered as intrinsically safe, resistant to lithium dendrite growth and are well operable at elevated temperatures. Furthermore, damage to the cell from freezing liquid electrolyte is avoided. Therefore, solid electrolytes could be key components to enable so-called next generation cells (e.g., Li-S, Li-O₂) [5] and are necessary for the construction of solid state batteries. However, identifying suitable solid electrolytes represents a major challenge. A general introduction to all solid state batteries is given in [4, 6-8].

2. Motivation

The aim of the PhD project was to prepare and characterize garnet-type solid electrolytes, mainly prepared as thin films by pulsed laser deposition. The academic interest in solid lithium ion conducting thin films was rather limited at the beginning of this doctoral project. Thus, there were no publications about lithium ion conducting garnet-type thin films at all. To the contrary, there were still unsolved problems in the preparation of lithium ion conducting garnet-type phases even as bulk material. Especially the preparation of cubic $\text{Li}_7\text{La}_3\text{Zr}_2\text{O}_{12}$ was a delicate task and often tetragonal $\text{Li}_7\text{La}_3\text{Zr}_2\text{O}_{12}$, with poor lithium ion conductivity, was obtained [9]. The importance of a stabilizing dopant for the cubic phase as well as the degradation in air [10-12] by formation of Li_2CO_3 [13] was not yet known to the academic community. Currently, the interest in solid lithium ion conducting electrolytes and lithium ion conducting thin films rises rapidly. This is due to the fact that potential next generation batteries (lithium-sulfur and lithium-oxygen) are not yet commercially realized and that usage of solid electrolytes promises an intrinsically safe battery if applied to an all solid state battery concept. Also, solid electrolytes could be used as protective layers on electrode materials or on battery separators. The advantages of solid electrolytes compared to liquid electrolytes are their non-flammability (of oxide-type solid electrolytes at least) coupled with possible operation temperatures higher than the boiling point of most liquid electrolytes, and their expected mechanical stability against lithium dendrites. Furthermore, their ion selectivity prevents the migration of undesired redox-active species.

In all cases, the solid electrolyte needs to fulfill several criteria like high ionic and low electronic conductivity. In addition to that, it needs to be chemically and electrochemically stable. For commercial usage the costs of material and production need to be considered as well as recyclability and toxicity.

There are two general possibilities for the application of solid electrolytes, either as bulk solid electrolytes – as “thick films” - or as solid electrolyte thin films. The basic requirements are identical, with the exception that solid electrolyte thin films can have a lower ionic conductivity in order to achieve the same resistance of a cell. At a required resistance the conductivity can be lowered by the same factor as the thickness is reduced. From a research perspective, another advantage of solid ion conducting thin films is that

they facilitate investigations under vacuum conditions. This means that a broad variety of vacuum analysis methods, e.g., scanning electron microscopy, transmission electron microscopy and x-ray photoelectron spectroscopy can be used to investigate single parts of a cell (electrodes, electrolytes, and their interfaces) as well as the cell chemistry of a whole cell. Vacuum stability is a result of the negligible vapor pressure of solid ion conducting materials compared to liquid electrolytes. For the investigation by vacuum analysis methods thin films are preferred over bulk materials as they provide smooth model type surfaces that can be studied more easily. A first task of this doctoral project was to realize model type solid electrolyte thin films of lithium ion conducting garnet-type phases that were not prepared as thin film so far. Subsequently, structural and electrochemical characterization of the garnet-type thin films was performed in order to broaden the knowledge about garnet-type material in general and lithium ion conducting garnet-type material thin films in particular.

3. Fundamentals

3.1 Solid lithium ion conductors

Solid lithium ion conductors are at least partially expected to replace organic electrolytes with the benefit of possible miniaturization and increased safety [4, 14]. Before classifying the numerous solid lithium ion conductors the criteria defining a good lithium ion conductor need to be discussed. The criteria naturally depend on the field of application. In the following, the criteria for a solid lithium electrolyte that could be used in an all solid state cell, not necessarily in a thin film cell, are listed.

- i. The solid lithium ion conductor should be a thermodynamically stable phase at all operating conditions. This is required for the long-term stability of the system [15].
- ii. The solid electrolyte should be chemically inert against the applied electrode materials, including metallic lithium. Hence, the electrochemical window of the solid electrolyte needs to be wider than the cell voltage which is defined by the Gibbs free energy of the cell reaction. For high voltage lithium based batteries an electrochemical window of > 5 V versus Li^+/Li is needed.
- iii. The lithium ion conductivity (bulk and grain boundary) should be sufficient for the respective application. This means that the current needed for a certain application should not be limited by the solid electrolyte. A liquid electrolyte like EC:PC:LiPF₆ has a conductivity of about $5 \cdot 10^{-3} \text{ S} \cdot \text{cm}^{-1}$ [16]. The typical distance between two electrodes of a standard battery is about 40 μm . Thereby, the specific resistance (thickness divided by conductivity) is $0.8 \text{ } \Omega \cdot \text{cm}^2$. This value should also be reached for solid electrolytes. For a solid electrolyte thin film which is typically about 1 μm thick a conductivity of $1.25 \cdot 10^{-4} \text{ S} \cdot \text{cm}^{-1}$ is required to achieve $0.8 \text{ } \Omega \cdot \text{cm}^2$. However, liquid electrolytes have transference numbers for lithium ions smaller than unity (usually smaller than 0.5) [17]. Thereby, the conductivity of the solid electrolyte given here is the upper limit and usually a conductivity of $> 10^{-5} \text{ S} \cdot \text{cm}^{-1}$ should be sufficient.
- iv. The solid electrolyte should have a negligible electronic conductivity. Hence, the lithium transference number has to be close to unity ($t_{\text{Li}^+} \approx 1$) at the given

electrochemical potentials (low lithium activity at the positive and high lithium activity at the negative electrode) [4]. This parameter is crucial for the self-discharge rate of the cell. A significant electronic conductivity reduces the usable cell voltage by the formation of a diffusion potential.

- v. The compatibility with the electrode materials concerning the transfer resistance at the respective phase boundaries needs to be achieved. The transfer resistance for lithium ions should be as low as possible [18].
- vi. Lithium dendrite growth should be prevented by a mechanically stable and dense solid electrolyte material in case of lithium metal electrodes.
- vii. The solid electrolyte should be accessible as thin film by conventional industrial sputtering processes or by chemical thin film deposition methods [19].
- viii. The starting materials need to be abundant (for economic use) [20].
- ix. The solid electrolyte and its chemical constituents should be non-toxic [19].
- x. When taking a battery apart the solid electrolyte should be able to be reused or recycled.

Several solid lithium ion conducting materials are introduced in the following section. So far, no material is established as standard solid electrolyte for commercial lithium based battery applications (with the exception of “LiPON” introduced in chapter 3.2).

Perovskite-type oxides – Lithium ion conducting ABO₃-type lithium lanthanum titanate (LLT) of the chemical composition Li_{3x}La_{2/3-x}TiO₃, which can also be written as Li_{3x}La_{2/3-x}□_{1/3-2x}TiO₃ exhibits A-site vacancies if $x < 1/6$ (□). A high room temperature ionic conductivity of $\sigma \approx 10^{-3} \text{ S}\cdot\text{cm}^{-1}$ for $x = 0.11$ [21] of single crystals is enabled by those A-site vacancies. However, polycrystalline LLT shows a decreased lithium ion conductivity of about $\sigma \approx 10^{-5} \text{ S}\cdot\text{cm}^{-1}$ due to a high grain boundary resistance [22]. Furthermore, contact to strong reducing materials like metallic lithium leads to a reduction of Ti⁴⁺ resulting in an electronic conductivity increase [23]. Further information about this perovskite-type lithium ion conductors can be found in the review articles from Bohnke and Stramare et al [23, 24].

NASICON – This acronym stands for sodium super ionic conductor and originally was used for the phosphate-based phase NaM₂(PO₄)₃ (M = Ge, Ti, Zr) which was first reported in 1968 [25]. The NASICON type sodium conducting structure was transferred to lithium

ion conducting solid electrolytes. By partial substitution of the tetravalent metal cation (M^{+4}) with a trivalent dopant (e.g., Al, La, Y, Sc) [26] the ion conductivity can be increased. Among the Al-doped materials the phase $Li_{1.3}Al_{0.3}Ti_{1.7}(PO_4)_3$ (LATP) has the highest conductivity of about $\sigma = 3 \cdot 10^{-3} \text{ S} \cdot \text{cm}^{-1}$ [26]. However, LATP is not stable versus metallic lithium due to reduction of Ti^{4+} [27].

LISICON – The acronym LISICON (lithium super ionic conductor), was first coined to denote $Li_{14}Zn(GeO_4)_4$ [28, 29] which has a lithium ion conductivity of about $\sigma \approx 10^{-7} \text{ S} \cdot \text{cm}^{-1}$, and which describes a whole class of lithium ion conducting materials. By replacing the oxide ions of the LISICON structure with sulfide ions, which are larger and easier to polarize, the conductivity can be increased. The so-called thio-LISICON was introduced by Kanno et al. [30-32] $Li_{4+x-\delta}Ga_xS_4$ exhibits a conductivity of about $\sigma = 6 \cdot 10^{-5} \text{ S} \cdot \text{cm}^{-1}$ for $x = 0.25$ and by addition of a silicon constituent ($Li_{3.4}Si_{0.4}P_{0.6}S_4$) a conductivity of $\sigma = 6.4 \cdot 10^{-4} \text{ S} \cdot \text{cm}^{-1}$ [31] was obtained. The main drawback of the LISICON-type materials is their instability versus metallic lithium and CO_2 [3].

Li_3N – Lithium nitride crystallizes in a layered structure and thus exhibits anisotropic lithium ion conduction. Single crystals of Li_3N show a lithium ion conductivity of about $\sigma = 1.2 \cdot 10^{-3} \text{ S} \cdot \text{cm}^{-1}$ perpendicular to the c -axis [33] and a conductivity of about $\sigma = 1 \cdot 10^{-5} \text{ S} \cdot \text{cm}^{-1}$ along the c -axis [33] at 27 °C. Due to the anisotropy of the lithium ion conduction the conductivity of polycrystalline material is lower than $10^{-3} \text{ S} \cdot \text{cm}^{-1}$ [34]. Furthermore, the material decomposes at potentials of 0.44 V versus Li^+/Li [35].

Li_2S -based glasses and glass ceramics – Lithium ion conducting glasses and glass ceramics based on Li_2S with further addition of other oxides or sulfides can be prepared by mechanical milling or melt quenching. Two representative compounds are Li_2S - GeS_2 and Li_2S - P_2S_5 each with variable Li_2S -to- GeS_2/P_2S_5 ratio. The conductivities are about $\sigma \approx 4 \cdot 10^{-5} \text{ S} \cdot \text{cm}^{-1}$ and $\sigma \approx 2 \cdot 10^{-4} \text{ S} \cdot \text{cm}^{-1}$ for 50 Li_2S -50 GeS_2 and 75 Li_2S -25 P_2S_5 [36] (the numbers in front of the respective materials denote the composition as used in literature), respectively. Further sulfides, oxides or phosphates can be added to tune the material properties (e.g., SiS_2 , Li_4SiO_4) [37]. These lithium ion glasses tend to be strongly hygroscopic and deliquesce in contact with aqueous electrolytes or at ambient air under release of H_2S [38].

Garnet-type materials – The first reported lithium ion conducting garnet-type material was $\text{Li}_5\text{La}_3\text{M}_2\text{O}_{12}$ ($\text{M} = \text{Nb}, \text{Ta}$) [18] which is related to the $\text{A}_3\text{B}_2(\text{XO}_4)_3$ garnet structure. This garnet-type material crystallizes in a cubic $\text{Ia}\bar{3}\text{d}$ space group and has a conductivity of about $\sigma \approx 10^{-6} \text{ S}\cdot\text{cm}^{-1}$ [18]. The M sites and the La sites can be substituted in order to increase the concentration of lithium in the structure.

Possible substituents for the M site (16a position, valence +5) are cations with a valence of +4 with a diameter of approximately 80 pm [39]. For that purpose Zr^{4+} is favored with a diameter of 86 pm [40]. Furthermore, Zr-doped lithium ion conducting garnets are stable in contact with metallic lithium and an increase of the lithium ion concentration within the garnet-type structure is caused by means of electro-neutrality. A drawback of solely zirconium garnet-type material - $\text{Li}_7\text{La}_3\text{Zr}_2\text{O}_{12}$ - is the need of stabilization of the cubic phase by addition of Al_2O_3 or Ga_2O_3 during synthesis. Otherwise a tetragonal phase with lower lithium ion conductivity compared to the cubic phase is obtained [9]. The conductivity of cubic $\text{Li}_7\text{La}_3\text{Zr}_2\text{O}_{12}$ stabilized with Al_2O_3 can reach $\sigma = 4 \cdot 10^{-4} \text{ S}\cdot\text{cm}^{-1}$ [9], for $\text{Li}_7\text{La}_3\text{Zr}_2\text{O}_{12}$ stabilized with Ga_2O_3 conductivities of up to $\sigma = 5.4 \cdot 10^{-4} \text{ S}\cdot\text{cm}^{-1}$ [41] are reported. The Al^{3+} as well as the Ga^{3+} cations tend to occupy the 24d [9] and 96h [42] sites, which are regularly occupied by Li^+ , thereby lowering the lithium content of the garnet-type material ($1 \text{ Al}^{3+} = 1 \text{ Ga}^{3+} = 3 \text{ Li}^+$). The amount of aluminum and gallium needed for the stabilization of the cubic garnet-type phase can be reduced by partial re-substitution of zirconium by tantalum. A survey of these materials is given in detail in the literature [39]. An overview of the conductivities of these materials is given in an Arrhenius plot in Figure 1. For completeness, the $\text{Li}_6\text{BaLa}_2\text{Ta}_2\text{O}_{12}$ phase is depicted as well in Figure 1. The garnet-type materials stabilized with Al_2O_3 are labeled by “ $\text{Li}_{7-x}\text{La}_3\text{Zr}_{2-x}\text{Ta}_x\text{O}_{12}:\text{Al}$ ”. The replacement of Li^+ in the garnet-type structure by Al^{3+} or Ga^{3+} is not included in the chemical formula for these garnet-type phases in this thesis, because the total amount of Al^{3+} and Ga^{3+} in the lattice cannot be given exactly. This is due to the fact that the addition of Al_2O_3 or Ga_2O_3 results also in the formation of a glass matrix around the garnet-type particles [41].

Another strategy to improve the conductivity of the $\text{Li}_5\text{La}_3\text{Ta}_2\text{O}_{12}$ phase is the substitution of La with a valence of +3 by a cation with a valence of +2. The doping of the solely tantalum containing $\text{Li}_5\text{La}_3\text{Ta}_2\text{O}_{12}$ garnet-type phase by addition of an earth alkali cation on the lanthanum 24c site affects the lithium ion conductivity in two ways: First, the

lithium ion content is raised in accordance with the amount of earth alkali introduced into the garnet-type structure by means of electroneutrality. The increase of the lithium content in the garnet lattice caused by means of electroneutrality can be explained considering the formula of the garnet-type material. C denotes an earth alkali cation on a 24c La site $\text{Li}_{5+y}\text{La}_{3-y}\text{C}_y\text{Ta}_2\text{O}_{12}$. Second, the lattice parameter increases widening the lattice and thereby reducing the activation energy for ion jumps [20, 43]. Both effects add to an increase in lithium ion conductivity. Barium is the favored earth alkali for this type of doping, because its contribution to the lattice widening of the garnet-type structure is the highest compared to other earth alkalis with smaller diameter. The conductivity of $\text{Li}_6\text{BaLa}_2\text{Ta}_2\text{O}_{12}$ garnet-type material is about $\sigma = 4 \cdot 10^{-5} \text{ S} \cdot \text{cm}^{-1}$ [44].

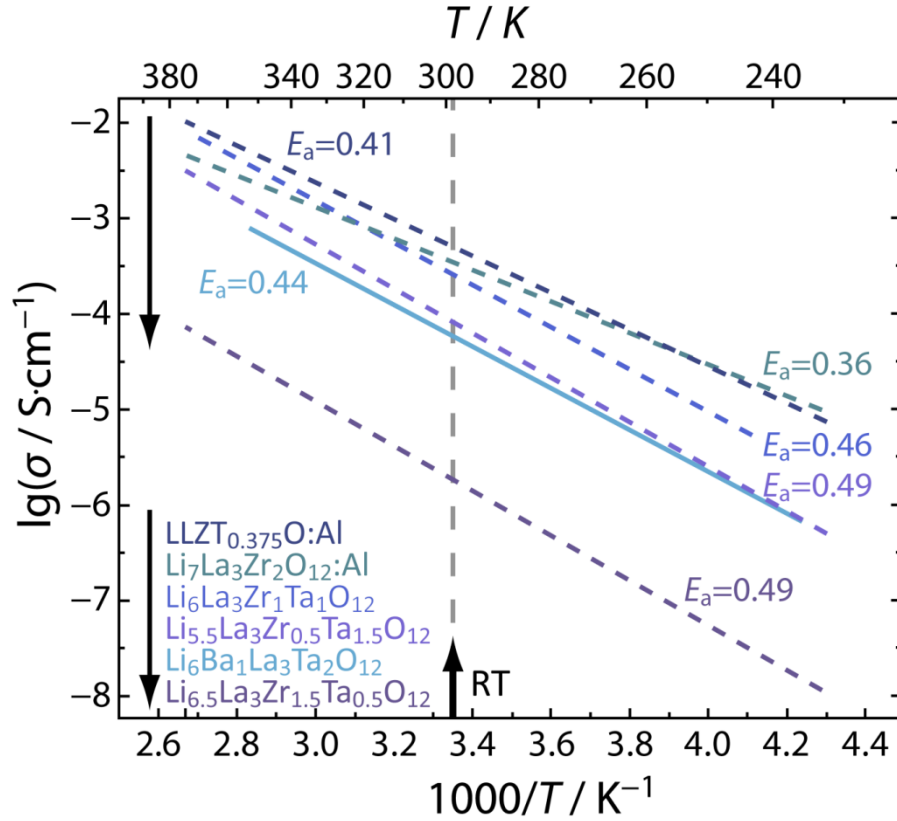


Figure 1: Modified survey of the conductivity of different garnet-type materials after Buschmann et al.[39]. Additionally, the activation energies for the ionic conductivity are displayed. An arrow with a dashed grey line indicates room temperature (RT).

A good survey of the different garnet-type materials is given in the review of Thangadurai et al. [19]. The structure of the garnet-type materials is discussed extensively in the publications of Cussen et al. [45-47], Buschmann et al. [9] and Logéat et al. [48]. Besides their potential application as solid electrolytes for lithium ion batteries, garnet-type $\text{Li}_6\text{BaLa}_2\text{Ta}_2\text{O}_{12}$ has been used to prepare potentiometric CO_2 gas sensors which were successfully tested in a temperature range from 300 °C to 500 °C by Zhu et al. [49]. The use of lithium ion conducting garnet-type materials as CO_2 gas sensor is quite odd, as these materials tend to react with CO_2 (in humid air) [13].

3.2 Lithium ion conducting thin films

The demands on lithium ion conducting thin films are the same as stated in chapter 3.1, but need further explanation. Additionally, atmosphere and temperature during the electrolyte deposition process need to be considered as the electrode material could otherwise be damaged e.g., by reduction/oxidation, undesired side reactions or by a phase transformation. Some electrode/electrolyte compositions are therefore not suitable, as the deposition parameters of one material will affect the previously applied thin film.

Furthermore, the deposited electrolyte thin film needs to be free of cracks and pinholes in order to prevent later short circuits of the electrodes. Cracks can be formed by strain due to lattice mismatch with the substrate or by different thermal expansion coefficients. A flexible electrolyte thin film would also be preferred to compensate volume changes of the electrodes during cycling.

Until now, mainly nitrogen doped glassy Li_3PO_4 (“LiPON”) is utilized as a lithium ion conducting thin film electrolyte. The conductivity of this material is about $2 \cdot 10^{-6} \text{ S} \cdot \text{cm}^{-1}$ with an activation energy of about 0.4 eV - 0.6 eV [50, 51]. A big advantage of “LiPON” compared to most other thin film electrolytes is its rather simple deposition by radio frequency sputter deposition using a Li_3PO_4 target in nitrogen atmosphere, which can easily be upscaled to larger areas. Furthermore, “LiPON” is stable in contact with metallic lithium [52, 53].

Inspired by “LiPON” deposition Li_2SO_4 was also ablated by radio frequency magnetron sputter deposition under nitrogen atmosphere. In accordance with “LiPON” this material was named as “LiSON”. “LiSON” conductivity is only reported by a single study as $\sigma = 2 \cdot 10^{-5} \text{ S} \cdot \text{cm}^{-1}$ with an activation energy of about 0.47 eV [54].

Until now, mainly “LiPON” and a few other materials were prepared as lithium ion conducting thin films. These are summarized in Table 1. The highest lithium ion conductivity was reached by $80\text{Li}_2\text{S}-20\text{P}_2\text{S}_5$ thin films, especially after a subsequent heat treatment (see Ref. [55] for detailed information). However, a practical drawback is the decomposition of $\text{Li}_2\text{S}-\text{P}_2\text{S}_5$ thin films under release of H_2S in contact with air [38].

Also garnet-type phases are a promising class of lithium ion conducting solid electrolytes. At the beginning of this thesis project in 2010 these had only been synthesized as bulk material. In 2013 Kim et al. reported the successful preparation of Al_2O_3 stabilized $\text{Li}_7\text{La}_3\text{Zr}_2\text{O}_{12}$ thin films [56] with conductivities of about $\sigma = 2.5 \cdot 10^{-6} \text{ S} \cdot \text{cm}^{-1}$ for (100) oriented and $\sigma = 1 \cdot 10^{-5} \text{ S} \cdot \text{cm}^{-1}$ for (111) oriented thin films on gadolinium gallium garnet (GGG – $\text{Gd}_3\text{Ga}_5\text{O}_{12}$) by pulsed laser deposition. So far sputter deposition experiments of garnet-type materials were not successful and only amorphous films were obtained [57] which need to be crystallized in a subsequent step [58]. The amorphous and subsequently laser annealed garnet-type thin films show comparably poor conductivities of about $\sigma = 4 \cdot 10^{-7} \text{ S} \cdot \text{cm}^{-1}$ and $\sigma = 7.36 \cdot 10^{-7} \text{ S} \cdot \text{cm}^{-1}$, respectively.

Two garnet-type phases are of particular interest as materials for the preparation of electrolyte thin films due to their transport properties: The cubic phase of $\text{Li}_7\text{La}_3\text{Zr}_2\text{O}_{12}$ (stabilized by Al_2O_3 , Ga_2O_3 or by re-substitution of zirconium by tantalum) and $\text{Li}_6\text{BaLa}_2\text{Ta}_2\text{O}_{12}$, as these show the highest lithium ion conductivity. The deposition of $\text{Li}_6\text{BaLa}_2\text{Ta}_2\text{O}_{12}$ is expected to be easier because no tetragonal phase of this garnet-type material is known.

Table 1: Summary of lithium ion conducting thin films, their deposition method, conductivity at room temperature σ_{RT} and activation energy E_a . The asterisk (*) at the $\text{Li}_2\text{S-Li}_2\text{S}_5$ thin film indicates that this value was obtained after heat treatment.

Material	Deposition method	$\sigma_{\text{RT}} / \text{S}\cdot\text{cm}^{-1}$	E_a / eV
“LiPON” [50, 51]	rf-MS	$2\cdot 10^{-6}$	0.4 – 0.6
“LiSON” [54]	rf-MS	$2\cdot 10^{-5}$	0.47
Li_3PO_4 [59]	PLD	$5.1\cdot 10^{-7}$	0.59
Li_4SiO_4 [59]	PLD	$1.2\cdot 10^{-8}$	0.64
$50\text{Li}_4\text{SiO}_4\text{-}50\text{Li}_3\text{PO}_4$ [59]	PLD	$1.6\cdot 10^{-6}$	0.53
$80\text{Li}_2\text{S-}20\text{P}_2\text{S}_5$ [55]	PLD	$7.9\cdot 10^{-5}$	0.44
$80\text{Li}_2\text{S-}20\text{P}_2\text{S}_5$ [55]	PLD	$(2.8\cdot 10^{-4})^*$	$(0.39)^*$
c- $\text{Li}_7\text{La}_3\text{Zr}_2\text{O}_{12}(100)$ [56]	PLD	$2.5\cdot 10^{-6}$	0.52
c- $\text{Li}_7\text{La}_3\text{Zr}_2\text{O}_{12}(111)$ [56]	PLD	$1\cdot 10^{-5}$	0.55
c- $\text{Li}_7\text{La}_3\text{Zr}_2\text{O}_{12}$ [58]	PLD	$7.36\cdot 10^{-7}$	0.32
Li-La-Zr-O [57]	Rf-MS	$4\cdot 10^{-7}$	0.70

Deposition methods: rf-MS: radio frequency magnetron sputtering, PLD: pulsed laser deposition.

3.3 All solid state batteries

The expected advantages of all solid state lithium batteries are safety, reliability and the possible use of high voltage cathode materials compared to conventional lithium ion batteries with organic electrolytes. These advantages are gained through the omission of liquid electrolyte. Oxide solid electrolytes are non-flammable, have no leakage of a liquid phase [14] and have, depending on the solid electrolyte, a wide electrochemical window of operation versus Li^+/Li .

When discussing all solid state batteries one has to differentiate between all solid state thin film batteries on the one hand and solid state bulk batteries (thick film batteries) on the other hand. All solid state thin film batteries are prepared by vapor deposition techniques, mainly by sputter deposition or pulsed laser deposition. Thereby, the thickness of one cell is restricted to a few μm ; commercially available all solid state thin film batteries have a thickness of up to 10 μm , including the metal substrate and excluding the housing.

A schematic illustration of the general fabrication steps needed to build an all solid state thin film battery is depicted in Figure 2. Figure 2 a) shows the substrate which needs to be suited to deposit the different battery components. Furthermore, the substrate needs to be smooth in order to avoid short circuits induced by defects. Figure 2 b) shows the deposition of the metallic electrode contacts. The big contact pad is for the positive electrode (deposited first) and the smaller contact pad is for the second, negative electrode. The deposition of the first electrode is shown in c). After the deposition of the positive electrode the solid electrolyte thin film is applied on top of the electrode thin film (Figure 2d), covering an area larger than the area of the first applied electrode. Hence, there is no direct contact between the first and the second electrode. The negative electrode, applied in step e), is deposited with the same electrode area as the first electrode with the exception of the connection to the electrode contact pad. In a last step f) the all solid state thin film battery is encapsulated, e.g., by a compound foil.

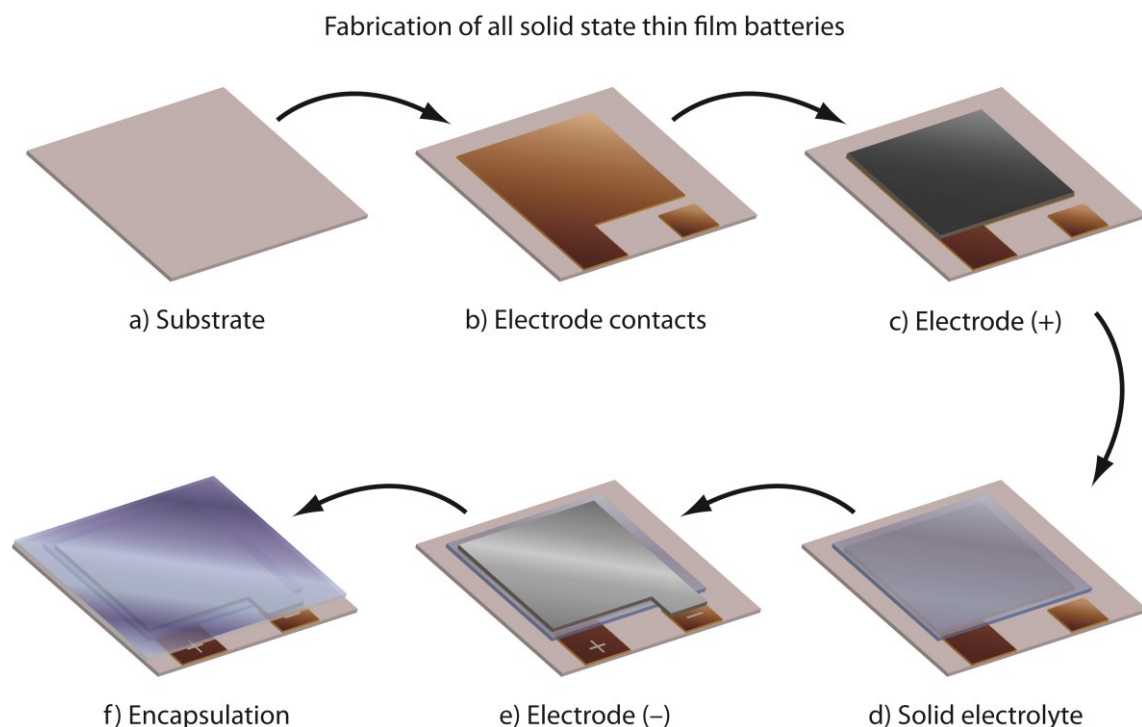


Figure 2: Schematic illustration of the necessary fabrication steps of an all solid state thin film battery via a vapor deposition process. a) Shows the substrate on which the electrode contacts are deposited in a first step b). Afterwards, the first electrode gets deposited c) (usually the positive electrode), followed by the solid electrolyte thin film d). e) and f) depict the deposition of the second electrode (negative) and the encapsulation, respectively.

The reason that “LiPON” is mainly used as solid electrolyte for thin film batteries, despite its low conductivity, is its favorable combination of other properties. “LiPON” combines a good chemical and electrochemical stability with acceptable lithium ion conductivity. One key feature of “LiPON” is that it can be obtained via sputter deposition at room temperature, due to the fact that “LiPON” is an amorphous material. Several other lithium solid electrolyte thin films (listed in chapter 3.2) exist, but usually these exhibit too low conductivities ($< 10^{-6} \text{ S}\cdot\text{cm}^{-1}$). An exception are Li_2S -based systems which exhibit high ionic conductivities ($> 10^{-5} \text{ S}\cdot\text{cm}^{-1}$) and can be deposited as amorphous material or as glass-ceramic, but are rather unstable in air and decompose partly to H_2S [38].

An overview of selected all solid state thin film lithium cells is given in Table 2. Displayed are the compositions of the solid electrolytes as well as anode and cathode

materials and, if available, the preparation method along with their respective thickness (in square brackets; Σ denotes the total thickness of anode, cathode and solid electrolyte). Furthermore, the potential window used for cycling is given with the current density and the number of cycles reached. The capacity of the thin film cell, the energy density (the potential used for the calculation is given in brackets and was estimated from the respective discharge behavior of the cell as it is shown in the reference) as well as the year of publication with the reference at the end is given.

Table 2: Overview of secondary lithium thin film cells.

Anode	Electrolyte	Cathode	U / V	$j / \mu A \cdot cm^{-2}$	Cycles	Specific capacity / $\mu Ah \cdot cm^{-2}$	Energy density / $Wh \cdot l^{-1}$	Year	Ref.
Li (TE) [4 μm]	$Li_{3.6}Si_{0.6}P_{0.4}$ (rf-S) [4 μm]	TiS ₂ (CVD) [1 μm]	2.5 - 1.5	3 - 16	2000	45 - 150	105- 350 (at 2.1 V)	1983	[70]
$Li_xV_2O_5$ (rf-MS) [0.3 μm]	LiPON (rf-MS) [1.5 μm]	V ₂ O ₅ (rf-MS) [0.3 μm]	3.5 - 1	10	350	6	74 (at 2.6 V)	1999	[71]
Li	$LiI-Li_3PO_4-P_2S_5$ (S)	TiS ₂ (S) [$\Sigma \approx 10 \mu m$]	2.8 - 1.8	100	>1000	170	357 (at 2.1 V)	1994	[61]
Li [0.5 μm]	$Li_2O-V_2O_5SiO_2$ (rf-MS) [1 μm]	MnO _x (rf-S) [4 μm]	3.5 - 1.5	10	100	15	68 (at 2.5 V)	1990	[72]
Li (TE) [3 μm]	LiPON (rf-S) [1.5 μm]	LiMnO ₂ (rf-MS) [1 μm]	4.5 - 2.5	2 - 40	>1000	11 - 81	66 - 486 (at 3.3 V)	1999	[73]
Cu (Li-plated) [1.5 μm]	LiPON (rf-MS) [2 μm]	LiCoO ₂ (rf-MS) [3.5 μm]	4.2 - 3.0	≤ 5000	1000	130	733 (at 3.95 V)	2000	[53]
Li (TE) [3 μm]	LiPON (rf-MS) [2 μm]	LiCoO ₂ (rf-MS) [1.8 μm]	4.2 - 3.0	~60	500	122	709 (at 3.95 V)	1996	[74]
Li (TE) [3.5 μm]	LiPON (rf-MS) [1 μm]	$Li_x(Mn_yNi_{1-y})_{2-x}O_2$ (rf-MS) [3 μm]	4.8 - 2.5	5	~10	136	707 (at 3.9 V)	1998	[75]
SnO (PLD)	$Li_{2.2}V_{0.54}Si_{0.46}O_{3.4}$ (PLD)	LiCoO ₂ (PLD) [$\Sigma \approx 2 \mu m$]	3.3 - 0.7	44 - 200	100	4 - 10	46 - 115 (at 2.3 V)	2004	[76]
Li (TE) [1 μm]	$LiNbO_3[Li_2S-P_2S_5]$ (PLD) [10 μm]	LiCoO ₂ [9.1 μm]	4.2 - 3.0	100	500	400	786 (at 3.95 V)	2012	[77]

Deposition method is given in brackets if available. TE: thermal evaporation, S: sputter deposition, rf: radio frequency, MS: magnetron sputtering, CVD: chemical vapor deposition, PLD: pulsed laser deposition.

LiCoO_2 is the favored positive electrode material for the preparation of solid state lithium thin film batteries, followed by LiMn_2O_4 . The negative electrode material of choice is metallic lithium which is quite remarkable as metallic lithium undergoes a dramatic volume change during cycling, which may cause an unstable electrode/electrolyte interface. The processes that take place at the interface between a metallic lithium electrode and the solid electrolyte in an all solid state battery are shown schematically in Figure 3. The positive electrode material is depicted as 'counter electrode'. Figure 3 a) shows the cell under open circuit conditions - the cell is in equilibrium (if the solid electrolyte shows no electronic conductivity). The interface between the metallic lithium electrode and the solid electrolyte is smooth, and the electric field inside the solid electrolyte is homogeneous (not shown in the figure). Figure 3 b) shows the cell during discharge (as indicated by the glowing light bulb). Lithium stripping starts at the interface between the metallic lithium electrode and the solid electrolyte, injecting lithium vacancies into the lithium electrode, as lithium ions migrate towards the negative electrode. The interface between solid electrolyte and the respective parent metal electrode was intensively studied e. g. by Rickert et al. [78-80] and later by Janek et al. [81-85]. Mainly the interface between silver and a silver solid electrolyte ($\text{Ag}|\text{Ag}_y\text{X}$ - X = halogenide or sulfide) was studied.

Voids may also be formed during charging of the cell, as the lithium plating can only occur at the interface between the solid electrolyte and the metallic lithium electrode. If the lithium plating is not homogeneous lithium voids will occur, which lead to the same phenomenon as already described for the discharge of the cell.

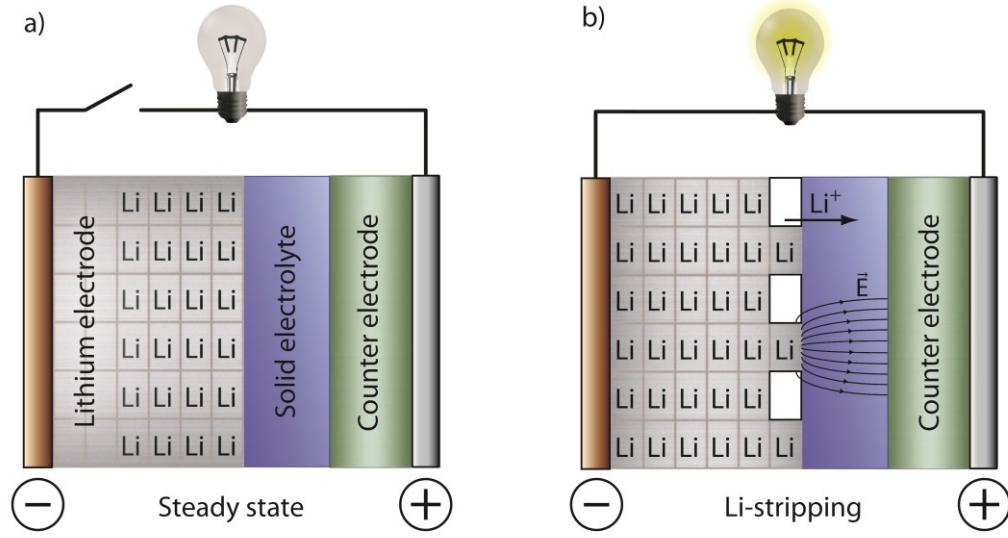


Figure 3: Schematic illustration of the processes at a metallic lithium electrode in an all solid state battery. a) Shows the cell with a smooth interface between the metallic lithium electrode and the solid electrolyte, there is no charge transfer. b) Shows the cell during discharge, the current is unequal to zero. The lithium stripping causes the formation of lithium vacancies at the interface between the lithium electrode and the solid electrolyte.

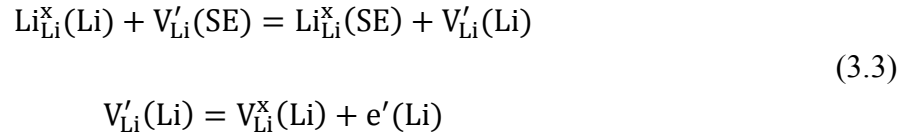
Due to the lithium vacancies formed at the interface the electric field becomes inhomogeneous, and the contact area between the lithium electrode and the solid electrolyte decreases. Under potentiostatic conditions, the current (I) of the cell decreases as the resistance (R) increases because of the lowered contact area (A) according to Eq. 3.1 and Eq. 3.2:

$$I = \frac{U}{R} \quad (3.1)$$

$$R = \frac{1}{\sigma} \cdot \frac{l}{A} \quad (3.2)$$

The spacing (l) between the electrodes and the conductivity (σ) of the solid electrolyte remain constant. Galvanostatic conditions can lead to temporary instabilities. The applied voltage under galvanostatic conditions becomes a function of time $U(t)$. Sometimes even

periodic voltage oscillations [81, 85] can occur at the parent metal|solid electrolyte interface. Critical for the occurrence of these voltage oscillations are the current density and the applied mechanical pressure. The frequency of the oscillation increases with increasing current density, due to the higher reaction rate of the anodic dissolution. A possible version of this reaction adopted for a lithium solid electrolyte (SE) is depicted in Eq. 3.3 using Kröger-Vink notation.



The structure element $\text{Li}_{\text{Li}}^{\times}(\text{Li})$ stands for a lithium atom in the lithium lattice and $\text{V}_{\text{Li}}'(\text{SE})$ stands for a lithium ion vacancy in the solid electrolyte. A transfer of lithium from the lithium metal electrode onto the position of a lithium ion vacancy in the solid electrolyte leads to $\text{Li}_{\text{Li}}^{\times}(\text{SE})$ - a lithium ion on a lithium ion position in the solid electrolyte. Thereby a lithium vacancy $\text{V}_{\text{Li}}^{\times}(\text{Li})$ is formed (injected) in the lithium electrode. As can be seen from Eq. 3.3 a constant current leads to a constant rate of vacancy formation in the parent metal electrode. The formation of vacancies and thereby the formation of voids can lead to degradation of the interface between the solid electrolyte and the metal electrode if the solid electrolyte or the metal electrode are unable to react to the local contact rupture by plastic deformation. The diffusion of the lithium vacancies in the metal electrode away from the solid electrolyte|metal electrode interface can lead to a stabilization of the morphology (these processes are usually slow at room temperature). A possible solution to this problem is the application of high pressure so that the metal electrode, in our case lithium, undergoes a plastic deformation. Furthermore, low current densities (i.e., more time for lithium vacancy diffusion in the metal) and higher temperatures (i.e., increasing the vacancy diffusion and thus leading to a higher plasticity of the lithium electrode) may help to stabilize the interface. However, all solid state lithium batteries show stable cyclability even if metallic lithium electrodes are utilized. To further improve the cyclability of an all solid state cell with metallic lithium electrodes several techniques can be applied. One technique is the doping or alloying of the lithium metal electrode. Either another metal, e.g., aluminum, is added to improve the mechanical properties, or a small interphase is added between the metallic lithium electrode and the solid electrolyte. This interphase is often generated by the deposition of a thin metal film, e.g., indium, on the

solid electrolyte, which then alloys with the metallic lithium. This interphase improves the contact between electrode and solid electrolyte as the formation of voids is prevented by the redox inactive metallic (indium) framework structure. Hence, the whole solid electrolyte surface keeps contact.

Another way of improving the cyclability is the use of additional lithium on the negative electrode side. The cell itself does in principle not need additional lithium on the negative electrode if the cell is assembled in the discharged state. In the discharged state the positive electrode is lithium rich, and lithium is deposited cathodically on the lithium electrode during the first charge of the cell. By applying a lithium electrode the mechanical pressure is raised when the cell gets charged, but the ductile lithium is able to compensate the tension by plastic deformation. By vacuum sealing these cells into pouches, before they are charged for the first time, a pressure is applied on the ductile lithium electrode so that the lithium is mechanically pressed onto the solid electrolyte. Hence, the formation of larger voids is prevented and the electrode|solid electrolyte interface remains homogeneous. Another advantage of this procedure is that cathodically deposited lithium should be able to be anodically dissolved with high current densities and low over-voltages, as shown for the dissolving of silver whiskers in contact with α -Ag₂S by Corish et al. [86].

There are also other interesting solid electrolytes besides “LiPON” that can be used for the fabrication of all solid state secondary lithium batteries. Li₂S-based solid electrolytes are interesting candidates because they show a high lithium ion conductivity and can be used as solid electrolyte in all solid state thin film batteries [77] as well as in all solid state bulk batteries [87-89]. These bulk all solid state batteries are able to circumvent the problem of low battery capacities which thin film batteries have. The construction of an all solid state bulk battery consists as well of a positive and negative electrode, separated by a solid electrolyte as depicted in Figure 4. Due to the absence of a liquid electrolyte (that usually ensures the ionic connectivity, also for the often poor ion conducting (active) electrode particles) an additional ion conduction path is needed. Therefore, particles of the solid electrolyte can be added to the electrode with the purpose to raise the overall ionic conductivity. Furthermore, electronic conducting particles like graphite are needed if the electrode material exhibits a low electronic conductivity. The difference to an all solid state thin film battery is thereby, besides the thickness, the introduction of ionic

and/or electronic conducting particles, which form a percolation network that ensures the connectivity of the electrode material. In addition, a binder can be added to the electrode composition in order to establish the needed cohesion and buffer volume changes. A (modified) scheme of an all solid state bulk battery as used by Kotobuki et al. [90] is presented in Figure 4. The solid electrolyte can be formed solely from particles of a solid ion conductor or by solid ion conducting particles in an ion conducting matrix. This matrix can for instance be a polymer [91] or an amorphous material improving the mechanical or electrochemical characteristics of the solid electrolyte.

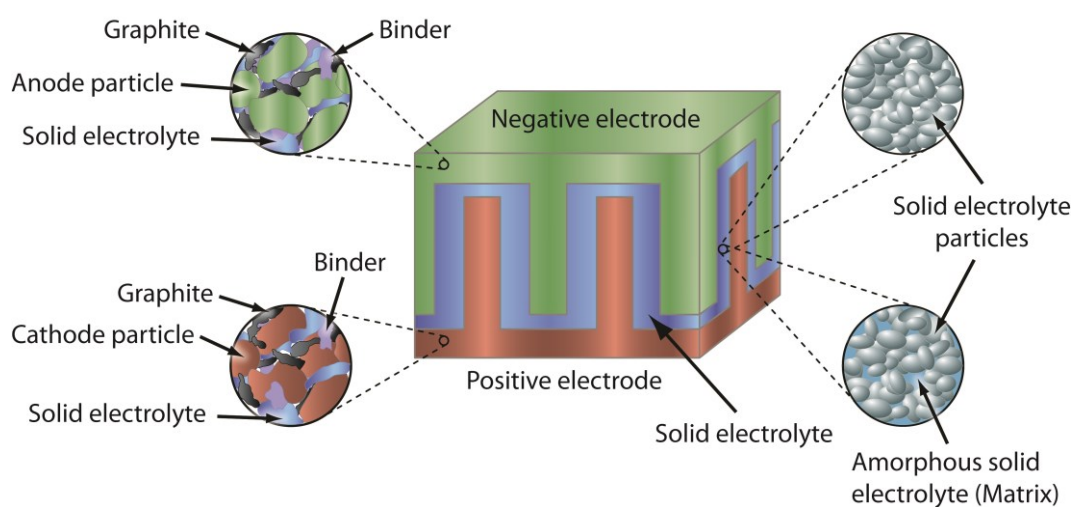


Figure 4: Scheme of an all solid state bulk battery after Ref. [92] (modified). The electrode electrolyte contact area is increased through the 3D structure of the battery. The magnifications show the compositions of the electrodes and of the solid electrolyte.

The 3D structure of the battery depicted in Figure 4 increases the contact area between the electrodes and the solid electrolyte. Thus, the resistance of the solid electrolyte is lowered and the accessible electrode surface is increased which leads to an accelerated ‘macroscopic kinetics’ (the improvement of the kinetics is due to the increased interface area) of the battery. Hence, the achievable maximum current is raised which is accompanied by a faster cycle rate of the cell. An overview of bulk solid state cells is given in Table 3. The potential used for the calculation of the energy density was estimated from the respective discharge behavior of the cell as it is shown in the reference.

Table 3: Overview of selected bulk all solid state lithium cells.

Anode	Electrolyte	Cathode	U/V	Cycles	Specific capacity / $\text{mAh}\cdot\text{g}^{-1}$	Energy density / $\text{Wh}\cdot\text{kg}^{-1}$	Ref.
Li/In	$\text{Li}_2\text{S}-\text{P}_2\text{S}_5$	TiS_3 [10 mg]	2.5 – 1.0	10	320	—	[93]
C [12 mg]	$\text{Li}_2\text{O}-\text{Li}_2\text{S}-\text{P}_2\text{S}_5$ [65 mg]	LiCoO_2 [16.2 mg]	4.1 – 3.0	—	107	65 (at 3.9 V)	[94]
$\text{Li}_4\text{Ti}_5\text{O}_{12}$ [27.7 mg]	$\text{Li}_2\text{S}-\text{P}_2\text{S}_5$	$\text{LiNi}_{0.8}\text{Co}_{0.15}\text{Al}_{0.05}$ O_2 coated with LiNbO_3 [31.3 mg]	3.0 – 0.5	1500*	134	102 (at 3.9 V)	[95]
Li/Al [#] [25.4 mg]	$\text{Li}_{3.25}\text{Ge}_{0.25}\text{P}_{0.75}\text{S}_4$ [70 mg]	S/CMK-3 [5 mg]	3.0 – 0.5	50	1000 [†]	75 (at 2.4 V)	[96]
In [#] [146.9mg]	$\text{Li}_2\text{S}-\text{P}_2\text{S}_5$ [140 mg]	LiCoO_2 [25 mg]	3.6 – 1.9	50	84	22 (at 3.3 V)	[97]
Li	$\text{Li}_7\text{La}_3\text{Zr}_2\text{O}_{12}:\text{Nb}$ [1 mm thick pellet]	$\text{LiCoO}_2/\text{Li}_3\text{BO}_3^\ddagger$	4.05 – 3.0	5	85	—	[98]
Li	$\text{Li}_7\text{La}_3\text{Zr}_2\text{O}_{12}:\text{Al}$	$\text{Cu}_{0.1}\text{V}_2\text{O}_5$	3.8 – 2.0	30	30	—	[99]
LiCoO_2	$\text{Li}_{0.35}\text{La}_{0.55}\text{TiO}_3$	$\text{Li}_4\text{Mn}_5\text{O}_{12}$	4.2 – 3.0	3	0.22	—	[90]

* Cycling was performed at 60 °C. [†]: This setup showed higher capacity than theoretically expected at the first cycles, the role of the CMK-3 is not entirely clear.

[‡] Li_3BO_3 was used as solid electrolyte in the cathode. [#]: The mass was calculated from the dimensions and density of the respective material.

A still unsolved problem in all solid state bulk batteries is poor cyclability and insufficient utilization of the active material of the electrode. Furthermore, the ratio of electrode material to solid electrolyte should have a high value. However, the ratio in bulk solid state batteries is unfavorable and leads to rather small energy densities. Another parameter that needs further improvement is the current density with which the bulk batteries can be cycled. These bulk batteries often run into a diffusion limitation (mainly of the active species), which has a big influence on the capacity of the cell. Due to high rates during cycling the capacity of the bulk battery cannot be fully utilized, thereby limiting the retrievable capacity. This diffusion limitation is the reason that the ratio of the electrode material compared to the solid electrolyte is so unfavorable. If the mass of the electrode material would be raised, in order to achieve higher energy densities, the electrode material would become thicker. As a consequence small current densities are needed for utilizing the whole active material. At high current densities the active material further away from the solid electrolyte would not be accessible due to the diffusion limitation.

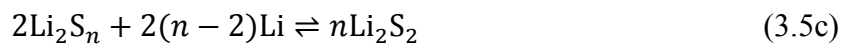
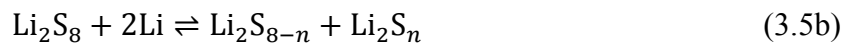
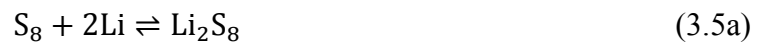
3.4 Ion conducting membranes

A possible way to combine the advantages of a battery with liquid electrolyte and the ion-selective characteristics of a solid ion conductor would be a solid electrolyte coated thin and porous separator. Introduced into a ‘conventional’ battery with liquid electrolyte the solid electrolyte membrane would allow the transport of lithium ions and would suppress the diffusion of other species from one electrode to another. Furthermore, the particulate electrode design with its high capacities compared to all solid state (thin film) batteries could be maintained. This setup would be particularly useful to prevent any kind of shuttle mechanism like it is observed in Li-S cells [100].

The electrochemical reaction that forms the basis of energy storage in Li-S cells is shown in Eq. 3.4. The thermodynamic cell voltage of this reaction is about 2.15 V [1].



In case of a conventional Li-S cell without ion-selective membrane, polysulfide species Li_2S_n ($8 \leq n \leq 3$) are soluble in the liquid organic electrolyte and are thereby able to migrate from the sulfur electrode to the lithium electrode (cf. Figure 5). The sulfur electrode itself consists mainly of cyclo- S_8 , which is the most stable allotrope at room temperature. Cyclo- S_8 reacts with lithium according to Eq. 3.5a to Li_2S_8 at the sulfur electrode Li_2S_8 is then able to dissolve into the liquid organic electrolyte, forming a catholyte. The solved Li_2S_8 can react further with lithium forming polysulfide species with shorter chain lengths (Eq. 3.5b) until the insoluble Li_2S_2 is formed (Eq. 3.5c). The reduction from insoluble Li_2S_2 to Li_2S (Eq. 3.5d) is kinetically slow due to the low electronic conductivity of Li_2S_2 .



In the end this leads to the deposition of electronically inactive Li_2S_2 and Li_2S at the anode and to a migration of the still solved polysulfide species between both electrodes. Besides the reduction of polysulfide species, oxidation is also possible, inverting the reactions shown in Eq. 3.5. The resulting cyclic behavior is called ‘shuttle mechanism’.

The shuttle mechanism in Li-S cells is a major problem and leads to a shortened life time of the battery and additionally to a low coulombic efficiency of the cell if no shuttle suppressing additives are used [100]. A schematic illustration of a Li-S cell with shuttle mechanism is shown in Figure 5. Depicted is the setup of a Li-S cell with a metallic lithium electrode on the left, which is ionically connected through the liquid electrolyte to a sulfur electrode on the right. Possible sulfur species that can occur are given on the sulfur electrode and are depicted between both electrodes. The detail of the sulfur electrode shows the composition, consisting of sulfur and graphite particles blended with a polymer binder. The circular arrows between the electrodes indicate the shuttle mechanism of the polysulfide species. Different polysulfide species have varying colors changing from reddish for Li_2S_8 to green and blue for the polysulfide species with shorter chain length. The color change is implied in the figure by the circular arrows.

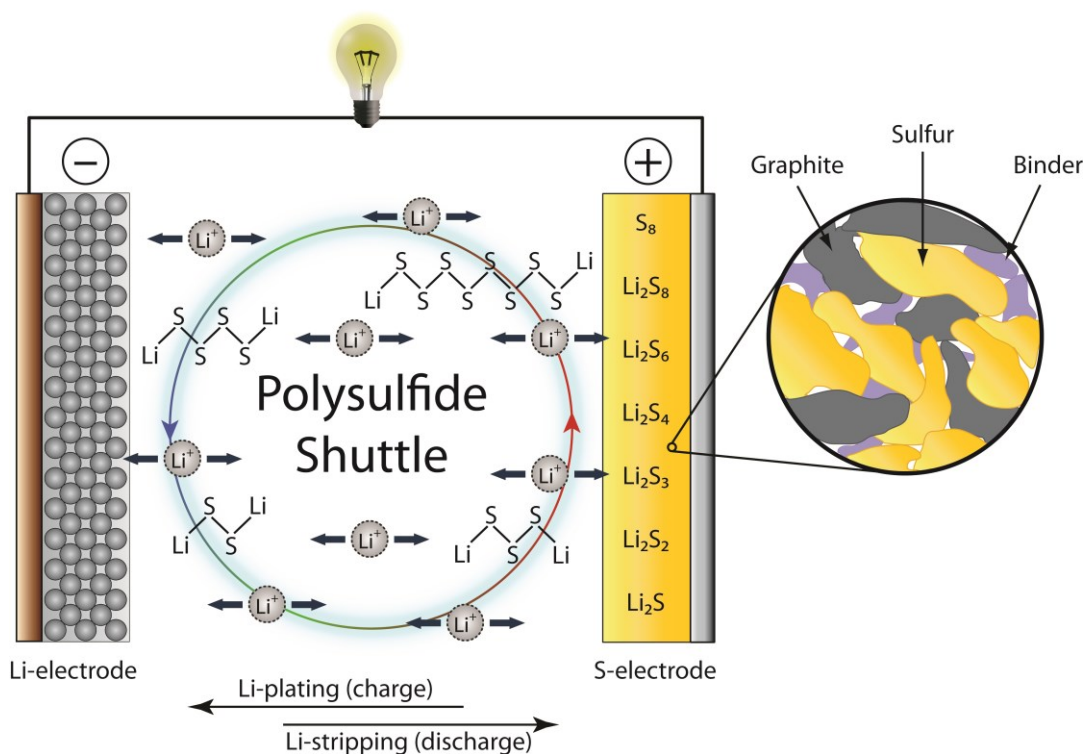


Figure 5: Illustration of the shuttle mechanism inside a Li-S cell.

Another problem arising in a Li-S cell can be the decomposition of the organic electrolyte at the lithium electrode, which can also lead to an early cell death. Despite their problems Li-S cells are regarded as a potential future lithium battery technology with a notable gravimetric energy density combined with the low resource costs of the sulfur electrode. The theoretical energy density of Li-S cells is about $2199 \text{ Wh}\cdot\text{l}^{-1}$ (based on the sum of the volumes of Li at the beginning and Li_2S at the end of discharge) [5] and the theoretical specific energy is $2567 \text{ Wh}\cdot\text{kg}^{-1}$ [5]. The theoretical gravimetric capacity is about $1675 \text{ mAh}\cdot\text{g}^{-1}$ [101, 102]. The practical values that can be achieved are lower. For the specific energy a practical value of up to $350 \text{ Wh}\cdot\text{kg}^{-1}$ was achieved and it is expected that values of about $600 \text{ Wh}\cdot\text{kg}^{-1}$ can be achieved in the near future [5] if the problems of electrolyte decomposition can be overcome.

The introduction of an impermeable ion-selective membrane in a Li-S cell with liquid electrolyte mechanically prevents the shuttle of polysulfide species from the sulfur electrode to the metallic lithium electrode. Such an assembly of a Li-S cell with an ion-selective membrane is shown schematically in Figure 6. The mechanical separation of the two electrode compartments allows the use of two different liquid electrolytes, facilitating the individual adjustment of the liquid electrolyte to the respective electrode. In contrast to an all solid state concept one thus evades the problem of a high interface resistance between the solid electrolyte and the active material of the electrodes. This improvement is at the expense of a newly introduced transfer resistance between the two liquid electrolytes and the solid electrolyte membrane $R_t(\text{I})$ and $R_t(\text{II})$ ($R_t(\text{I})$ and $R_t(\text{II})$ do not necessarily have the same values). Additionally, the resistance of the solid electrolyte (R_{SE}) needs to be taken into account. The catholyte is maintained but its volume expansion is restricted to the sulfur electrode compartment. The different polysulfide species are represented by their respective color in the frame of the sulfur electrode compartment.

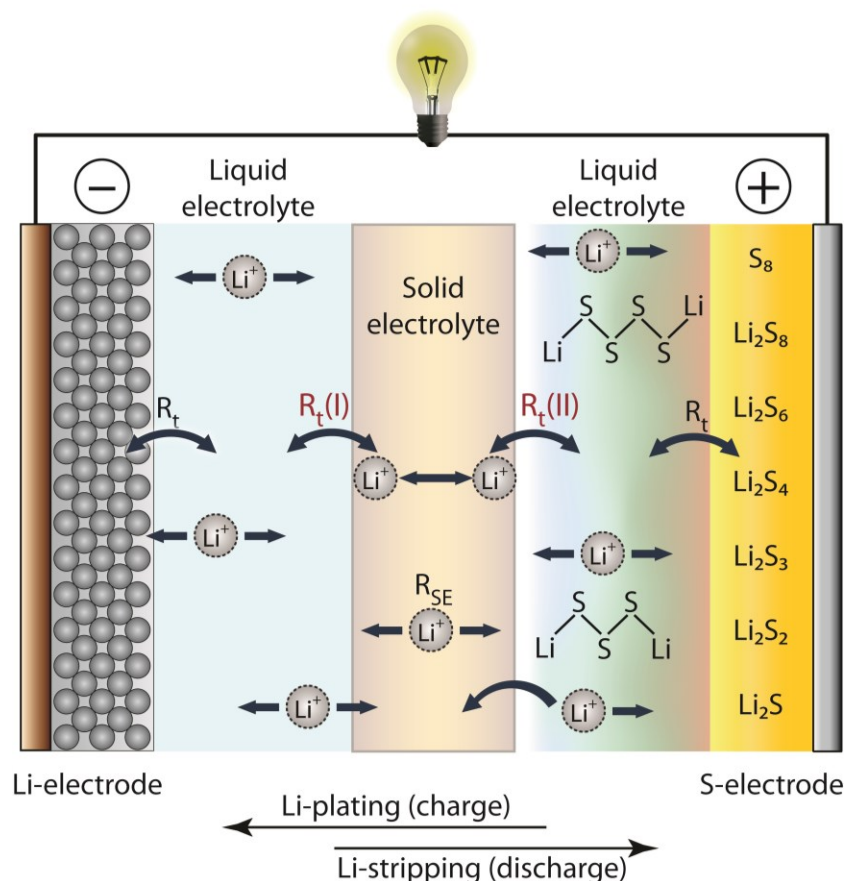


Figure 6: By insertion of a solid electrolyte membrane/solid electrolyte into a Li-S cell the shuttle mechanism is suppressed, without losing the advantage of a cell with liquid electrolyte.

The interface region between a solid and liquid electrolyte is illustrated in detail in Figure 7 [103]. The activation energy barriers for the charge transport are schematically depicted. The activation energy of ion conduction can be obtained from temperature dependent conductivity measurements of the single compound (solid electrolyte, liquid electrolyte). The activation energy of charge transfer at the interface between the solid and the liquid electrolyte can subsequently be determined by temperature dependent conductivity measurements of a solid-liquid cell. If possible a 4-point conductivity measurement should be conducted to exclude effects caused from the electrode/electrolyte contact.

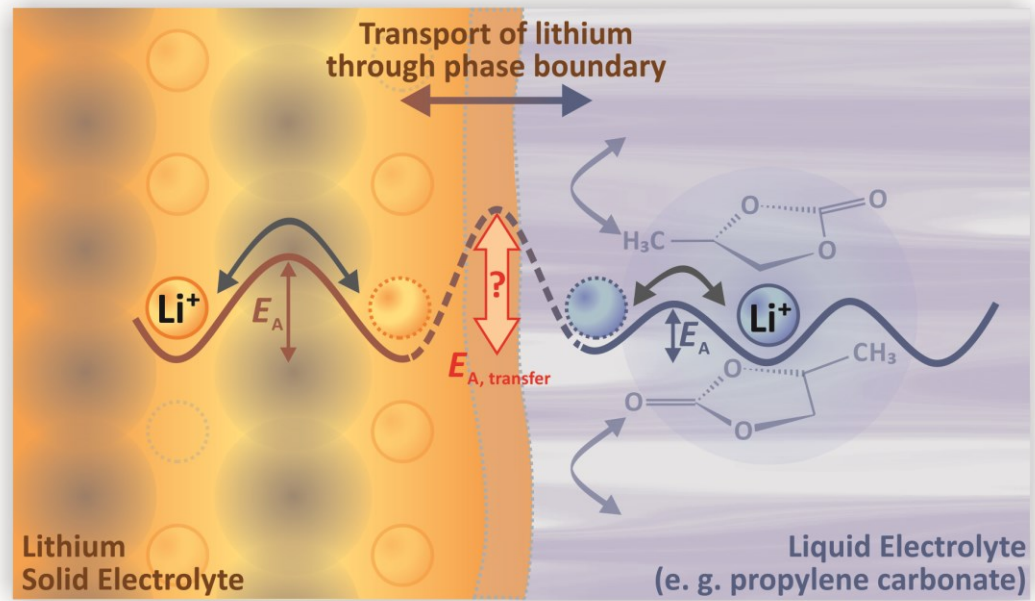


Figure 7: Detailed illustration of the interface between a solid and a liquid electrolyte [103] (acknowledgement Dr. Bjoern Luerßen/M. R. Busche). The activation energy barriers for the charge transfer in the solid electrolyte, the interface region and the liquid electrolyte are schematically depicted.

4. Experimental

4.1 Synthesis

Six different lithium ion conducting garnet-type phases were prepared out of the variety of garnet-type phases. These bulk materials were mainly prepared for the use as targets during the PLD process. The prepared garnet-type bulk materials can be classified in three groups. This classification is based upon the type(s) of cation(s) at the 16a site of the garnet type material as given in the subsequent listing. The 16a site can be occupied by cations with a charge number of +4 or +5, with a diameter of approximately 80 pm [39]. Two suitable cations are Zr^{4+} and Ta^{5+} with diameters of 86 pm [40] and 78 pm [104], respectively.

Group I: Ta^{5+} at the 16a position

Group II: Zr^{4+} at the 16a position

Group III: Zr^{4+} and Ta^{5+} at the 16a position

4.1.1 Synthesis of garnet-type bulk materials

The solid state synthesis of $\text{Li}_6\text{BaLa}_2\text{Ta}_2\text{O}_{12}$ was performed as described in literature [105]. Li_2CO_3 (99.998 %, Alfa Aesar, USA), BaCO_3 (99.95 %, Alfa Aesar), La_2O_3 (99.99 %, ChemPur GmbH, Germany; pre-dried at 900 °C for 12 h in air) and Ta_2O_5 (99.9 %, Chempur) were used for the high temperature synthesis of the garnet-type $\text{Li}_6\text{BaLa}_2\text{Ta}_2\text{O}_{12}$ material. To compensate lithium loss due to a volatile species as reported in Ref. [44] an excess of 10 mol% of the lithium source, based on lithium (excess of 5 mol% Li_2CO_3), was given to the starting materials that were mixed in the appropriate ratio.

An agate mortar was used for the initial manual mixing. In a subsequent step the grinded starting materials were ball milled (Pulverisette 5, Fritsch GmbH, Germany) in a zirconia grinding bowl with 3 mm zirconia balls for 4 h in 2-propanol with 160 rpm. Then the powder was dried using a rotary evaporator (Hei-VAP Advantage, Heidolph, Germany with a SC 920 pump from KNF, Germany) and calcined in a Heraeus chamber furnace (Heraeus, Germany) at 750 °C for 6 h in air. This was followed by another ball milling

step using the same parameters. The powdered material was heated to 1000 °C for 12 h in air in an open Al₂O₃ crucible. The material was initially uniaxially pressed to a pellet (custom made press) with 12.5 MPa. Afterwards, the pellet was compacted further with a pressure of 400 MPa by cold isostatic pressing (isostatic press, Loomis GmbH, Karlsruhe, Germany). The resulting pellet was covered in powder of the same composition and sintered at 1000 °C for 4 h in an open Al₂O₃ crucible at ambient atmosphere. The prepared pellet had a diameter of 7.66 mm and a thickness of 4.04 mm.

In addition to the pellet for electrochemical characterization, a PLD target was prepared as described above with the addition of an extra 5 mol% of Li₂O (99.5 %, Alfa Aesar) during the last milling step. The Li₂O addition was used to compensate a possible lithium loss during the PLD process. The obtained garnet-type material was pressed to a pellet with a diameter of 25 mm. Initially, the pellet was pressed uniaxially (custom made press) with 12.5 MPa and afterwards compacted with a pressure of 400 MPa by cold isostatic pressing (isostatic press, Loomis GmbH, Karlsruhe, Germany). The obtained pellet was covered in powder of the same composition and sintered at 1000 °C for 4 h in an open Al₂O₃ crucible in air. The resulting pellet had a final diameter of about 21 mm and was grinded down to a height of 6 mm (the laser spot size was measured at 6 mm height, thereby a target height of 6 mm ensures correct laser fluence settings). The prepared garnet-type Li₆BaLa₂Ta₂O₁₂ target was then transferred into a glovebox with argon atmosphere (Labmaster, MBraun, Germany) with less than 0.1 ppm residual H₂O and O₂ content. The glovebox was directly connected to the PLD chamber, thereby avoiding that the target material as well as the prepared thin films were exposed to air.

Besides garnet-type Li₆BaLa₂Ta₂O₁₂ (group I) other lithium ion conducting garnet-type materials with cubic structure and high lithium ion conductivity (cf. chapter 3.1) were prepared similarly:

- | | |
|------------|---|
| Group II: | • Li ₇ La ₃ Zr ₂ O ₁₂ stabilized by Ga ₂ O ₃ |
| Group III: | • Li _{6.5} La ₃ Zr _{1.5} Ta _{0.5} O ₁₂ additionally stabilized by Al ₂ O ₃ |
| | • Li _{6.5} La ₃ Zr _{1.5} Ta _{0.5} O ₁₂ |
| | • Li ₆ La ₃ Zr ₁ Ta ₁ O ₁₂ |
| | • Li _{5.5} La ₃ Zr _{0.5} Ta _{1.5} O ₁₂ |

The starting materials for the respective garnet-type material were mixed in the appropriate ratio with 10 mol% excess of lithium. The process is described in detail in literature [9, 39] and was analogous to the process described above for the garnet-type $\text{Li}_6\text{BaLa}_2\text{Ta}_2\text{O}_{12}$ material (temperatures during synthesis differed, but are given in [9, 39]).

An exception from the classical high temperature solid state synthesis was the preparation of $\text{Li}_7\text{La}_3\text{Zr}_2\text{O}_{12}$ stabilized by Ga_2O_3 . This garnet-type material was synthesized using a sol-gel approach as described in literature [41]. The material contained 1.0 mole Ga per one mole of $\text{Li}_7\text{La}_3\text{Zr}_2\text{O}_{12}$ and was prepared and kindly provided by Dr. Hany El Shinawi from our department.

4.1.2 Synthesis of garnet-type thin films

Garnet-type thin films were prepared by PLD. A KrF excimer laser (Compex 201F, Coherent, USA) with a wavelength of $\lambda = 248$ nm and a pulse duration of 25 ns was used for the process. Before ablation the PLD chamber was evacuated to at least $5 \cdot 10^{-5}$ mbar. The deposition process took place in pure $5 \cdot 10^{-2}$ mbar oxygen atmosphere (5N oxygen was used). For the deposition of a certain garnet-type thin film the appropriate garnet-type material was used as target. The distance between target and substrate was adjusted to 45 mm. The substrates were heated from the backside, by either a platinum ac heater or by an IR-laser heater, covering a temperature range from 530 °C to 620 °C. The temperatures stated either refer to a thermocouple inside the substrate holder directly behind the substrate or, in the case of the IR-laser heater, the temperature stated refers to a pyrometer adjusted to the backside of the stainless steel substrate holder. The laser fluence (laser energy divided by the irradiated area) was set by using a pyroelectric sensor.

Garnet-type thin films were deposited on different substrates, among these were MgO(100), indium tin oxide (ITO) and anodized aluminum oxide (AAO) substrates. The depositions on MgO(100) were divided into “single layer thin films”, which means that only “one” garnet-type material was deposited in one process and into “multilayer thin films”, denoting garnet-type films with alternating layers of different garnet-type phases. Besides $\text{Li}_6\text{BaLa}_2\text{Ta}_2\text{O}_{12}$, the deposition of all garnet-type materials was performed on

MgO(100) substrates that were initially covered with a thin (< 100 nm) $\text{Li}_6\text{BaLa}_2\text{Ta}_2\text{O}_{12}$ garnet-type thin film as a buffer layer to avoid cracking of the respective garnet-type thin film. For the multilayer thin films a simplified notation is introduced at this point:

$$(X|Y) \times n \quad (4.1)$$

Thereby X denotes the first garnet-type material that was deposited onto the substrate and Y denotes the second garnet-type thin film that was applied. If the garnet-type multilayer structure contains no $\text{Li}_6\text{BaLa}_2\text{Ta}_2\text{O}_{12}$ the multilayer structure was deposited onto a $\text{Li}_6\text{BaLa}_2\text{Ta}_2\text{O}_{12}$ covered MgO(100) substrate. The variable n gives the amount of bilayers. If not mentioned separately all layers of one multilayer structure were prepared using a constant amount of laser pulses, leading to the same thickness for each layer. For instance a multilayer thin film consisting of alternating layers of $\text{Li}_6\text{BaLa}_2\text{Ta}_2\text{O}_{12}$ and $\text{Li}_6\text{La}_3\text{Zr}_1\text{Ta}_1\text{O}_{12}$ with two $\text{Li}_6\text{BaLa}_2\text{Ta}_2\text{O}_{12}$ and two $\text{Li}_6\text{La}_3\text{Zr}_1\text{Ta}_1\text{O}_{12}$ layers would be depicted by $(\text{Li}_6\text{BaLa}_2\text{Ta}_2\text{O}_{12}|\text{Li}_6\text{La}_3\text{Zr}_1\text{Ta}_1\text{O}_{12}) \times 2$.

The thin films deposited on MgO(100) are suitable for lateral conductivity measurements, whereas the ones on ITO and platinum coated MgO(100) substrates are suitable for conductivity measurements in axial geometry. The MgO(100) substrate was used as a standard substrate for the deposition of garnet-type thin films as it is a good compromise between matching lattice parameters and cost efficiency (the possibly better-suited GGG substrates are approximately three times more expensive than MgO substrates). The cubic MgO crystal structure (rock salt-type) has a lattice parameter of $a_{\text{MgO}} = 421$ pm. The unit cell of MgO multiplied by three (1263 pm) equals approximately the lattice constant of garnet-type $\text{Li}_6\text{BaLa}_2\text{Ta}_2\text{O}_{12}$, $a_{\text{LBLTO}} = 1296$ pm [44] (3:1 commensurability), leading to a misfit (f) of -2.5% , according to Eq. 4.1, for $\text{Li}_6\text{BaLa}_2\text{Ta}_2\text{O}_{12}$ on a MgO(100) substrate. It is assumed that the $\text{Li}_6\text{BaLa}_2\text{Ta}_2\text{O}_{12}$ thin film undergoes an elastic deformation on top of the inelastic MgO(100) single crystal. d_{hkl} gives the length of the lattice plane spacing. For simplicity a (100) orientation of the garnet-type material was assumed.

$$f_{\text{LBLTO/MgO}} = \frac{d_{100}(\text{MgO}) - d_{100}(\text{LBLTO})}{d_{100}(\text{LBLTO})} \quad (4.1)$$

A misfit of -2.5% means that the thin film is compressed parallel to the substrate (xy -plane) and elongated in z -direction. This probably leads to a semicoherent interface between the MgO substrate and the $\text{Li}_6\text{BaLa}_2\text{Ta}_2\text{O}_{12}$ thin film. The elastic compression of the thin film ($\varepsilon_{\text{LBLTO}}$) is equal the calculated misfit due to the assumed inelasticity of the substrate (Eq 4.2). Furthermore, it is assumed that the misfit of the cubic $\text{Li}_6\text{BaLa}_2\text{Ta}_2\text{O}_{12}$ is identical in x - and y -direction.

$$\begin{aligned}\varepsilon_{\text{LBLTO}} &= f_{\text{LBLTO/MgO}} \\ \varepsilon_{\text{MgO}} &= 0\end{aligned}\tag{4.2}$$

It was already shown that strain can influence ionic conductivity, leading to a reduced ionic conductivity in the compressively strained plane [106-111]. A detailed discussion of this topic is given in [112].

Another possible substrate for lithium ion conducting garnet-type materials is porous AAO. By deposition of a garnet-type thin film on top of the AAO substrate an ion-selective membrane is created, which can then be used in hybrid cells.

4.1.2.1 Single layer thin films

Single layer thin films were prepared on various substrates such as MgO(100), ITO, Ohara electrolyte and AAO. The following targets were used yielding the corresponding garnet-type thin film:

- | | |
|------------|--|
| Group I: | • $\text{Li}_6\text{BaLa}_2\text{Ta}_2\text{O}_{12}$ |
| Group II: | • $\text{Li}_7\text{La}_3\text{Zr}_2\text{O}_{12}$ stabilized by Ga_2O_3 |
| Group III: | • $\text{Li}_{6.5}\text{La}_3\text{Zr}_{1.5}\text{Ta}_{0.5}\text{O}_{12}$ additionally stabilized by Al_2O_3 |
| | • $\text{Li}_{6.5}\text{La}_3\text{Zr}_{1.5}\text{Ta}_{0.5}\text{O}_{12}$ |
| | • $\text{Li}_6\text{La}_3\text{Zr}_1\text{Ta}_1\text{O}_{12}$ |
| | • $\text{Li}_{5.5}\text{La}_3\text{Zr}_{0.5}\text{Ta}_{1.5}\text{O}_{12}$ |

In case of $\text{Li}_6\text{BaLa}_2\text{Ta}_2\text{O}_{12}$ the garnet-type thin films were directly deposited onto an untreated MgO(100) substrate. All other remaining garnet-type phases were deposited onto a MgO(100) substrate that was previously coated with a thin layer (< 100 nm) of $\text{Li}_6\text{BaLa}_2\text{Ta}_2\text{O}_{12}$.

The substrates were glued to the substrate holder by conductive silver paint. The substrate to target distance was 45 mm. Before the ablation process was carried out the PLD chamber was evacuated to $5 \cdot 10^{-5}$ mbar. Thereafter, a mass flow controller pumped oxygen into the recipient setting the pressure to $5 \cdot 10^{-2}$ mbar. The substrate was simultaneously heated from the backside by a platinum ac-heater to the desired temperature ($\vartheta = 530$ °C - 600 °C) with a rate of 10 °C \cdot min $^{-1}$. The amount of laser pulses was set according to the desired film thickness. The frequency of the KrF laser was 10 Hz for all ablation processes. The laser fluence was adjusted to values between 2 J \cdot cm $^{-2}$ and 4 J \cdot cm $^{-2}$. After deposition, the O_2 pressure was raised to 0.1 mbar, while at the same time the temperature was lowered by 10 °C \cdot min $^{-1}$ until 300 °C were reached. All deposition parameters are summarized in Table 4.

Table 4: Summarized process parameters for the deposition of garnet-type single layer thin films by PLD.

Prior to deposition	p / mbar	$5 \cdot 10^{-5}$
	Target substrate distance / mm	45
Deposition	p / mbar	$5 \cdot 10^{-2}$
	Gas atmosphere	O ₂ (5N)
	T / °C	530 °C – 600 °C
	Laser fluence / J·cm ⁻²	2 – 4
	Laser frequency / Hz	10
After Deposition	p / mbar	0.1
	Gas atmosphere	O ₂ (5N)
	Temperature ramp / °C·min ⁻¹	10
	AC heater switch off temperature / °C	300

4.1.2.2 Multilayer thin films

The deposition of multilayer thin films was performed exclusively on MgO(100) substrates with a thin Li₆BaLa₂Ta₂O₁₂ layer using the IR-laser heater. The substrates were attached to the substrate holder by conductive silver paint. One small corner of the substrates was covered with a piece of aluminum foil in order to determine the film thickness of the deposited layer. Three different garnet-type targets, representing all three groups, were used for the deposition of garnet-type multilayers:

- Group I: • Li₆BaLa₂Ta₂O₁₂
- Group II: • Li₇La₃Zr₂O₁₂ stabilized by Ga₂O₃
- Group III: • Li_{6.5}La₃Zr_{1.5}Ta_{0.5}O₁₂ additionally stabilized by Al₂O₃

Prior to the deposition the recipient of the PLD was evacuated to $1 \cdot 10^{-5}$ mbar. The deposition process took place in pure $5 \cdot 10^{-2}$ mbar oxygen atmosphere. The Li₆BaLa₂Ta₂O₁₂ garnet-type layers were prepared at 550 °C. For comparison all other garnet-type layers were prepared at 600 °C. Only one (Li_{6.5}La₃Zr_{1.5}Ta_{0.5}O₁₂:Al₂O₃|Li₇La₃Zr₂O₁₂:Ga₂O₃)×5 multilayer thin film was prepared at

620 °C to explore a possible temperature influence during deposition. Depositions at this temperature are critical as 620 °C is close to the decomposition temperature of the garnet-type thin films. At temperatures higher than 620 °C the binary metal oxides and other mixed metal oxides are often obtained in addition to the garnet-type phase as determined by X-ray diffraction. The fluence of the laser for the deposition of all garnet-type multilayer thin films was set to 4 J·cm⁻². The number of pulses taken was adjusted to the desired thickness of the thin film (around 40,000 pulses usually). The laser frequency was set to 10 Hz. The temperature ramp after deposition was set to 10 °C·min⁻¹ until a temperature of 350 °C was reached, then the IR-laser heater was switched off. The pyrometer used for the temperature control has a lower limit of 320 °C. That is the reason why temperatures lower than this value cannot be detected. Hence, lower temperatures cannot be achieved using the IR-laser heater. All deposition parameters are summarized in Table 5.

Table 5: Summarized process parameters for deposition of garnet-type multilayer thin films by PLD.

Prior to deposition	Substrate	MgO(100)
	p / mbar	$1 \cdot 10^{-5}$
	Target substrate distance / mm	45
Deposition	p / mbar	$5 \cdot 10^{-2}$
	Gas atmosphere	O ₂ (5N)
	ϑ / °C	550 °C – 620 °C
	Laser fluence / J·cm ⁻²	4
	Laser frequency / Hz	10
After Deposition	p / mbar	0.1
	Gas atmosphere	O ₂ (5N)
	Temperature ramp / °C·min ⁻¹	10
	IR heater switch off temperature / °C	350

4.1.2.3 Garnet-type membranes

The deposition of garnet-type $\text{Li}_6\text{BaLa}_2\text{Ta}_2\text{O}_{12}$ thin films on porous AAO was carried out using PLD. The process is schematically shown in Figure 6. The laser fluence was adjusted to $3 \text{ J}\cdot\text{cm}^{-2}$ and the frequency to 10 Hz. The target rotation was set to 19 rpm and a target wobble ensured a uniform ablation of the garnet-type target material. Prior to the PLD process the PLD chamber was evacuated to $5\cdot 10^{-5}$ mbar. The process itself was conducted under a $5\cdot 10^{-2}$ mbar oxygen atmosphere with 45 mm distance between target and substrate. As substrate anodized aluminum oxide (AAO; AnodiscTM, AnoporeTM, by Whatman, USA) with a diameter of 13 mm and a pore diameter of 100 nm was attached to the substrate holder and fixed by a round shadow mask. The shadow mask had a cut out circle of 12 mm in diameter and was screwed to the substrate holder. The 60 μm thick substrates were heated to 860 $^{\circ}\text{C}$ by an IR-laser from the backside. This temperature was measured at the backside of the stainless steel substrate holder using a pyrometer and was therefore not identical with the temperature at the substrate surface. It is assumed that the temperature at the substrate surface was kept between 500 $^{\circ}\text{C}$ and 650 $^{\circ}\text{C}$. The prepared thin films had thicknesses between 0.5 μm and 2 μm .

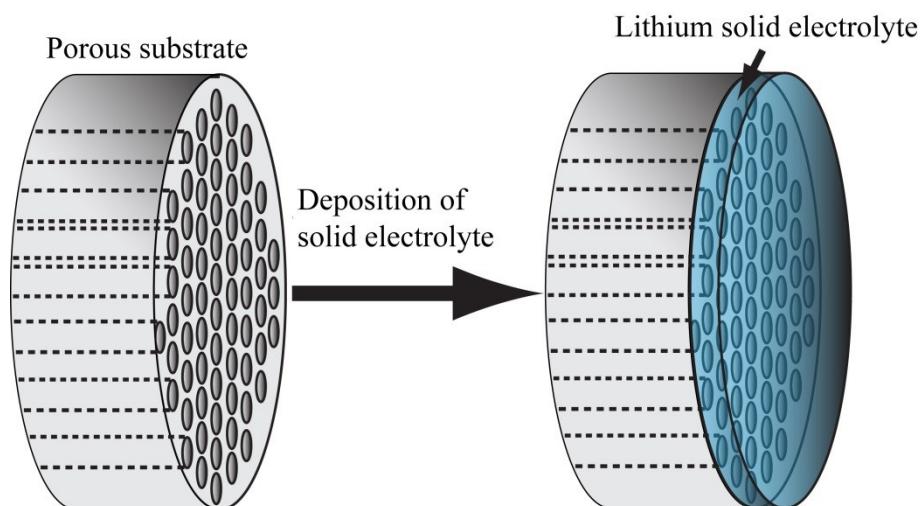


Figure 8: Fabrication of an ion-selective membrane by deposition of an ion conducting thin film on top of a porous membrane.

As an uncoated area still remained at the fringe of the AAO disc due to the shadow mask, a polymer foil was applied with an office laminator (Otto Office, Germany) to enable

permeation measurements of the $\text{Li}_6\text{BaLa}_2\text{Ta}_2\text{O}_{12}$ coated AAO disc. The lamination process is depicted in Figure 9 as a process chart with the associated photographs shown on the right hand side. In step 1-2 the porous AAO substrate was coated by lithium ion conducting $\text{Li}_6\text{BaLa}_2\text{Ta}_2\text{O}_{12}$. In step 3 a circle with a diameter of 10 mm was cut out of the lamination foil. The $\text{Li}_6\text{BaLa}_2\text{Ta}_2\text{O}_{12}$ coated AAO was placed between the lamination foils. The lamination foil consisted of two different polymers. The inside of the lamination foil was made out of a thermoplastic with a low melting point (ethylene vinyl acetate - EVA). The outside of the lamination foil was made out of a more rigid polymer with a higher melting point (polyethylene terephthalate - PET). In step 4 the lamination pouch was transferred to a laminator, which heats the lamination pouch between two rolls that apply pressure during the lamination process. Thereby, the two EVA coatings fused with each other and adhered to the $\text{Li}_6\text{BaLa}_2\text{Ta}_2\text{O}_{12}$ disc. After lamination the AAO disc is mechanically more stable and can even be bent, which would normally cause the AAO disc to break if no polymer support ring had been applied.

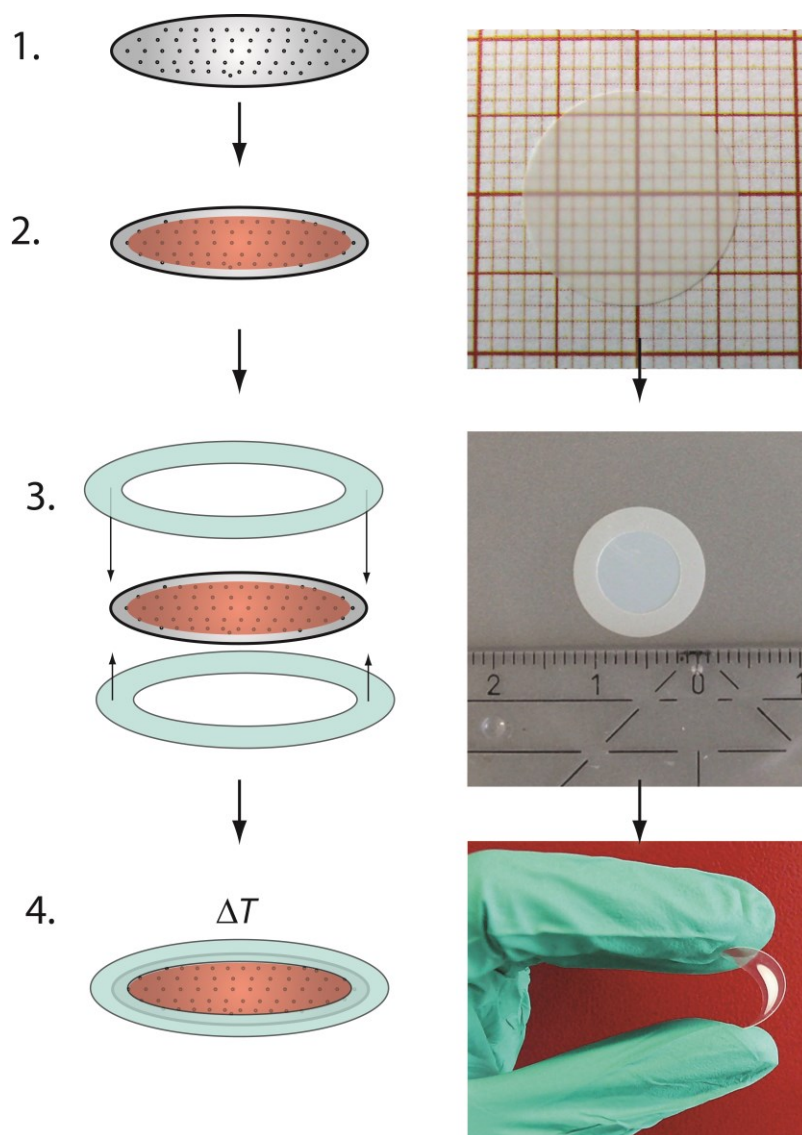


Figure 9: Lamination of a $\text{Li}_6\text{BaLa}_2\text{O}_{12}$ -coated anodized aluminum oxide disc with an EVA/PET foil. Step 1-2: AAO is coated with a thin LBLTO layer. Step 3-4: a circle is cut out of the polymer foils and the AAO is put in between. Thereafter the formed polymer pouch is heated by a laminator.

4.2 Characterization

4.2.1 X-ray diffraction

The obtained bulk and thin film samples were characterized by x-ray diffraction (XRD; Siemens D500, now Bruker AXS GmbH, Germany, Cu-K $\alpha_{1,2}$ -radiation; X'Pert HighScore Plus, by PANalytical B. V., Netherlands was used as software for XRD data analysis). For this, the respective bulk or thin film sample was taken out of the glovebox and brought to atmosphere. Thereafter, the sample was immediately placed inside the XRD. Bulk material samples were measured in a range from $2\theta = 15^\circ - 70^\circ$ and garnet-type thin film samples were measured from $2\theta = 15^\circ - 40^\circ$, avoiding the single crystal reflex of MgO(100) at $2\theta = 42.9^\circ$.

4.2.2 Conductivity measurements of garnet-type bulk material

Three different types of conductivity measurements (electrochemical impedance spectroscopy, dc measurements with reversible electrodes, and Hebb-Wagner polarization) were performed in order to differentiate the ionic conductivity from the electron hole conductivity of a Li₆BaLa₂Ta₂O₁₂ garnet-type bulk sample. The garnet-type phases of Li_{6.5}La₃Ta_{0.5}Zr_{1.5}O₁₂ [39] were additionally stabilized by Al₂O₃, Li₇La₃Zr₂O₁₂ [41] which had been stabilized by Ga₂O₃, Li_{6.5}La₃Zr_{1.5}Ta_{0.5}O₁₂ [39], Li₆La₃Zr₁Ta₁O₁₂ [39] and Li_{5.5}La₃Zr_{0.5}Ta_{1.5}O₁₂ [39] were not characterized as their properties are already known in literature [39, 41].

In a first step the total conductivity of the Li₆BaLa₂Ta₂O₁₂ garnet-type bulk sample was measured by electrochemical impedance spectroscopy (EIS) with a SP-300 (Bio-Logic, France) in the frequency range from 7 MHz to 1 Hz. The fit of the obtained impedance data with an equivalent circuit was performed with ZSimpWin Version 3.21 (ZSimpWin, EChem Software, USA). For the impedance measurements lithium electrodes (>98 %, Chemetal now Rockwood Lithium, Germany) were pressed from both sides on the whole circular surfaces of the pellet (diameter of 7.66 mm, thickness without electrodes of 4.04 mm). The EIS measurements were performed in gas-tight pouches, which were sealed under argon atmosphere in a glovebox. In an additional step the impedance of the sample was determined as a function of temperature in order to determine the activation

energy of the charge transfer from the slope of $\ln(\sigma T)$ versus $1/T$. Therefore, a temperature chamber (WTL 64, Weiss Technik, Germany) was used in a temperature range from $-40\text{ }^{\circ}\text{C}$ up to $80\text{ }^{\circ}\text{C}$. An electrochemical impedance measurement was performed every $10\text{ }^{\circ}\text{C}$ (an additional measurement was performed at $25\text{ }^{\circ}\text{C}$).

In order to verify the values obtained by the EIS experiments, dc measurements were conducted. Here, the garnet-type $\text{Li}_6\text{BaLa}_2\text{Ta}_2\text{O}_{12}$ sample with Li-electrodes was measured from -1 V to 1 V at $25\text{ }^{\circ}\text{C}$ using an SP-300 as potentiostat.

The partial electronic conductivity, as well as the transference numbers (t_i), of a mixed ionic-electronic conductor can be determined by the Hebb-Wagner [113, 114] polarization technique. In this dc technique the ionic current is suppressed. Hence, the measured steady state current is only caused by electrons and/or electron holes. During this experiment, the current transient is measured at an applied constant voltage. For this type of measurement two different electrodes are necessary: One reversible electrode for the mobile ionic species which also acts as chemical potential reference and one lithium ion blocking electrode which is electron-conducting, electrochemically inert and should not act as Schottky barrier. In the case of cation-conducting solid electrolytes the reversible electrode is usually made of the parent metal (Li in the present case), and thus also provides a standard reference potential for the blocking electrode.

For the Hebb-Wagner measurements a lithium reference electrode was pressed on one side of the pellet and a carbon electrode was attached to the other side. The carbon electrode was deposited on the pellet by physical vapor deposition (carbon coater, custom made). The carbon electrode proved to be better suited than Ni or Au electrodes. Measurements were performed in the potential range of $+2.85$ to $+4.3\text{ V}$ versus Li^+/Li , which corresponds to the typical condition of an electrolyte between a Li anode and a cathode in the charge state of a battery. The Hebb-Wagner cell was transferred into a gas-tight Swagelok test cell and investigated with a Keithley Model 6430 Sub-Femtoamp Remote SourceMeter (Keithley Instruments, USA, maximum resolution of 10 aA). The Swagelok cell was assembled under argon gas atmosphere and finally placed in a Faraday cage, protecting the low current measurement from electrical noise. When a steady state current at given potential was achieved a measurement point was taken from which the partial electronic conductivity was calculated.

The setup used for EIS and dc polarization experiments with lithium electrodes is schematically illustrated in Figure 10 a). The arrangement for the Hebb-Wagner polarization is illustrated in Figure 10 b). The depicted arrows show either that this species can reversibly be exchanged with the electrodes (solid line) or that the species cannot be supplied by the electrode material (dotted line with bar at the beginning). The arrow heads show the direction of the driving force for the respective species under measurement conditions.

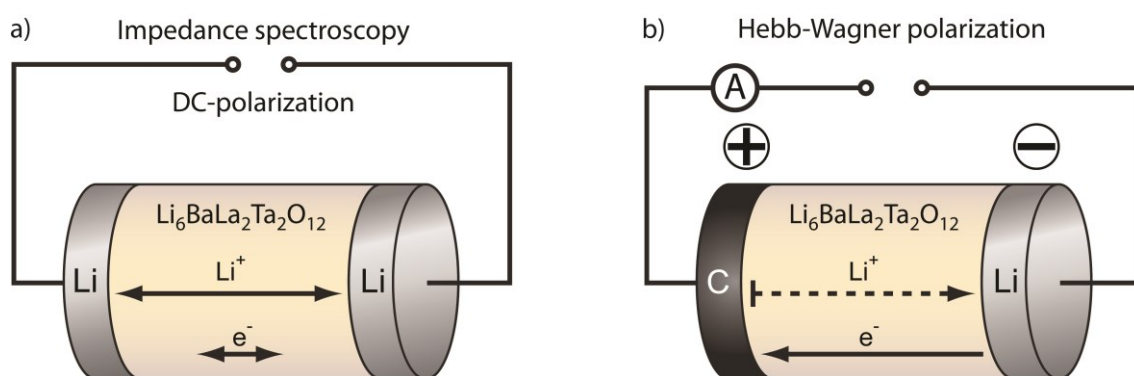


Figure 10: Measurement setup for EIS and dc polarization of a $\text{Li}_6\text{BaLa}_2\text{Ta}_2\text{O}_{12}$ bulk sample with lithium electrodes is shown in a). Measurement setup for Hebb-Wagner polarization of a $\text{Li}_6\text{BaLa}_2\text{Ta}_2\text{O}_{12}$ bulk sample with a carbon electrode on the left hand side and a lithium electrode on the right hand side is shown in b). The polarization of the carbon electrode was positive referred to the lithium electrode.

4.3 Characterization of garnet-type thin films

The following chapters briefly describe the techniques applied to characterize the different garnet-type thin films regarding their structural and electrochemical properties.

4.3.1 Scanning electron microscopy

A Merlin (Zeiss, Germany) scanning electron microscope (SEM) was used for the investigation of garnet-type thin film materials. Besides garnet-type single layer thin films, multilayer thin films and membranes were investigated.

In addition to regular “image” generation measurements in situ dc polarization measurements of a garnet-type thin film were realized and observed using a Leo Gemini 982 (Zeiss, Germany). For these measurements a platinum microelectrode and a broad metallic lithium electrode were applied to the $\text{Li}_6\text{BaLa}_2\text{Ta}_2\text{O}_{12}$ thin film. The platinum electrode was polarized negatively versus the lithium electrode. During this measurement the $\text{Li}_6\text{BaLa}_2\text{Ta}_2\text{O}_{12}$ garnet-type thin film on a $\text{MgO}(100)$ substrate was heated from below to 36°C for an increased conductivity. The setup used for the dc polarization measurement is shown in Figure 11. The measurements were conducted in cooperation with Rabea Dippel from our department.

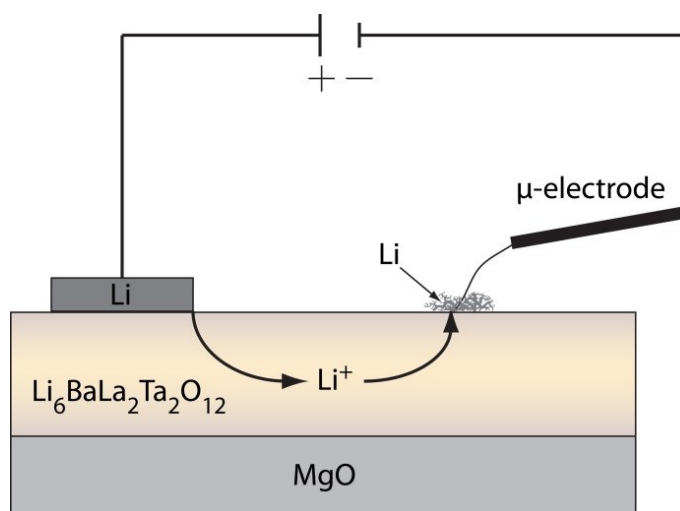


Figure 11: Setup for an in situ polarization experiment during SEM investigation.

4.3.2 Transmission electron microscopy

Transmission electron microscopy (TEM) measurements were performed at the “Institute of Nanotechnology” (INT) at the “Karlsruhe Institute of Technology” (KIT) by the group of Dr. Christian Kübel. Two types of samples were characterized by TEM. A multilayer garnet-type thin film sample consisting of $(\text{Li}_6\text{BaLa}_2\text{Ta}_2\text{O}_{12}|\text{Li}_{6.5}\text{La}_3\text{Zr}_{1.5}\text{Ta}_{0.5}\text{O}_{12}:\text{Al}_2\text{O}_3)\times 10$ and a prototype thin film battery with a layered $\text{Li}_6\text{BaLa}_2\text{Ta}_2\text{O}_{12}|\text{LiFePO}_4|\text{Pt}|\text{Cu}$ structure built onto a silicon substrate.

Both samples were prepared by focused ion beam (FIB) using a Zeiss Auriga 60 SEM (Carl Zeiss, Germany) and a FEI Strata 400S dual beam (FEI, USA) FIB. The FEI Strata 400S used a focused gallium ion beam to cut a predefined pattern out of the sample. Subsequently, a thin layer of platinum was deposited on top of the sample, fusing it with a manipulator, in order to place it onto a TEM grid. The deposition of platinum was performed inside the SEM. For the TEM measurements a Titan 80–300 (FEI) was used.

4.3.3 Conductivity measurements in lateral geometry

The conductivity of the garnet-type thin films was determined by lateral EIS and dc polarization measurements. For those measurements electrodes were deposited by thermal evaporation on top of the garnet-type thin film material. A mask was used during the thermal evaporation process in order to achieve reproducible electrodes on each garnet-type thin film. The deposited electrodes had a length of 1 cm with a gap of 1 mm. Mainly lithium and gold were used as electrode materials.

The EIS measurements were performed in gas-tight pouches, which were sealed under argon atmosphere in a glovebox. In an additional step the impedance of the sample was determined as a function of temperature to determine the activation energy of the charge transfer from the slope of $\ln(\sigma T)$ versus $1/T$. Therefore, a temperature chamber (WTL 64) was used in a temperature range from $-30\text{ }^\circ\text{C}$ to $70\text{ }^\circ\text{C}$. For EIS as well as for dc polarization measurements a SP-300 was used in a frequency range from 1 MHz to 2 Hz. The fit of the obtained impedance data with an equivalent circuit was either performed with ZSimpWin or with EC-Lab from Bio-Logic. dc polarization experiments were

performed on garnet-type $\text{Li}_6\text{BaLa}_2\text{Ta}_2\text{O}_{12}$ thin films using lithium electrodes from -1 V to 1 V.

The setup used for the garnet-type thin film conductivity measurements is schematically shown in Figure 12.

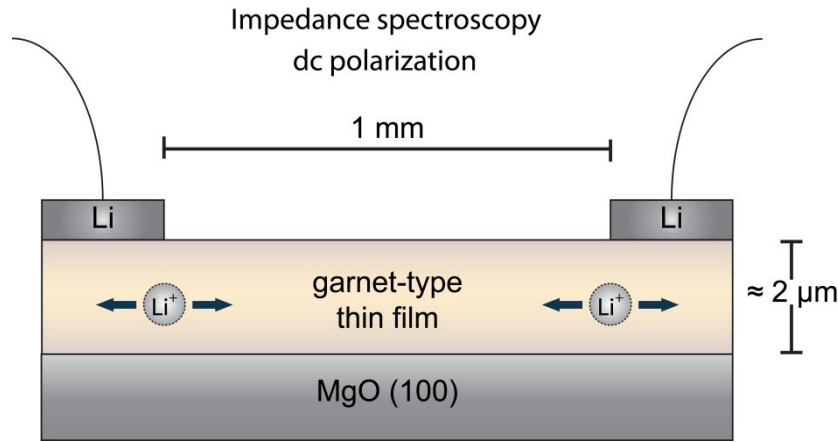


Figure 12: Schematic setup of the EIS and dc polarization measurements using reversible Li-electrodes.

4.3.4 Conductivity measurements in axial geometry

Complementary to the conductivity measurements in lateral geometry electrochemical impedance spectroscopy and dc polarization measurements were realized in axial geometry. For this purpose garnet-type thin films were deposited on conductive substrates as platinum coated $\text{MgO}(100)$ or on indium tin oxide (ITO), whereby a corner of the substrate was covered by a mask so that the back electrode contact of the thin film was still accessible. Thereafter, 26 circular gold electrodes with a diameter of 0.9 mm were deposited on the sample by thermal vapor deposition. A sample prepared in that manner can be seen in Figure 13. On the upper right corner the ITO substrate was covered, to avoid deposition of garnet-type material. The remaining sample area was covered with a garnet-type thin film. The yellowish color of the sample arises from reduction of the ITO substrate during the PLD process, as this was observed as well for an ITO sample which was heated under comparable experimental conditions (same gas atmosphere, $5 \cdot 10^{-2}$ mbar

O₂) for 30 minutes. The gray-silver speckles are a result of conductive silver paint residue on the backside of the substrate. The conductivity measurements were performed in a temperature range of $\vartheta = 0\text{ }^{\circ}\text{C}$ up to $\vartheta = 70\text{ }^{\circ}\text{C}$.

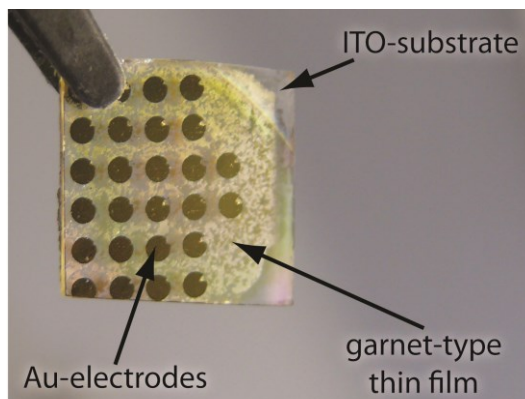


Figure 13: Garnet-type thin film with circular gold electrodes on top of an ITO substrate for axial conductivity measurements.

Different measurement techniques were applied in order to obtain conductivities, activation energies of the charge transfer and partial electronic conductivities. By electrochemical impedance spectroscopy the total conductivity of the corresponding sample was obtained. The activation energy of the charge transfer was received from impedance measurements at different temperatures. For impedance measurements a Novocontrol Alpha-AT (Novocontrol Technologies GmbH & Co. KG, Germany) was used. Furthermore, dc polarization was applied using a Keithley model 6430 Sub-Femtoamp Remote SourceMeter to determine the partial electron/hole conductivity. Because partially reduced ITO might be a reversible electrode for lithium the ITO electrode was polarized positively versus a circular gold electrode at the beginning of the experiment. Afterwards the polarity of the electrodes was inverted. Shielded coaxial cables were used during the measurements. As the samples always remained inside the glove box under argon atmosphere the cables were passed through a gas tight flange.

4.3.5 Ion-selective membranes

For the purpose of checking permeation across the laminated ion-selective membranes, a dye concentration experiment was set up. The idea was to directly visualize permeation through the membrane, if existent. Therefore, the laminated membrane was used like a diaphragm, connecting two glass tubes with each other. A dye (methyl red) was brought in contact with the membrane from one side, on the other side a colorless liquid (2-propanol) was used.

The equipment for the permeation experiment is shown in Figure 14 a). The laminated membrane was embedded between two flat gaskets (Figure 14 b). The flat gaskets were pushed together by the glass tubes which were themselves squeezed together by a clamp connector (Figure 14 c). The clamp connector was locked using a hose clamp. The flange of the glass tubes needed to have a bigger inner diameter than the membrane itself (AAO: $\varnothing = 13$ mm, flange of glass tube inner diameter: $\varnothing = 15$ mm), so that no direct pressure was applied to the membrane. In a next step methyl red was inserted into one glass tube (Figure 14 d) and 2-propanol was inserted in the other glass tube. Both glass tubes were sealed with a plug. Thereby, the membrane had only contact to methyl red (solved in ethanol) and 2-propanol, and was not exposed to atmosphere during the experiment. In Figure 14 e) the automated measurement setup for permeation testing is shown. A webcam connected to a laptop recorded pictures with timestamps of the experiment in regular time intervals.

The most fragile part of the construction was the boundary between lamination foil and AAO disc. The liquid phase tended to penetrate the space between the lamination foil and the AAO disc and could thereby flow around the pore-blocking $\text{Li}_6\text{BaLa}_2\text{Ta}_2\text{O}_{12}$ layer. The pores not covered by the garnet-type thin film were thereby accessible to the liquid phase. Hence, the ion-selective membrane was bypassed. As countermeasure a two layer sealing was applied between the AAO and the lamination foil. The first layer consisted of super glue with low viscosity (Sekundenkleber blitzschnell Pipette, UHU, Germany), sealing the pores between the lamination foil and the AAO disc. The second layer consisted of silicone rubber (Scriintec 901 RTV 1k, Scrint, Germany), protecting the super glue against organic solvents.

Measurements were performed with an uncoated but laminated AAO substrate as reference, with a laminated as well as garnet-type thin film coated AAO without sealing

between the lamination foil and the membrane, and finally with a garnet-type thin film coated AAO with sealing applied between the lamination foil and the AAO.

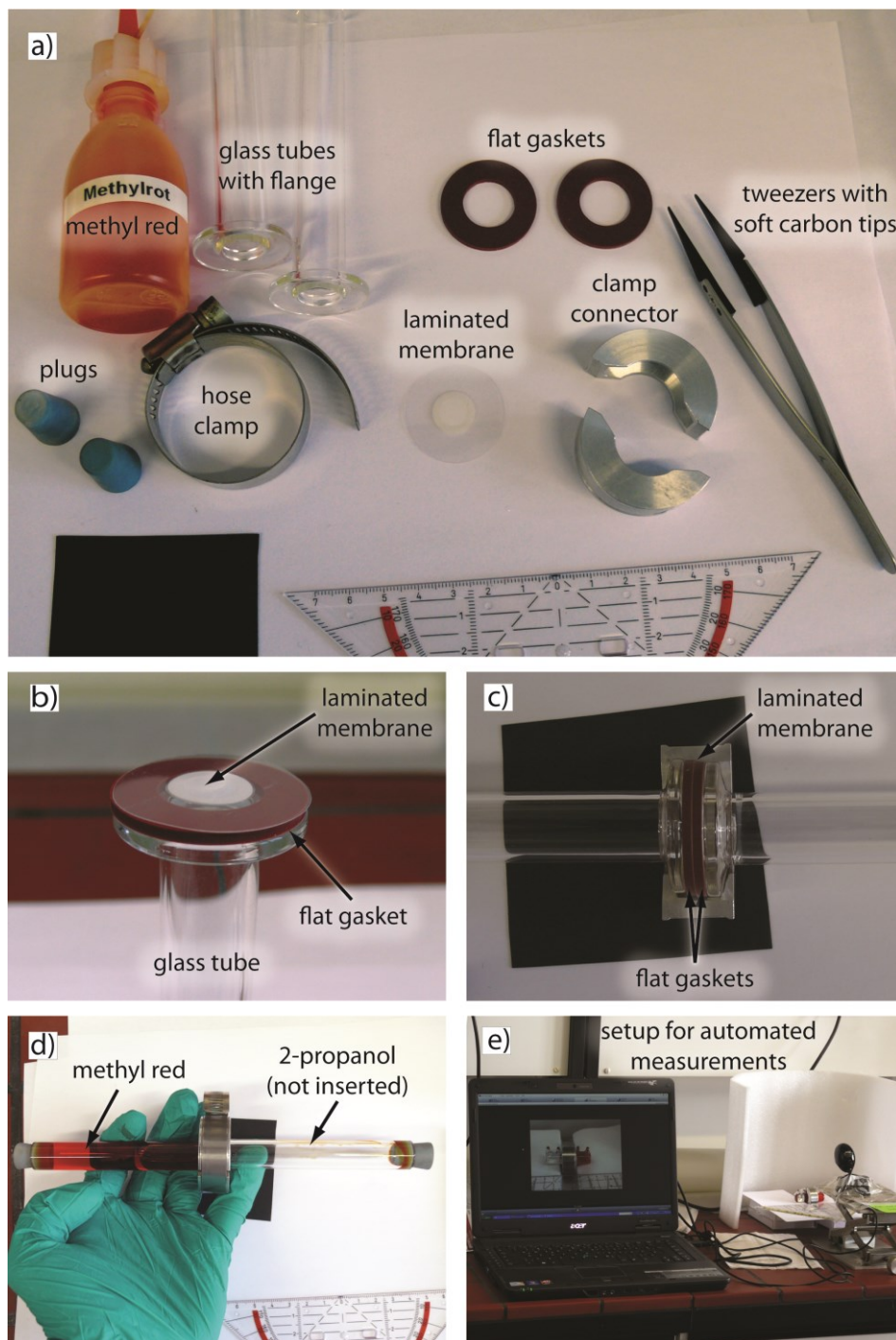


Figure 14: Setup for testing the permeation through the laminated ion-selective membranes. a) Equipment for permeation test; b) and c) membrane was embedded between two flat gaskets; d) glass tubes were squeezed together and methyl red was inserted in the left glass tube; e) automated measurement setup.

After permeation testing, the $\text{Li}_6\text{BaLa}_2\text{Ta}_2\text{O}_{12}$ coated anodized AAO were applied in Li-S cells at the “Battery and Electrochemistry Laboratory” (BELLA) at the KIT.

For the preparation of the cathodes, sulfur (Aldrich, reagent grade) and conductive carbon additives (Printex XE2, Orion and Super C65, TIMCAL™, Switzerland) were mixed in a ratio of 1:1 and ground in a ball mill. Poly(vinyl alcohol) (Selvol 425, Sekisui, Japan) dissolved in a mixed solvent of water and 2-propanol was subsequently added to the blend. The resulting mixture was ball milled for 20 h to form a homogeneous slurry. The slurry was then coated onto $\sim 8 \mu\text{m}$ thick primed aluminum (containing 2/3 Super C65 - 20 μm) with a doctor blade. The electrode was dried in vacuum at 40 °C for 16 h.

The electrolyte was a solution of 12 wt% lithium bis(trifluoromethanesulfonyl)imide (LiTFSI) (99.95 %, Aldrich), 44 wt% of 1,2-dimethoxyethane (DME) (Alfa Aesar, 99 +%) and 44 wt% 1,3-dioxolane (DOL) (99.8 %, Acros, Belgium). The electrolyte solvents were purified by distillation from sodium potassium alloy under argon atmosphere.

For the cell assembly, coin-type cells were built in an argon-filled glovebox using a sulfur cathode with an electrode diameter of 8 mm. The small electrode diameter was chosen to avoid contact with $\text{Li}_6\text{BaLa}_2\text{Ta}_2\text{O}_{12}$ -uncoated areas. The ion-selective membrane was used to separate the negative lithium electrode (lithium foil, 600 μm thick, China Lithium Ltd., China) from the positive sulfur electrode. Additionally, a glass fiber separator (Whatman, 8 mm in diameter, GE Healthcare Life Sciences, USA) was placed between the negative electrode and the ion-selective membrane. The garnet coating faced towards the lithium electrode. The sulfur electrode was assembled on the opposite side of the lithium ion conductive thin film and was placed directly onto the porous membrane. The glass fiber separator as well as the positive electrode was soaked with liquid electrolyte. The setup of the assembled cell is shown in Figure 15.

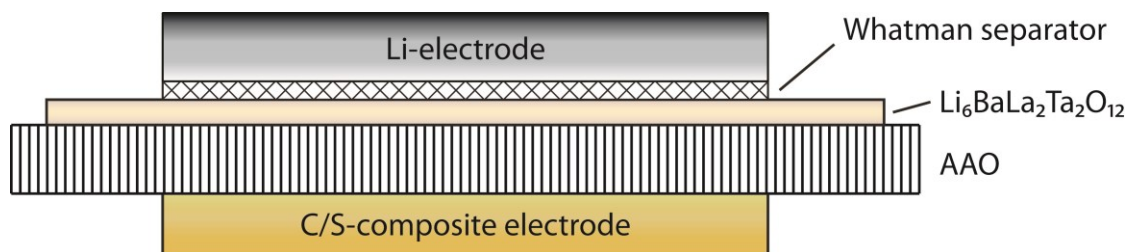


Figure 15: Setup for the Li-S cell with ion-selective membrane.

Discharge-charge cycling of the cell was performed at 36 μA (corresponds to a rate of C/50 for the sulfur electrode used) for the first cycle with a discharge cutoff voltage of 1.7 V and charge cutoff at 2.5 V. For the subsequent cycles a discharge current of 360 μA , and charge current of 220 μA were applied. This corresponds to a discharge rate of C/5 and a charge rate of C/8 for the Li-S cell.

Furthermore, a reference Li-S cell without $\text{Li}_6\text{BaLa}_2\text{Ta}_2\text{O}_{12}$ -coated AAO was built and cycled corresponding to the Li-S cell with $\text{Li}_6\text{BaLa}_2\text{Ta}_2\text{O}_{12}$ -coated AAO.

5. Results and Discussion

5.1 Characterization of garnet-type bulk material

5.1.1 X-ray diffraction

Phase determination of the PLD targets was carried out by XRD. For this purpose, a bit of each garnet-type material was grinded and examined. Figure 16 shows the diffraction patterns of the different garnet-type materials. $\text{Li}_5\text{La}_3\text{Nb}_2\text{O}_{12}$ (ICSD-PDF: 00-045-0109 [115]) was used as reference pattern (black lines) at the bottom. It has to be remembered that the reference does only indicate the 2θ position of a reflex, and does not give information about the reflex intensity, as the metal ions differ. The reflex positions of the garnet are also shown by gray columns in the background. Going from bottom to top the following garnet-type phases are shown: $\text{Li}_6\text{BaLa}_2\text{Ta}_2\text{O}_{12}$, $\text{Li}_{6.5}\text{La}_3\text{Zr}_{1.5}\text{Ta}_{0.5}\text{O}_{12}:\text{Al}_2\text{O}_3$, $\text{Li}_{6.5}\text{La}_3\text{Zr}_{1.5}\text{Ta}_{0.5}\text{O}_{12}$, $\text{Li}_6\text{La}_3\text{Zr}_1\text{Ta}_1\text{O}_{12}$ and $\text{Li}_{5.5}\text{La}_3\text{Zr}_{0.5}\text{Ta}_{1.5}\text{O}_{12}$. The abscissa shows 2θ in ° (degrees) and the ordinate shows the intensity in arbitrary, linear units. The XRD of $\text{Li}_7\text{La}_3\text{Zr}_2\text{O}_{12}$ stabilized by Ga_2O_3 is not shown here because this target material has been synthesized by Dr. Hany El Shinawi and the results have been published elsewhere [41].

The garnet-type phases show a cubic structure with $\text{Ia}\bar{3}\text{d}$ symmetry. $\text{Li}_6\text{BaLa}_2\text{Ta}_2\text{O}_{12}$ shows the biggest unit cell of all investigated garnet-type target materials with a lattice parameter of 12.989 Å. For comparison, the indicated $\text{Li}_5\text{La}_3\text{Nb}_2\text{O}_{12}$ reference has a lattice parameter of 12.889 Å, i.e., 0.76 % smaller. This is mainly caused by the incorporation of Ba^{2+} on La^{3+} sites (24c). Ba^{2+} has a bigger ionic radius of 149 pm [104] compared to 117 pm [104] of La^{3+} . Along with the Ba^{2+} incorporation goes a Li^+ incorporation for charge neutrality ($\text{Ba}^{2+} + \text{Li}^+ = \text{La}^{3+}$).

$\text{Li}_{6.5}\text{La}_3\text{Zr}_{1.5}\text{Ta}_{0.5}\text{O}_{12}$ stabilized additionally by Al_2O_3 and $\text{Li}_{6.5}\text{La}_3\text{Zr}_{1.5}\text{Ta}_{0.5}\text{O}_{12}$ showed lattice parameters (12.983 Å and 12.930 Å) comparable to that of $\text{Li}_6\text{BaLa}_2\text{Ta}_2\text{O}_{12}$. The lattice parameters were determined by Rietveld refinement using X'Pert HighScore Plus. The incorporation of Al^{3+} in the garnet-type $\text{Li}_{6.5}\text{La}_3\text{Zr}_{1.5}\text{Ta}_{0.5}\text{O}_{12}:\text{Al}_2\text{O}_3$ structure led to a decrease of the lattice parameter compared to $\text{Li}_{6.5}\text{La}_3\text{Zr}_{1.5}\text{Ta}_{0.5}\text{O}_{12}$ (without additional Al_2O_3 stabilization). Hence, the aluminum is, up to a certain extent, part of the garnet-

type structure and occupies a regular lattice site. It can be seen that with increasing tantalum content the lattice parameter decreased to 12.893 Å for $\text{Li}_6\text{La}_3\text{Zr}_1\text{Ta}_1\text{O}_{12}$ and to 12.846 Å for $\text{Li}_{5.5}\text{La}_3\text{Zr}_{0.5}\text{Ta}_{1.5}\text{O}_{12}$.

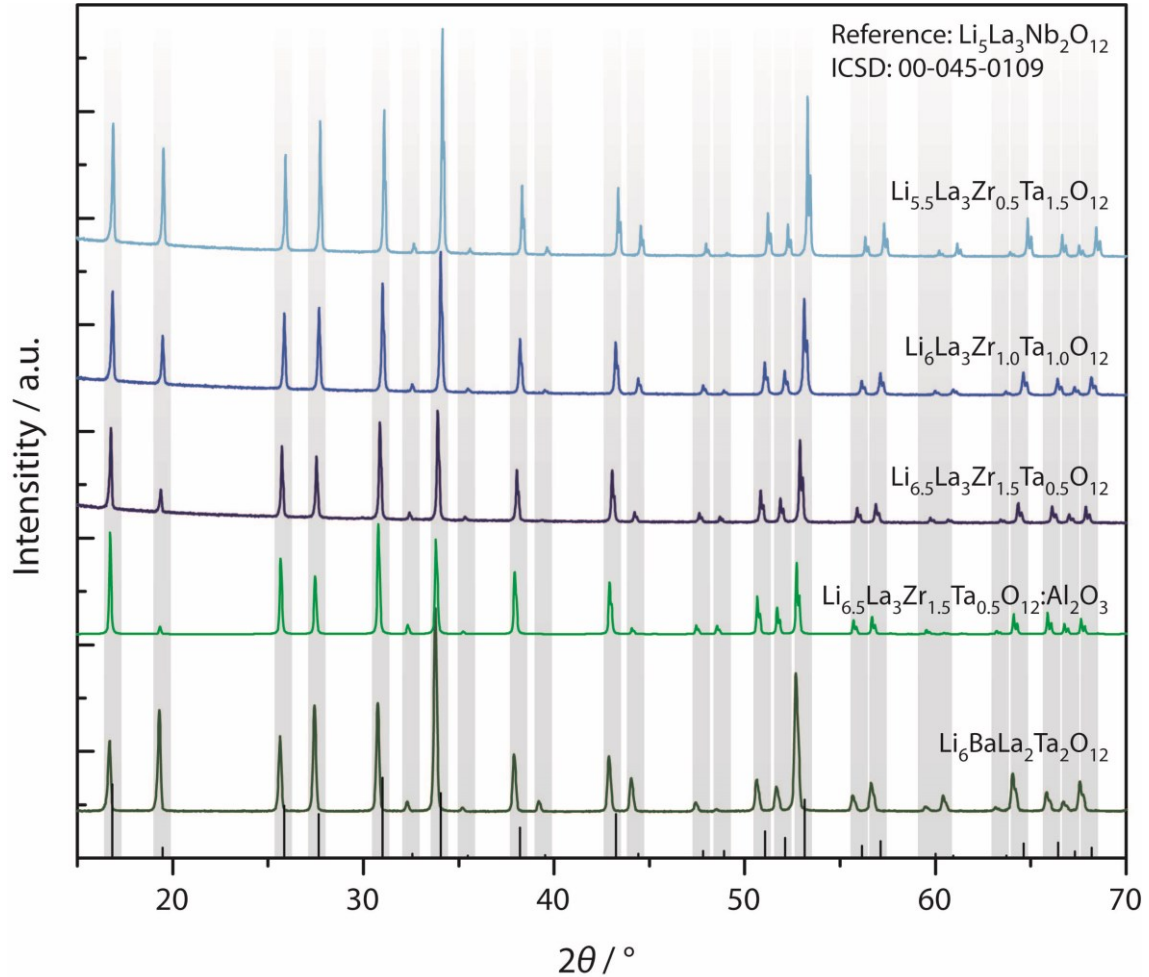


Figure 16: X-ray diffraction patterns of the different garnet-type target materials. As a reference $\text{Li}_5\text{La}_3\text{Nb}_2\text{O}_{12}$ ICSD-PDF: 00-045-0109 [115] with a lattice constant of 12.889 Å is shown as vertical, black lines.

The lattice parameter of $\text{Li}_6\text{La}_3\text{Zr}_1\text{Ta}_1\text{O}_{12}$ is between the lattice parameters of $\text{Li}_{6.5}\text{La}_3\text{Zr}_{1.5}\text{Ta}_{0.5}\text{O}_{12}$ and $\text{Li}_{5.5}\text{La}_3\text{Zr}_{0.5}\text{Ta}_{1.5}\text{O}_{12}$. This is due to the fact that Zr^{4+} (86 pm [40], coordination number = 6) has a bigger diameter than Ta^{5+} (78 pm [104], coordination number = 6). The difference in ionic radii also explains the decreasing lattice parameter with increasing Ta^{5+} content. Additionally, the substitution of Zr^{4+} with Ta^{5+} led to a

decreased Li^+ content, which should also have an influence on the lattice parameter. This finding is in accordance with literature [39, 48, 116] and can be shown by plotting the lattice parameter as a function of the constituent element, as shown in Figure 17. For comparison the values by Logéat et al. [48] are shown along with the extrapolated value for $\text{Li}_5\text{La}_3\text{Ta}_2\text{O}_{12}$.

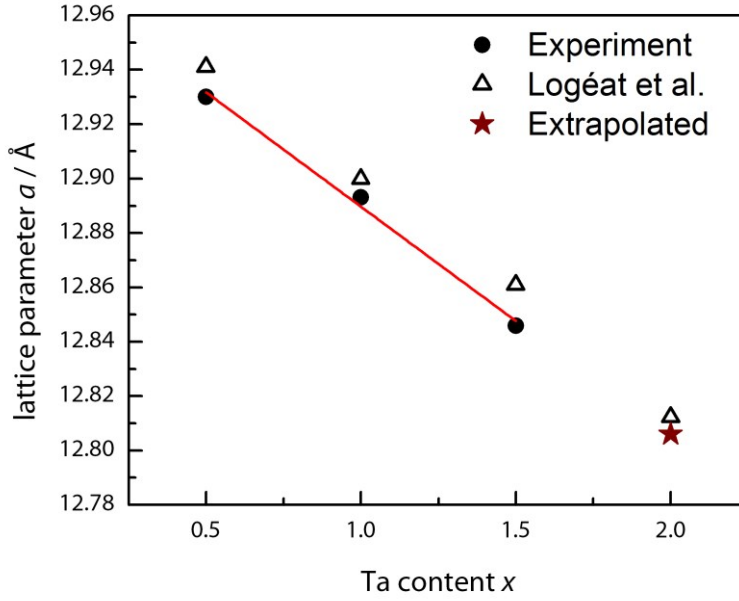


Figure 17: Lattice parameters of $\text{Li}_{7-x}\text{La}_3\text{Zr}_{2-x}\text{Ta}_x\text{O}_{12}$ as a function of tantalum content x . The solid line represents a linear fit of the lattice parameters.

The calculated lattice parameters are in good agreement to the lattice parameters obtained by Logéat et al. [48]. In general, the lattice parameter is decreasing linearly as a function of Ta^{5+} substitution. This linear correlation between the lattice parameter of an alloy as a function of a constituent element concentration at constant temperature is called Vegard's law [117] after Leon Vegard. This empirical rule can be adopted for garnet-type $\text{Li}_{7-x}\text{La}_3\text{Zr}_{2-x}\text{Ta}_x\text{O}_{12}$ structures (Eq. 5.1).

$$a_{\text{Li}_{7-x}\text{La}_3\text{Zr}_{2-x}\text{Ta}_x\text{O}_{12}} = a_{\text{Li}_7\text{La}_3\text{Zr}_2\text{O}_{12}} \left(\frac{2 - x_{\text{Ta}}}{2} \right) + a_{\text{Li}_5\text{La}_3\text{Ta}_2\text{O}_{12}} \frac{x_{\text{Ta}}}{2} \quad (5.1)$$

a is the respective lattice constant of the garnet-type material and x represents the tantalum content. The limits of the $\text{Li}_{7-x}\text{La}_3\text{Zr}_{2-x}\text{Ta}_x\text{O}_{12}$ lattice constant are the lattice constant of $\text{Li}_5\text{La}_3\text{Ta}_2\text{O}_{12}$ at the lower end and of $\text{Li}_7\text{La}_3\text{Zr}_2\text{O}_{12}$ at the upper end. It should be noted that at room temperature tetragonal $\text{Li}_7\text{La}_3\text{Zr}_2\text{O}_{12}$ is obtained instead of the cubic phase if the material is not stabilized. However, the intercept obtained from the plot of the lattice parameter versus the tantalum concentration (Figure 17) makes the determination of the lattice parameter of $\text{Li}_7\text{La}_3\text{Zr}_2\text{O}_{12}$ possible. Thus, the lattice parameter of cubic $\text{Li}_7\text{La}_3\text{Zr}_2\text{O}_{12}$ at room temperature would be $12.974 \text{ \AA} \pm 0.006 \text{ \AA}$ (the error of the lattice parameter was derived by propagation of uncertainty). A comparison to literature values is not possible as cubic $\text{Li}_7\text{La}_3\text{Zr}_2\text{O}_{12}$ (without stabilization) is, at room temperature, a hypothetical structure. Furthermore, the lattice parameter of $\text{Li}_5\text{La}_3\text{Ta}_2\text{O}_{12}$, $a = 12.806 \text{ \AA} \pm 0.017 \text{ \AA}/x$, was obtained by extrapolation to a tantalum content of $x = 2$ (slope = $-0.084 \text{ \AA}/x \pm 0.006 \text{ \AA}/x$). A comparison of the thus obtained lattice constant of $\text{Li}_5\text{La}_3\text{Ta}_2\text{O}_{12}$ to literature [115] values ($a = 12.823 \text{ \AA}$) is in good agreement.

5.1.2 Conductivity measurements

The conductivity of garnet-type $\text{Li}_6\text{BaLa}_2\text{Ta}_2\text{O}_{12}$ bulk samples was measured by electrochemical impedance spectroscopy (cf. chapter 4.2.2). The impedance of a $\text{Li}_6\text{BaLa}_2\text{Ta}_2\text{O}_{12}$ sample with lithium electrodes ($\text{Li}|\text{Li}_6\text{BaLa}_2\text{Ta}_2\text{O}_{12}|\text{Li}$) at room temperature is shown in Figure 18. The respective Nyquist plot is displayed in Figure 18 a). The black dots represent the measured data; the red solid line represents the fit. The sample exhibits two semicircles. The semicircle at high frequencies can be attributed to the bulk and grain boundary contributions. These bulk and grain contributions cannot be separated, due to their similar time constants. Therefore, this first semicircle is fitted by a single resistance (R_1) parallel to a constant phase element (Q_1). The second semicircle at lower frequencies is caused by the charge transfer resistance at the electrode and the electrode capacity. This finding shows that the metallic lithium electrode is (inhibited) reversible. With regard to a non-ideal electrode capacity, most likely caused by rough interfaces between the garnet-type pellet and the metallic lithium electrodes, a constant phase element parallel to a resistance was used to describe the electrode contribution. The resulting equivalent circuit used for the fit of the impedance data consists of two parallel (RQ)-elements in series, as shown in the upper right corner of

Figure 18 a). The vertices of the two semicircles are at 766 kHz ($\text{Li}_6\text{BaLa}_2\text{Ta}_2\text{O}_{12}$) and 4.4 kHz (Li-electrodes) and are indicated in the Nyquist plot. The Bode plot of the sample is shown in Figure 18 b).

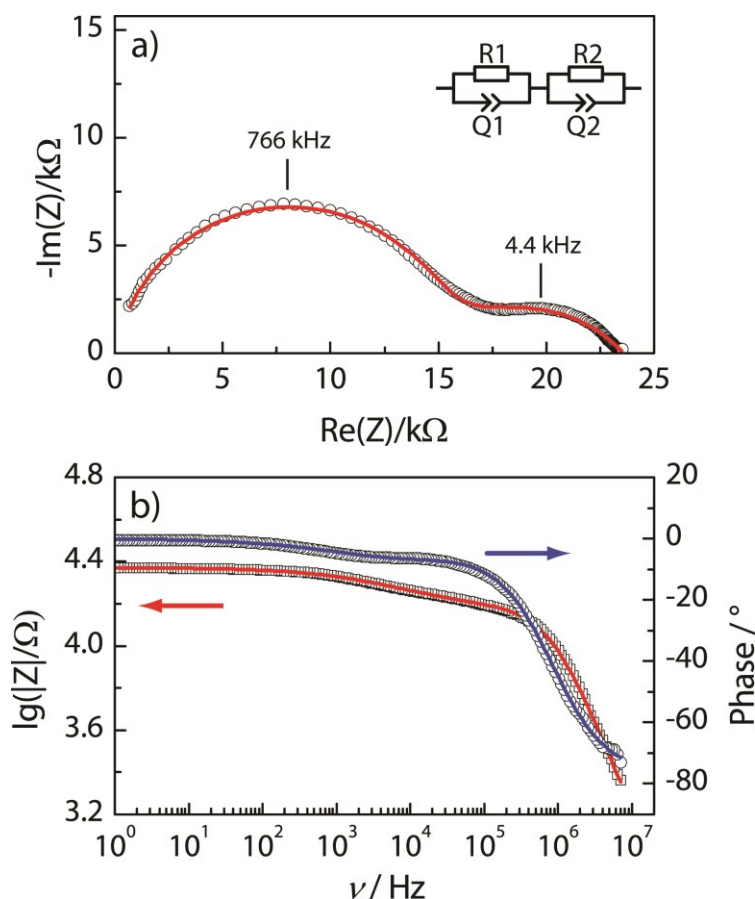


Figure 18: Electrochemical impedance measurement of a $\text{Li}_6\text{BaLa}_2\text{Ta}_2\text{O}_{12}$ garnet-type ceramic sample at 25 °C. a) Impedance response of the sample depicted as a Nyquist plot. The measured data is represented by open circles, the fitted data as a red solid line. Two frequencies are displayed at the vertices of the semicircles. Additionally, the equivalent circuit used for the fit is displayed. b) Impedance data of the sample depicted as Bode plot. The open circles represent the measured phase. The fit of the phase is displayed as a blue, solid line. The modulus of the impedance is displayed as open squares, the fit as a red, solid line.

The open circles are the measured data points for the phase; the fit of the phase is displayed as a blue, solid line. The open squares are the measured data points for the

modulus of the impedance; the fit is displayed as a red, solid line. The Bode plot is displayed in the frequency regime of 7 MHz - 1 Hz. The two semicircles from the Nyquist plot can be seen in the Bode plot as two plateaus. The resistance of the sample ($R_l = 15.112 \text{ k}\Omega$) was obtained from the resistance of the first (R_1Q_1)-element ($Q_1 = 5.6 \cdot 10^{-11} \text{ Fs}^{(a-1)}$, exponent $a_1 = 0.90$, $R_2 = 8.700 \text{ k}\Omega$, $Q_2 = 4.46 \cdot 10^{-7} \text{ Fs}^{(a-1)}$, exponent $a_2 = 0.53$). The resulting conductivity of the sample at 25 °C was calculated to be $\sigma = 5.8 \cdot 10^{-5} \text{ S}\cdot\text{cm}^{-1}$. The constant phase element of the second semicircle (Q_2 , a_2) corresponds to a Warburg impedance which indicates that a semi-infinite diffusion occurs at the electrode.

Temperature dependent measurements of the impedance, in the temperature range from $-40 \text{ }^\circ\text{C}$ to $80 \text{ }^\circ\text{C}$, revealed an activation energy of the charge transfer of 0.45 eV. The resulting Arrhenius plot is displayed in Figure 19. The black squares show the measured data, whereas the red, solid line represents the linear fit of the measured data points. The arrow and the dashed, grey line indicate room temperature. It can be seen that the measured data shows a linear dependence in the Arrhenius plot. Therefore, the relation displayed in Eq. 5.2 can be used to calculate the activation energy (given above, $E_a = 0.45 \text{ eV}$) of the charge transfer from the slope of the fit shown in Figure 19.

$$\ln(\sigma T) = \ln(\sigma_0) - \frac{E_a}{RT} \quad (5.2)$$

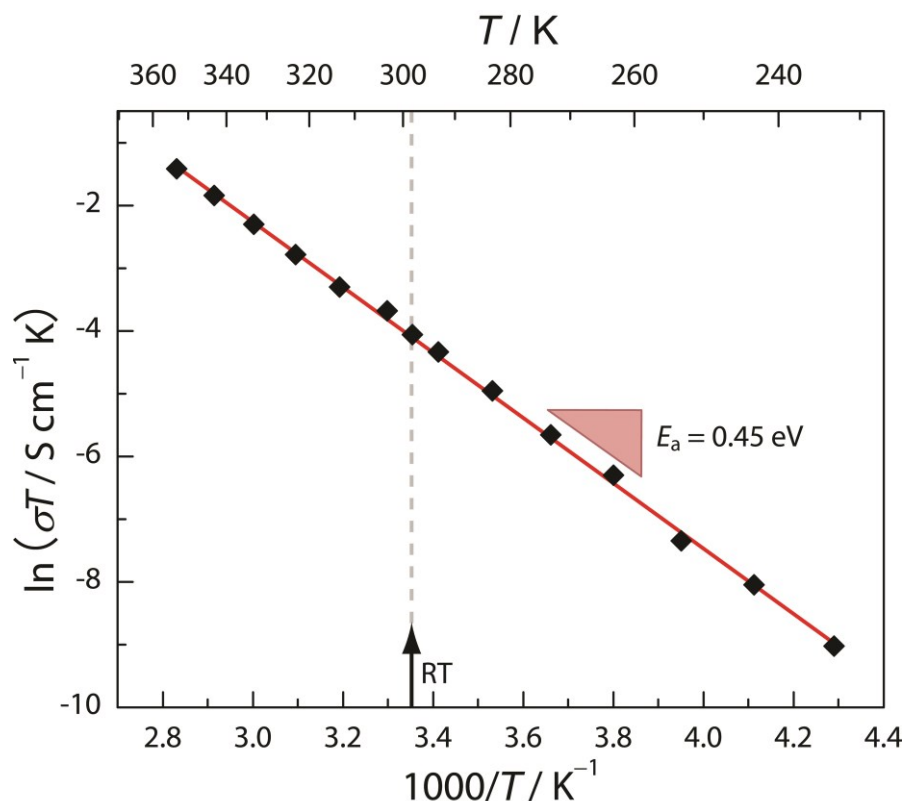


Figure 19: Arrhenius plot of the conductivity of a garnet-type polycrystalline $\text{Li}_6\text{BaLa}_2\text{Ta}_2\text{O}_{12}$ bulk sample. The black squares indicate the measured data whereas the red, solid line represents the fit. The activation energy was derived from the slope of the fit. Additionally, an arrow and a grey dotted line indicate room temperature (RT).

Hebb-Wagner polarization was performed in order to determine the partial electronic conductivity of the $\text{Li}_6\text{BaLa}_2\text{Ta}_2\text{O}_{12}$ sample. Therefore, an asymmetric cell (different electrode materials) with one reversible lithium electrode and one blocking carbon electrode ($\text{Li}|\text{Li}_6\text{BaLa}_2\text{Ta}_2\text{O}_{12}|\text{C}$) was used. The current was measured as function of time at a constant potential difference between the two electrodes. The Hebb-Wagner polarization experiment was performed in a voltage range from 2.8 V to 4.3 V. After more than 3 days a steady-state current (averaged over multiple measurement points) was obtained for every applied voltage. This steady state current was plotted as a function of the applied potential difference in Figure 20.

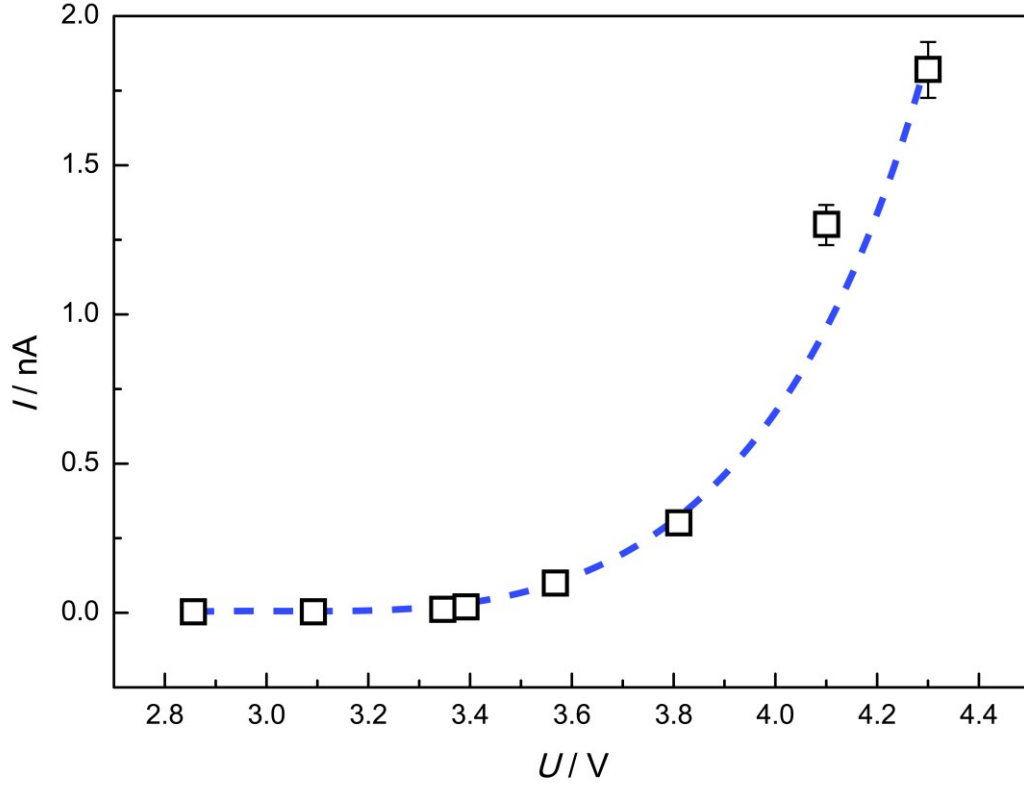


Figure 20: Hebb-Wagner polarization measurement using a $\text{Li}|\text{Li}_6\text{BaLa}_2\text{Ta}_2\text{O}_{12}|\text{C}$ cell at room temperature. The black squares show the measured data points - current as a function of voltage. The dashed blue line is only a guide to the eye and does not represent a physical model.

The total conductivity was obtained from electrochemical impedance measurements and the electronic conductivity was obtained by Hebb-Wagner polarization. The connection between the different conductivities is described in Eq. 5.3.

$$\begin{aligned}
 \sigma &= \sigma_{\text{ion}} + \sigma_{\text{el}} \\
 &= \sigma_{\text{ion}} + \sigma_{\text{e}} + \sigma_{\text{h}}
 \end{aligned}
 \tag{5.3}$$

σ represents the total conductivity, σ_{el} and σ_{ion} denote the partial electronic and ionic conductivity, respectively. The electronic conductivity itself can be separated into the contributions from electrons (σ_{e}) and electron holes (σ_{h}).

The transference numbers of electrons/electron holes and lithium ions were calculated using the total and partial electronic conductivity as defined in Eq. 5.4 and Eq. 5.5.

$$t_{\text{el}} = \frac{\sigma_{\text{el}}}{\sigma} \quad (5.4)$$

$$t_{\text{Li}^+} = 1 - t_{\text{el}} \quad (5.5)$$

t_{el} is the electronic transference number, and t_{Li^+} is the transference number of the lithium ions.

The resulting electronic conductivity is in the range from $\sigma_{\text{el}} = 3.1 \cdot 10^{-13} \text{ S} \cdot \text{cm}^{-1}$ to $\sigma_{\text{el}} = 3.7 \cdot 10^{-10} \text{ S} \cdot \text{cm}^{-1}$ in the voltage range from $U = 2.8 \text{ V}$ to $U = 4.3 \text{ V}$. Consequently, the electronic transference number ranges from $t_{\text{el}} = 5.3 \cdot 10^{-9}$ to $t_{\text{el}} = 6.4 \cdot 10^{-6}$, which is consistent with lithium ion transference numbers of $t_{\text{Li}} = 0.999999995$ to $t_{\text{Li}} = 0.999994$, respectively.

It can be assumed that anodic polarization leads to an oxidation of $\text{Li}_6\text{BaLa}_2\text{Ta}_2\text{O}_{12}$. Thereby, electron holes are introduced into the garnet-type material along with the formation of lithium vacancies according to the defect equation (Eq. 5.6) in Kröger-Vink notation.



The deposition of metallic lithium causes the formation of lithium ion vacancies (V_{Li}') and electron holes (h^{\bullet}) for charge compensation inside the garnet-type material. The lithium ion on a regular garnet-type lattice site is denoted as $\text{Li}_{\text{Li}}^{\times}$. Assuming that Eq. 5.6 can be strictly applied, one comes to the conclusion that the electron hole conductivity (σ_{h}) is direct proportional to the lithium metal deficiency (V_{Li}') and to the electron hole concentration (c_{h}) when considering constant charge (z_{h}) and constant mobility of the electron holes (μ_{h}), as displayed in Eq. 5.7.

$$\sigma_{\text{h}} = c_{\text{h}} z_{\text{h}} \mu_{\text{h}} \quad (5.7)$$

Table 6 summarizes the collected electrochemical data of a garnet-type $\text{Li}_6\text{BaLa}_2\text{Ta}_2\text{O}_{12}$ ceramic sample. Listed are the cell constant (l/A), the total conductivity (σ), the activation energy of the charge transfer (E_a) and the electronic conductivity (σ_{el}) of the sample.

Table 6: Summarized electrochemical data of a ceramic $\text{Li}_6\text{BaLa}_2\text{Ta}_2\text{O}_{12}$ garnet-type sample. The conductivities refer to a temperature of 25 °C.

	Cell constant / cm^{-1}	$\sigma / \text{S}\cdot\text{cm}^{-1}$	E_a / eV	$\sigma_{\text{el}} / \text{S}\cdot\text{cm}^{-1}$
$\text{Li}_6\text{BaLa}_2\text{Ta}_2\text{O}_{12}$	0.877	$5.8\cdot 10^{-5}$	0.45	$10^{-13} - 10^{-10}$

The results obtained are consistent with literature where the conductivity of $\text{Li}_6\text{BaLa}_2\text{Ta}_2\text{O}_{12}$ is given with $\sigma = 4\cdot 10^{-5} \text{ S}\cdot\text{cm}^{-1}$ (measured at 22 °C) [44] and an activation energy between 0.40 eV [44] and 0.44 eV [105]. The obtained electronic conductivity is very small leading to a transference number for the lithium ions of approximately 1, which is favorable for a solid state electrolyte.

5.2 Characterization of garnet-type thin films

5.2.1 X-ray diffraction

All deposited garnet-type thin films were characterized by means of x-ray diffraction. The diffractograms of the following garnet-type thin films are shown in Figure 21.

- 1) $(\text{Li}_{6.5}\text{La}_3\text{Zr}_{1.5}\text{Ta}_{0.5}\text{O}_{12}:\text{Al}_2\text{O}_3|\text{Li}_7\text{La}_3\text{Zr}_2\text{O}_{12}:\text{Ga}_2\text{O}_3)\times 5$
- 2) $(\text{Li}_6\text{BaLa}_2\text{Ta}_2\text{O}_{12}|\text{Li}_{6.5}\text{La}_3\text{Zr}_{1.5}\text{Ta}_{0.5}\text{O}_{12}:\text{Al}_2\text{O}_3)\times 5$
- 3) $\text{Li}_{5.5}\text{La}_3\text{Zr}_{0.5}\text{Ta}_{1.5}\text{O}_{12}$
- 4) $\text{Li}_6\text{La}_3\text{Zr}_1\text{Ta}_1\text{O}_{12}$
- 5) $\text{Li}_{6.5}\text{La}_3\text{Zr}_{1.5}\text{Ta}_{0.5}\text{O}_{12}$
- 6) $\text{Li}_{6.5}\text{La}_3\text{Zr}_{1.5}\text{Ta}_{0.5}\text{O}_{12}$ stabilized by Al_2O_3
- 7) $\text{Li}_7\text{La}_3\text{Zr}_2\text{O}_{12}$ stabilized by Ga_2O_3
- 8) $\text{Li}_6\text{BaLa}_2\text{Ta}_2\text{O}_{12}$

$\text{Li}_5\text{La}_3\text{Nb}_2\text{O}_{12}$ is indicated as a reference (ICSD-PDF: 00-045-0109 [115]) by black lines at the bottom of Figure 21. Some diffraction patterns show broad reflexes between 20° and 25° and a single reflex at about 38.8° . These reflexes are caused by the $\text{MgO}(100)$ substrate if it is not entirely (100)-oriented. These substrate reflexes are not always present as they depend on the individual $\text{MgO}(100)$ substrate quality (orientation).

Nevertheless, it can be seen from Figure 21 that the deposition of garnet-type thin films was successfully achieved for each kind of garnet-type source material. However, only $\text{Li}_6\text{BaLa}_2\text{Ta}_2\text{O}_{12}$, $\text{Li}_7\text{La}_3\text{Zr}_2\text{O}_{12}:\text{Ga}_2\text{O}_3$ and $\text{Li}_{6.5}\text{La}_3\text{Zr}_{1.5}\text{Ta}_{0.5}:\text{Al}_2\text{O}_3$ have been deposited phase pure. The multilayer thin films show broadened reflexes due to the slightly different lattice constants of the garnet-type materials used.

The $\text{Li}_{7-x}\text{La}_3\text{Zr}_{2-x}\text{Ta}_x\text{O}_{12}$ series shows phase impurities with increasing zirconium content. A tantalum content of $x = 0.5$ or 1.0 of the target material seems to be insufficient to entirely stabilize the garnet-type thin film phase at the chosen deposition parameters. In addition to the garnet-type phase, these thin films show phases of the corresponding metal oxides and of the mixed metal oxides. These observations show that high quality garnet-type thin films can be deposited more easily by PLD if a higher degree of stabilization is

ensured. The stabilization can either be realized by a high tantalum content of the garnet-type phase or by addition of Ga_2O_3 or Al_2O_3 .

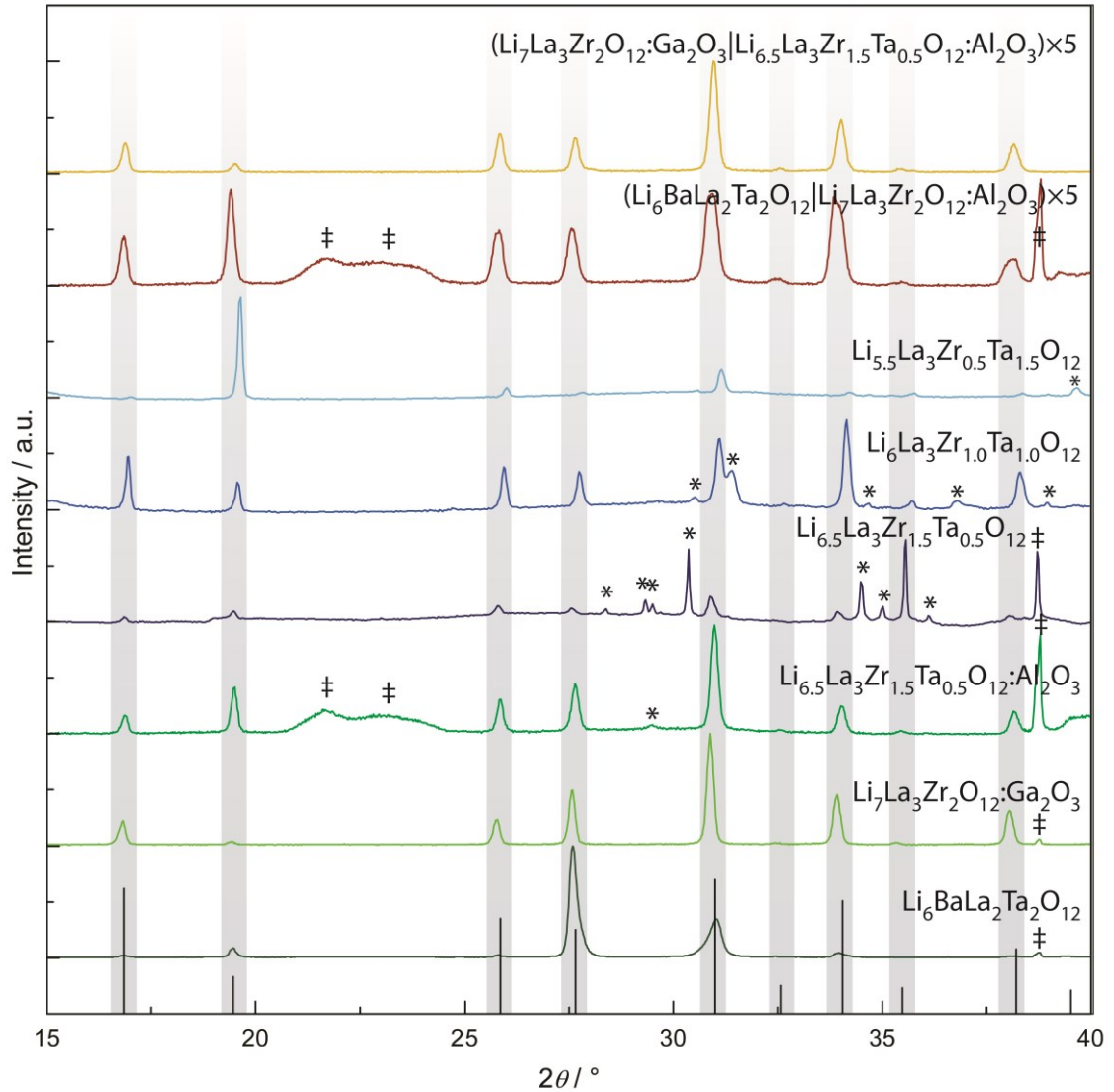


Figure 21: X-ray diffractograms of different garnet-type thin films prepared by pulsed laser deposition on $\text{MgO}(100)$. The displayed diagram shows (from bottom to top): $\text{Li}_5\text{La}_3\text{Nb}_2\text{O}_{12}[115]$ as reference (vertical, black lines), $\text{Li}_6\text{BaLa}_2\text{Ta}_2\text{O}_{12}$ (dark green), $\text{Li}_7\text{La}_3\text{Zr}_2\text{O}_{12}:\text{Ga}_2\text{O}_3$ (light green), $\text{Li}_{6.5}\text{La}_3\text{Zr}_{1.5}\text{Ta}_{0.5}:\text{Al}_2\text{O}_3$ (green), $\text{Li}_{6.5}\text{La}_3\text{Zr}_{1.5}\text{Ta}_{0.5}\text{O}_{12}$ (dark blue), $\text{Li}_6\text{La}_3\text{Zr}_1\text{Ta}_1\text{O}_{12}$ (blue), $\text{Li}_{5.5}\text{La}_3\text{Zr}_{0.5}\text{Ta}_{1.5}\text{O}_{12}$ (light blue) and the multilayer thin films with 5 bilayers consisting of: $(\text{Li}_6\text{BaLa}_2\text{Ta}_2\text{O}_{12}|\text{Li}_7\text{La}_3\text{Zr}_2\text{O}_{12}:\text{Ga}_2\text{O}_3)\times 5$ (red) and $(\text{Li}_{6.5}\text{La}_3\text{Zr}_{1.5}\text{Ta}_{0.5}:\text{Al}_2\text{O}_3|\text{Li}_7\text{La}_3\text{Zr}_2\text{O}_{12}:\text{Ga}_2\text{O}_3)\times 5$ (yellow). The asterisk (*) marks phase impurities, the double dagger (‡) shows MgO substrate reflexes.

The electrochemical characterization of the garnet-type thin films was solely performed on single- and multilayer thin films consisting of phase-pure garnet-type thin films ($\text{Li}_6\text{BaLa}_2\text{Ta}_2\text{O}_{12}$, $\text{Li}_7\text{La}_3\text{Zr}_2\text{O}_{12}:\text{Ga}_2\text{O}_3$ and $\text{Li}_{6.5}\text{La}_3\text{Zr}_{1.5}\text{Ta}_{0.5}:\text{Al}_2\text{O}_3$) to ensure that no impurity phase affects the measured data.

In the case of $\text{Li}_6\text{BaLa}_2\text{Ta}_2\text{O}_{12}$ the garnet-type thin film was directly deposited onto a $\text{MgO}(100)$ substrate. In the case of the remaining garnet-type phases the thin films were deposited onto a $\text{MgO}(100)$ substrate that was coated with a thin layer (< 100 nm) of $\text{Li}_6\text{BaLa}_2\text{Ta}_2\text{O}_{12}$.

5.2.2 Scanning electron microscopy

Scanning electron microscopy images revealed that not every substrate is suitable for the deposition of garnet-type thin films. Due to the elevated temperatures during the ablation process thermal strain is induced by the substrate in the thin film when it is cooled to room temperature. If the substrate is not well-matched, the mechanical strain is relieved by crack formation within the thin film. This crack formation is distinct if the garnet-type thin film is applied on top of a silicon substrate as can be seen from Figure 22 a) (secondary electron detector - SE2). The formation of cracks in the garnet-type thin film on top of a platinum coated MgO(100) is moderate, whereas on uncoated MgO(100) substrates generally no cracking occurs. Figure 22 b) shows a cracked garnet-type thin film on top of a platinum coated MgO(100) substrate (Inlens detector - Inlens). A $\text{Li}_{6.5}\text{La}_3\text{Zr}_{1.5}\text{Ta}_{0.5}\text{O}_{12}:\text{Al}_2\text{O}_3$ garnet-type thin film is shown in cross section on a $\text{Li}_6\text{BaLa}_2\text{Ta}_2\text{O}_{12}$ coated MgO(100) substrate in Figure 22 c) (Inlens). On top of the garnet-type film residues from a previously applied metallic lithium electrode from conductivity measurements can be seen. Figure 22 d) shows a cross section of a garnet-type multilayer structure with a total of ten alternating layers. The structure was composed of $\text{Li}_6\text{BaLa}_2\text{Ta}_2\text{O}_{12}$ and $\text{Li}_{6.5}\text{La}_3\text{Zr}_{1.5}\text{Ta}_{0.5}\text{O}_{12}:\text{Al}_2\text{O}_3$. Starting at the bottom with $\text{Li}_6\text{BaLa}_2\text{Ta}_2\text{O}_{12}$ which appears slightly brighter than $\text{Li}_{6.5}\text{La}_3\text{Zr}_{1.5}\text{Ta}_{0.5}\text{O}_{12}:\text{Al}_2\text{O}_3$ in the scanning electron microscope using an energy selected backscatter detector (ESB) which was chosen in order to achieve a material contrast. At the left side of the picture added horizontal lines indicate the layered structure of the material.

In conclusion, the results show that conductivity measurements in axial geometry are challenging due to the formation of cracks which inevitably lead to short circuits. Conductivity measurements in lateral geometry could be accomplished more easily as no crack formation was observed when the garnet-type thin film was deposited directly onto a MgO(100) substrate.

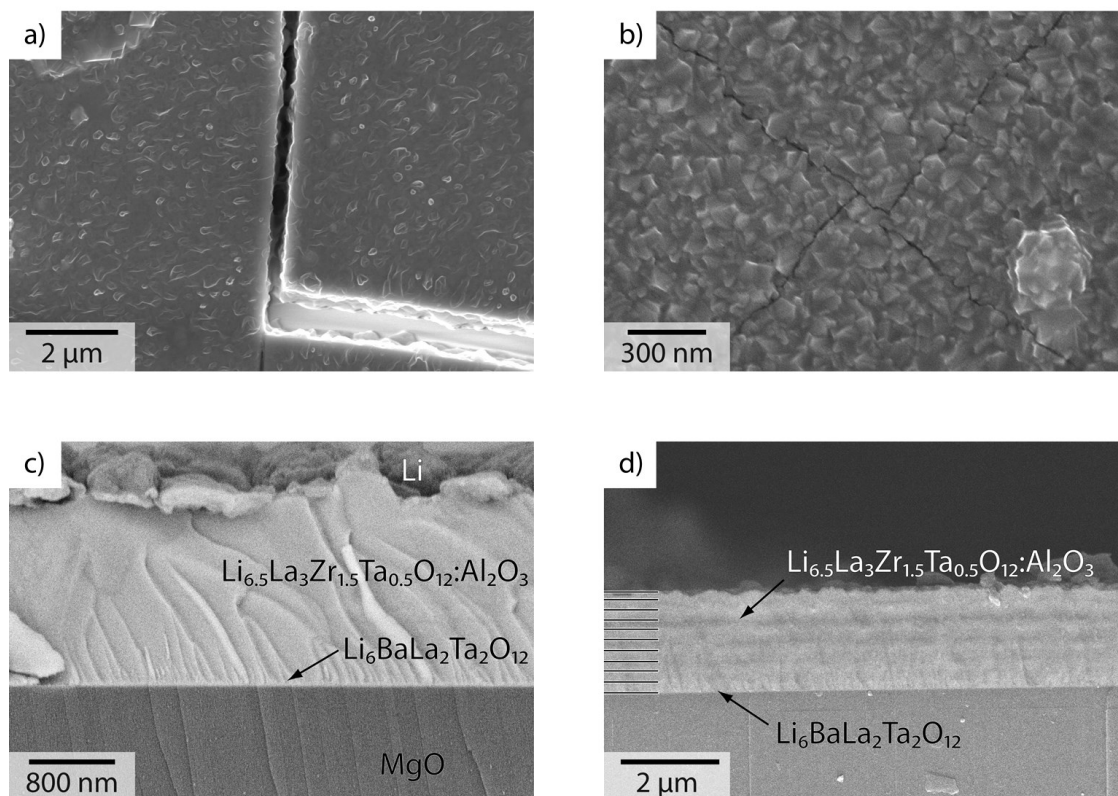


Figure 22: Scanning electron microscopy images of different garnet-type thin films. a) Top view of a $\text{Li}_6\text{BaLa}_2\text{Ta}_2\text{O}_{12}$ thin film on top of a Si substrate. b) Top view of a $\text{Li}_6\text{BaLa}_2\text{Ta}_2\text{O}_{12}$ thin film on top of a platinum coated $\text{MgO}(100)$ substrate. c) Cross section of a $\text{Li}_{6.5}\text{La}_3\text{Zr}_{1.5}\text{Ta}_{0.5}\text{O}_{12}:\text{Al}_2\text{O}_3$ garnet-type thin film on a $\text{Li}_6\text{BaLa}_2\text{Ta}_2\text{O}_{12}$ coated $\text{MgO}(100)$ substrate. Residue of a previously applied metallic lithium electrode can be seen on top of the $\text{Li}_{6.5}\text{La}_3\text{Zr}_{1.5}\text{Ta}_{0.5}\text{O}_{12}:\text{Al}_2\text{O}_3$ film. d) Cross section of a garnet-type multilayer structure with five bilayers – $(\text{Li}_6\text{BaLa}_2\text{Ta}_2\text{O}_{12}|\text{Li}_{6.5}\text{La}_3\text{Zr}_{1.5}\text{Ta}_{0.5}\text{O}_{12}:\text{Al}_2\text{O}_3)\times 5$.

In addition to “post mortem” scanning electron microscopy measurements dc polarization measurements were performed in situ in a high resolution scanning electron microscope (HRSEM) using a platinum microelectrode and a broad metallic lithium electrode. The measurement setup can be seen in Figure 11 of chapter 4.3.1. The platinum electrode was polarized negatively versus the lithium electrode. The current density was estimated to be about $j = 30 \text{ mA}\cdot\text{cm}^{-2}$ from the approximate contact area of the microelectrode at the beginning of the experiment. The current density decreased during the experiment with the amount of deposited lithium as the electrode area was increased by the metal

deposition. It can be seen from Figure 23 that metallic lithium is deposited on top of the garnet-type solid electrode by reduction of lithium ions at the phase boundary between the metal electrode supplying the electrons and the solid electrolyte providing the lithium ions. There are two different growth modes observed simultaneously during this experiment: a two dimensional lateral growth on top of the solid electrolyte and whisker growth. The in situ visualization of the lithium deposition as a function of time can be seen on the right hand side of Figure 23. The process that is represented in this image sequence took 50 minutes. This experiment clearly demonstrates that the $\text{Li}_6\text{BaLa}_2\text{Ta}_2\text{O}_{12}$ garnet-type thin film is a lithium ion conductor. However, a quantification of the conductivity was not possible from this experiment as the geometry of the measurement setup, especially the electrode area, could not be determined exactly and was changing during the lithium deposition.

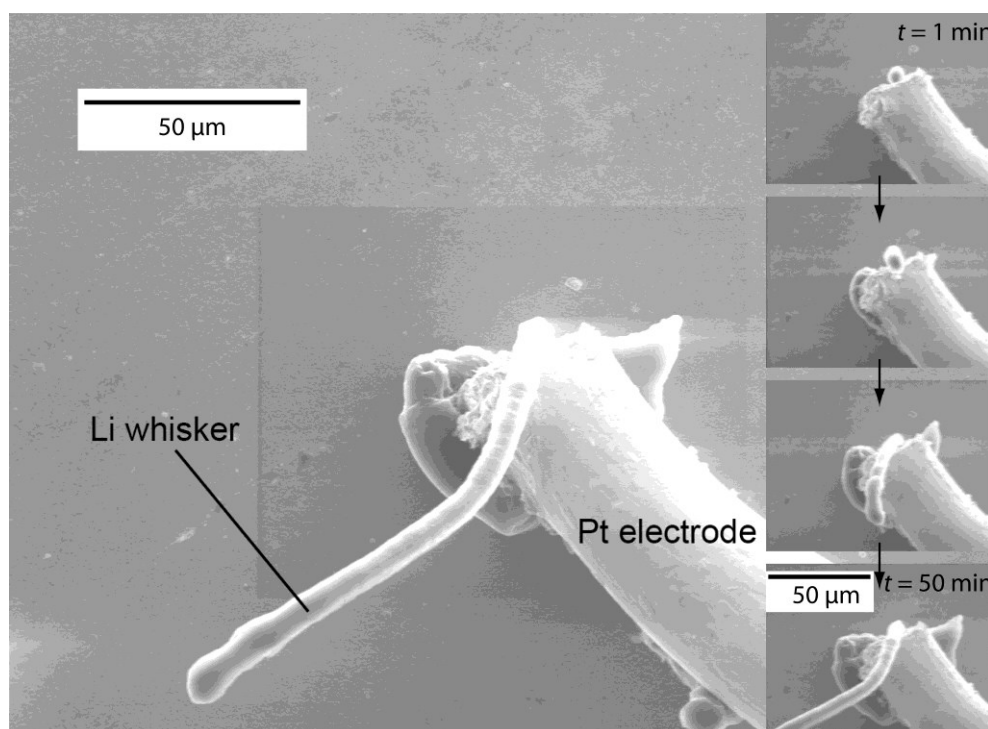


Figure 23: In situ visualization of lithium deposition by dc polarization of a $\text{Li}_6\text{BaLa}_2\text{Ta}_2\text{O}_{12}$ garnet-type thin film using a microelectrode inside a scanning electron microscope. The large picture shows the experiment after 50 min. The image sequence on the right hand side depicts the deposition process of lithium over that time range.

Further, scanning electron microscopy investigations were performed on garnet-type thin film coated anodized aluminum oxide. Figure 24 a) shows a tilted cross section of an uncoated anodized aluminum oxide substrate (SE2). The homogenously ordered two-dimensional pores have a diameter of about 100 nm and are aligned in z -direction. At the beginning of the deposition of garnet-type thin films on top of the porous substrate islands of the respective material start to grow on the pore walls, which leads to a Stranski-Krastanov (island-plus-layer) type growth of the thin film forced by the substrate material. Sufficient material deposition results in an impermeable, pore blocking thin film. Such a well prepared garnet-type thin film can be seen as a cross section in Figure 24 b) (SE2). At the bottom of the thin film a columnar structure can be observed, as the deposited garnet-type material was not able to form a closed layer directly from the start. With increasing film thickness the islands grew into each other. This means that a coating which is only a few nanometers thick would not be able to form a pore-blocking film.

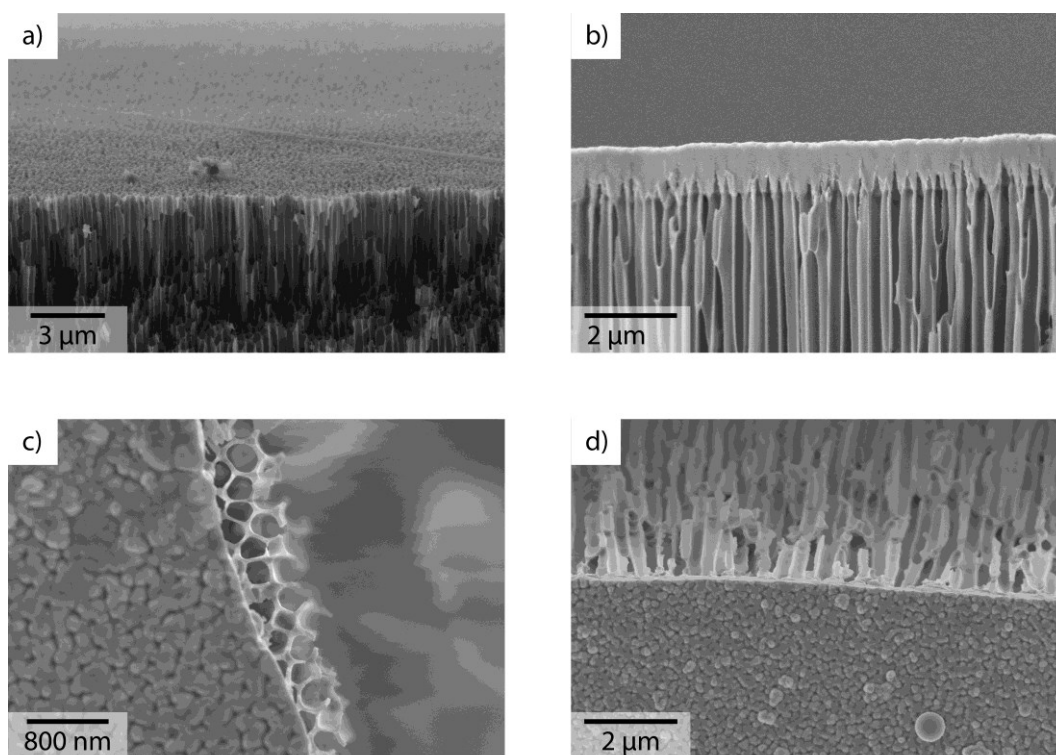


Figure 24: Scanning electron microscopy images of: a) tilted cross section of an uncoated porous AAO substrate; b) Li₆BaLa₂Ta₂O₁₂ garnet-type thin film on top of an AAO substrate in cross section; c) top view of a partially coated AAO substrate; d) tilted cross section of a Li₆BaLa₂Ta₂O₁₂ coated AAO substrate.

Figure 24 c) shows the edge between a coated and an uncoated area of a membrane revealing that the pores of the substrate are covered by the deposited material. However, the top of the garnet-type thin film still shows inhomogeneities resulting from the Stranski-Krastanov-like growth mechanism as can be seen in the tilted cross section of a coated anodized aluminum oxide substrate in Figure 24 d).

5.2.3 Transmission electron microscopy

Transmission electron microscopy studies were performed of garnet-type multilayer thin films with the intention to understand the cause of the increased conductivity of multilayer structures compared to single layer thin films. Transmission electron microscopy images of $(\text{Li}_6\text{BaLa}_2\text{Ta}_2\text{O}_{12}|\text{Li}_{6.5}\text{La}_3\text{Zr}_{1.5}\text{Ta}_{0.5}\text{O}_{12}:\text{Al}_2\text{O}_3)\times 10$ multilayer thin films can be seen in Figure 25. Figure 25 a) gives an overview of the lamella prepared by focused ion beam (FIB). The $\text{Li}_6\text{BaLa}_2\text{Ta}_2\text{O}_{12}$ garnet-type thin film appears dark in the bright field mode and white in the dark field mode, vice versa for the $\text{Li}_{6.5}\text{La}_3\text{Zr}_{1.5}\text{Ta}_{0.5}\text{O}_{12}:\text{Al}_2\text{O}_3$ garnet-type thin film. The $\text{MgO}(100)$ substrate can be seen as a bright area at the bottom and the platinum coating can be seen at the top of the image. Between the $\text{MgO}(100)$ substrate and the platinum coating at the top, 20 alternating layers of the two garnet-type materials can be seen. The multilayer thin film starts with $\text{Li}_6\text{BaLa}_2\text{Ta}_2\text{O}_{12}$ at the bottom. The waviness of the layers increases with increasing layer number. This has mainly two reasons. First, each imperfection adds up to all the layers deposited afterwards, increasing the roughness of the thin film; second the FIB cut is not entirely smooth. This causes a change of thickness of the thin film in viewing direction, which leads to cone-like structures and waviness depending on the film morphology in viewing direction. A detailed picture of the interface between the $\text{MgO}(100)$ substrate and the garnet-type multilayer thin film can be seen in Figure 25 b). The image shows that a smooth interface between the substrate and the first garnet-type layer is formed. Furthermore, the two different garnet-type materials form a smooth interface free from macroscopic defects. It can be seen that especially the $\text{Li}_6\text{BaLa}_2\text{Ta}_2\text{O}_{12}$ garnet-type layers show a columnar growth. A cone caused by the FIB preparation of the lamella can be seen in the left part of the picture. Figure 25 c) shows an enlarged image of the interface quality between a $\text{Li}_6\text{BaLa}_2\text{Ta}_2\text{O}_{12}$ garnet-type layer embedded between two $\text{Li}_{6.5}\text{La}_3\text{Zr}_{1.5}\text{Ta}_{0.5}\text{O}_{12}:\text{Al}_2\text{O}_3$ garnet-type thin film layers. The interface shows that almost

no mixing of the two different garnet-type phases occurs. High resolution images as well as EDX measurements were not possible due to the poor electron beam stability of the garnet-type material in the TEM. Figure 25 d) shows an overview of the sample after the TEM measurements. Material decomposition was observed during the experiments, which led to “shrinkage” of the multilayer thin film and the formation of voids coupled with lithium precipitation. Because of this, the defect structure at the interface between the two garnet-type phases could not be investigated further.

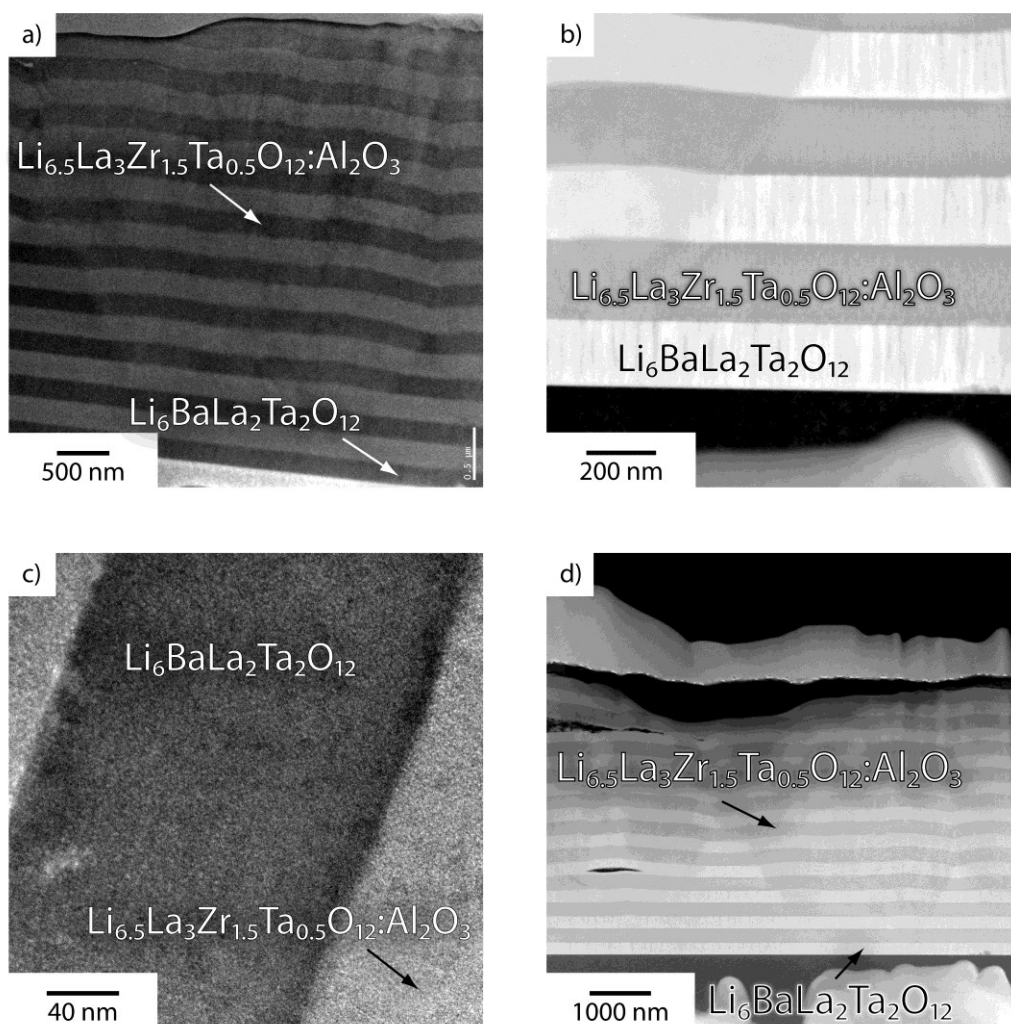


Figure 25: Transmission electron microscopy images of a garnet-type ($\text{Li}_6\text{BaLa}_2\text{Ta}_2\text{O}_{12}|\text{Li}_{6.5}\text{La}_3\text{Zr}_{1.5}\text{Ta}_{0.5}\text{O}_{12}:\text{Al}_2\text{O}_3$) $\times 10$ multilayer thin film. a) Bright field overview of the 10 garnet-type bilayers, beginning with $\text{Li}_6\text{BaLa}_2\text{Ta}_2\text{O}_{12}$ (dark) at the bottom. b) Enlarged dark field image of the alternating garnet-type layers. c) Bright field detail image of a $\text{Li}_6\text{BaLa}_2\text{Ta}_2\text{O}_{12}$ to $\text{Li}_{6.5}\text{La}_3\text{Zr}_{1.5}\text{Ta}_{0.5}\text{O}_{12}:\text{Al}_2\text{O}_3$ interface. d) Electron beam induced damage of the garnet-type thin film in dark field mode.

Besides the garnet-type multilayer thin film a prototype thin film cell consisting of $\text{Si}|\text{Li}_6\text{BaLa}_2\text{Ta}_2\text{O}_{12}|\text{LiFePO}_4|\text{Pt}|\text{Cu}$ was investigated using TEM. This cell did not show a cell voltage, and the TEM measurements were conducted to investigate possible causes. Most likely a short circuit due to contact of both electrode materials caused the breakdown of the cell voltage. Figure 26 shows the appropriate cross section of the layered cell system. The single layers are $\text{Li}_6\text{BaLa}_2\text{Ta}_2\text{O}_{12}$ (LBLTO), LiFePO_4 (LFP), platinum and copper. It can be seen that the different thin film materials were deposited onto each other without observable cracks in the small image section. However, the measured region shows a droplet of the $\text{Li}_6\text{BaLa}_2\text{Ta}_2\text{O}_{12}$ garnet-type material that is embedded between the interface of the garnet-type layer to the LiFePO_4 layer. The difference in shading of the droplet is probably caused by the different deposition methods of the materials. The darker part of the droplet is the actual target material droplet, the lighter colored material is subsequently deposited by the PLD process as thin film. A gap between the droplet and the garnet-type thin film is filled up with LiFePO_4 (bright) that was deposited after the garnet-type material. The area marked in Figure 26 a) is magnified in b). The magnified image clearly shows the deposited LiFePO_4 material in the gap between the garnet-type material (dark) and the droplet. The garnet-type thin film and droplet do not grow together since the temperature for a solid state reaction is too low. This leads to the formation of a gap between the regular thin film and the droplet. Thereby, LiFePO_4 was deposited into the gap.

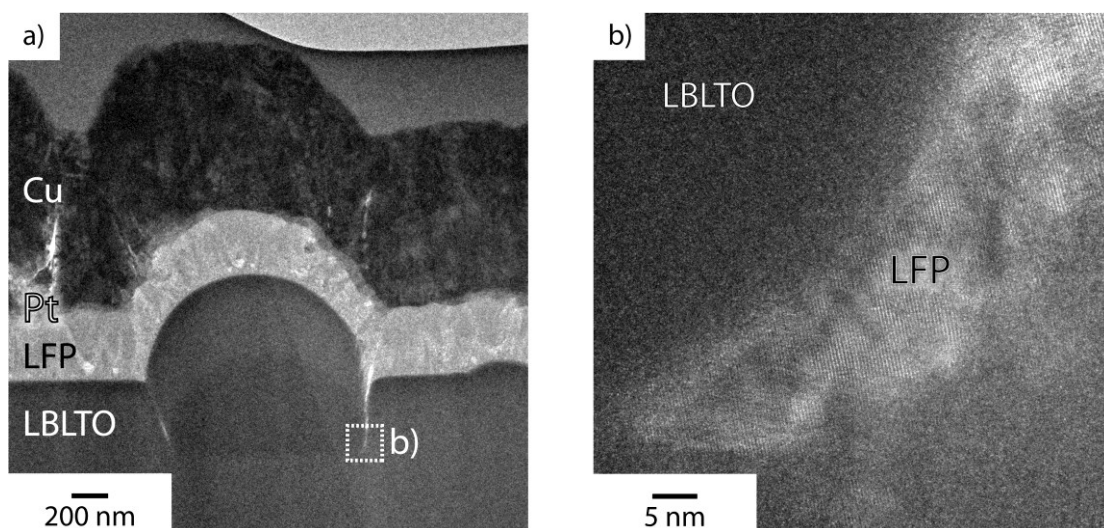


Figure 26: Transmission electron microscopy images of a prototype thin film cell consisting of $\text{Li}_6\text{BaLa}_2\text{Ta}_2\text{O}_{12}|\text{LiFePO}_4|\text{Pt}|\text{Cu}$ on a silicon substrate. a) Cross section of the layered all solid state cell. b) Magnification of the area marked in the overview.

This phenomenon is not a single event, as the TEM images show only a small segment of the prepared all-solid-state cell and formation of droplets cannot be prevented during the PLD process. This leads to the assumption that a short circuit was the cause of the lacking cell voltage.

5.2.4 Conductivity measurements in lateral geometry

The conductivities of garnet-type thin film samples were determined by electrochemical impedance spectroscopy in lateral geometry and are discussed exemplarily for a $\text{Li}_6\text{BaLa}_2\text{Ta}_2\text{O}_{12}$ garnet-type thin film.

An electrochemical impedance spectroscopy measurement of a $\text{Li}_6\text{BaLa}_2\text{Ta}_2\text{O}_{12}$ garnet-type thin film at room temperature is shown in Figure 27. Only one semicircle was observed (for the Nyquist plot) in the frequency region from 1 MHz to 1 Hz for the $\text{Li}_6\text{BaLa}_2\text{Ta}_2\text{O}_{12}$ thin film. The thin film was prepared by pulsed laser deposition on a MgO(100) substrate and gold electrodes were applied. The blocking gold electrodes could only be observed at elevated temperatures or at frequencies below 100 mHz. A deconvolution of the impedance data into the grain boundary and bulk contributions was not possible, independent of the temperature. This was found as the usual behavior for lithium ion conducting garnet-type materials (bulk), because the impedance of the grain boundary and the bulk have the same time constant ($\tau = RC$). In the case of conductivity measurements in lateral geometry another effect is crucial: The capacity of the substrate is identical (determined in a separate measurement) to the capacity determined for a thin film sample by impedance spectroscopy. Hence, the substrate capacity, which is parallel to the thin film, dominates due to geometrical reasons. However, the resistance of the substrate is higher than the resistance of the thin film yielding a semicircle consisting of two resistances (grain boundary and bulk are in series and can thereby be expressed as one resistance) parallel to the substrate capacity. Thus, only one semicircle can be observed. Subsequently, the equivalent model for the fit consisted of a resistance parallel to a constant phase element - (RQ). The constant phase element was chosen because of the slightly oblate semicircle. Figure 27 a) shows the Nyquist plot of the electrochemical impedance spectroscopy measurement. The measured data is represented by open circles. The equivalent circuit fit is shown as a red, solid line. Figure 27 b) shows the respective

Bode plot. The logarithmic modulus of the impedance is shown as open squares; the phase is shown as open circles. The equivalent circuit fit is depicted as a red, solid line and as a blue, solid line for the logarithmic modulus of the impedance and the phase, respectively. The resistance of the $\text{Li}_6\text{BaLa}_2\text{Ta}_2\text{O}_{12}$ garnet-type thin film with gold electrodes was determined from the equivalent circuit fit to be $R = 2.9 \cdot 10^7 \Omega$ ($Q = 1.1 \cdot 10^{-11} \text{ Fs}^{(a-1)}$, exponent $a = 0.99$). The film thickness was $2 \mu\text{m}$. The gold electrodes were 1 cm long and 1 mm apart. The resulting cell constant was $l/A = 500 \text{ cm}^{-1}$. Hence, the conductivity of the $\text{Li}_6\text{BaLa}_2\text{Ta}_2\text{O}_{12}$ garnet-type thin film is evaluated as $\sigma = 1.7 \cdot 10^{-6} \text{ S} \cdot \text{cm}^{-1}$.

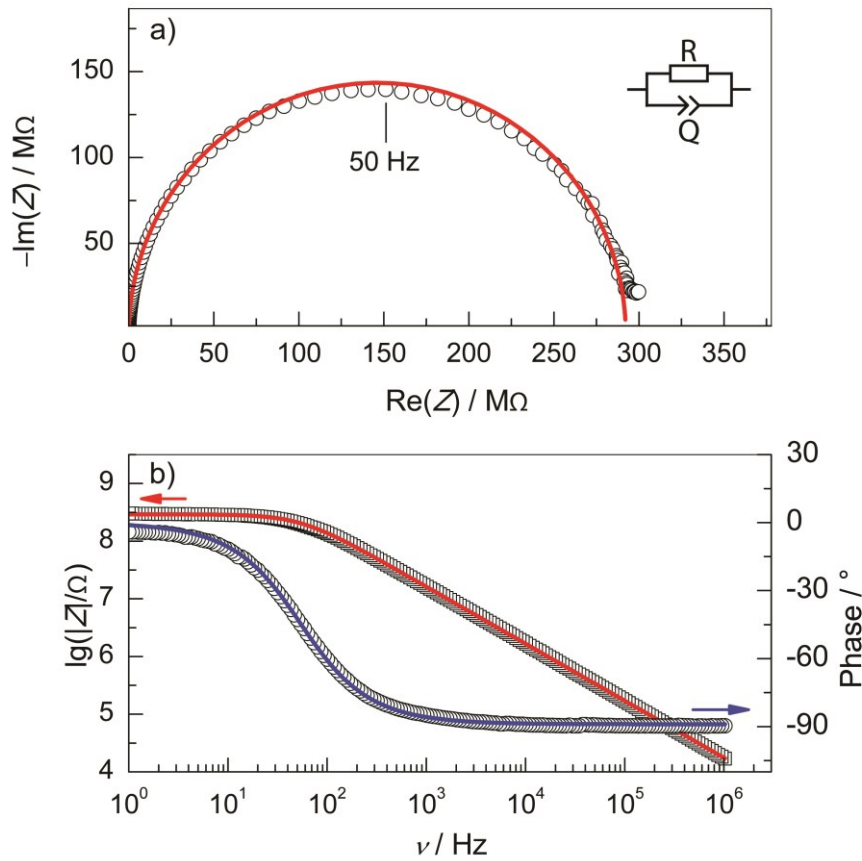


Figure 27: Impedance spectra of a $\text{Li}_6\text{BaLa}_2\text{Ta}_2\text{O}_{12}$ garnet-type thin film prepared by PLD on a $\text{MgO}(100)$ substrate. The measurement was performed at 25°C . Measured data are shown as open circles and open squares. The equivalent circuit fit is depicted as solid line. a) Nyquist plot of the sample, the apex is indicated. b) Respective Bode plot of the sample.

Additionally, the conductivity of the garnet-type thin film was verified by a 2-point dc polarization measurement using reversible lithium electrodes in lateral geometry on a 2 μm thick $\text{Li}_6\text{BaLa}_2\text{Ta}_2\text{O}_{12}$ garnet-type thin film. The measurement was performed at room temperature in a range of -1 V to 1 V . The measurement is depicted in Figure 28. The measured data shows a linear (ohmic) behavior of the current as a function of the applied potential (U has been plotted as a function of I in order to have direct access to the resistance from the slope). The slope was determined by a linear fit and results in a resistance of $R = 310\text{ M}\Omega$. The calculated conductivity of $\sigma = 1.6 \cdot 10^{-6}\text{ S}\cdot\text{cm}^{-1}$ agrees well with the impedance measurement. The small discrepancy between the EIS and dc measurement might be caused by a small charge transfer resistance of the electrodes or by small variations of film quality in the case of the dc measurement.

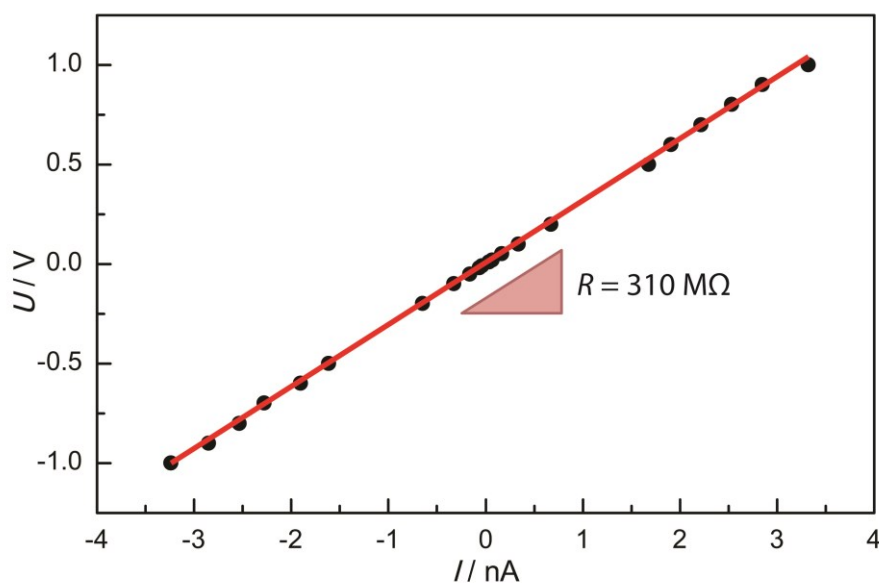


Figure 28: dc measurement of a $\text{Li}_6\text{BaLa}_2\text{Ta}_2\text{O}_{12}$ garnet-type thin film with two reversible Li-electrodes at $25\text{ }^\circ\text{C}$. The sample was measured in lateral geometry and shows ohmic behavior in the range from -1 V to 1 V .

Furthermore, $\text{Li}_{6.5}\text{La}_3\text{Zr}_{1.5}\text{Ta}_{0.5}\text{O}_{12}:\text{Al}_2\text{O}_3$ and $\text{Li}_7\text{La}_3\text{Zr}_2\text{O}_{12}:\text{Ga}_2\text{O}_3$ as well as multilayer thin films consisting of $(\text{Li}_{6.5}\text{La}_3\text{Zr}_{1.5}\text{Ta}_{0.5}:\text{Al}_2\text{O}_3|\text{Li}_7\text{La}_3\text{Zr}_2\text{O}_{12}:\text{Ga}_2\text{O}_3) \times n$ and

$(\text{Li}_6\text{BaLa}_2\text{Ta}_2\text{O}_{12}|\text{Li}_{6.5}\text{La}_3\text{Zr}_{1.5}\text{Ta}_{0.5}:\text{Al}_2\text{O}_3)\times n$ were characterized by temperature dependent electrochemical impedance spectroscopy.

The temperature dependent conductivity of the different garnet-type thin films is depicted in Figure 29 as an Arrhenius plot. The total conductivity of single layer thin films is $2.9\cdot 10^{-6} \text{ S}\cdot\text{cm}^{-1}$ for $\text{Li}_{6.5}\text{La}_3\text{Zr}_{1.5}\text{Ta}_{0.5}\text{O}_{12}:\text{Al}_2\text{O}_3$, $\sigma = 1.7\cdot 10^{-6} \text{ S}\cdot\text{cm}^{-1}$ for $\text{Li}_6\text{BaLa}_2\text{Ta}_2\text{O}_{12}$ and $\sigma = 1.2\cdot 10^{-6} \text{ S}\cdot\text{cm}^{-1}$ for $\text{Li}_7\text{La}_3\text{Zr}_2\text{O}_{12}:\text{Ga}_2\text{O}_3$. The activation energies ranged between 0.48 eV for $\text{Li}_{6.5}\text{La}_3\text{Zr}_{1.5}\text{Ta}_{0.5}\text{O}_{12}:\text{Al}_2\text{O}_3$ as well as for $\text{Li}_6\text{BaLa}_2\text{Ta}_2\text{O}_{12}$, and 0.44 eV for $\text{Li}_7\text{La}_3\text{Zr}_2\text{O}_{12}:\text{Ga}_2\text{O}_3$. A $(\text{Li}_6\text{BaLa}_2\text{Ta}_2\text{O}_{12}|\text{Li}_{6.5}\text{La}_3\text{Zr}_{1.5}\text{Ta}_{0.5}\text{O}_{12}:\text{Al}_2\text{O}_3)\times 5$ garnet-type multilayer thin film showed a conductivity of $\sigma = 8.9\cdot 10^{-6} \text{ S}\cdot\text{cm}^{-1}$ and a $(\text{Li}_{6.5}\text{La}_3\text{Zr}_{1.5}\text{Ta}_{0.5}:\text{Al}_2\text{O}_3|\text{Li}_7\text{La}_3\text{Zr}_2\text{O}_{12}:\text{Ga}_2\text{O}_3)\times 5$ multilayer thin film had a conductivity of $\sigma = 2.8\cdot 10^{-5} \text{ S}\cdot\text{cm}^{-1}$. The $(\text{Li}_{6.5}\text{La}_3\text{Zr}_{1.5}\text{Ta}_{0.5}:\text{Al}_2\text{O}_3|\text{Li}_7\text{La}_3\text{Zr}_2\text{O}_{12}:\text{Ga}_2\text{O}_3)\times 5$ multilayer thin film was prepared at a deposition temperature of 620 °C which is near the decomposition temperature (probably due to lithium loss) of the garnet-type thin films. The conductivities of the multilayer thin films were increased compared to their single layer components. The calculated activation energies of the charge transfer were 0.42 eV for $(\text{Li}_6\text{BaLa}_2\text{Ta}_2\text{O}_{12}|\text{Li}_{6.5}\text{La}_3\text{Zr}_{1.5}\text{Ta}_{0.5}\text{O}_{12}:\text{Al}_2\text{O}_3)\times 5$ and 0.39 eV for $(\text{Li}_{6.5}\text{La}_3\text{Zr}_{1.5}\text{Ta}_{0.5}:\text{Al}_2\text{O}_3|\text{Li}_7\text{La}_3\text{Zr}_2\text{O}_{12}:\text{Ga}_2\text{O}_3)\times 5$, respectively.

A comparison of the activation energies and conductivities shows that the single layer thin films have higher activation energies of charge transfer and lower conductivity compared to the multilayer garnet-type thin films.

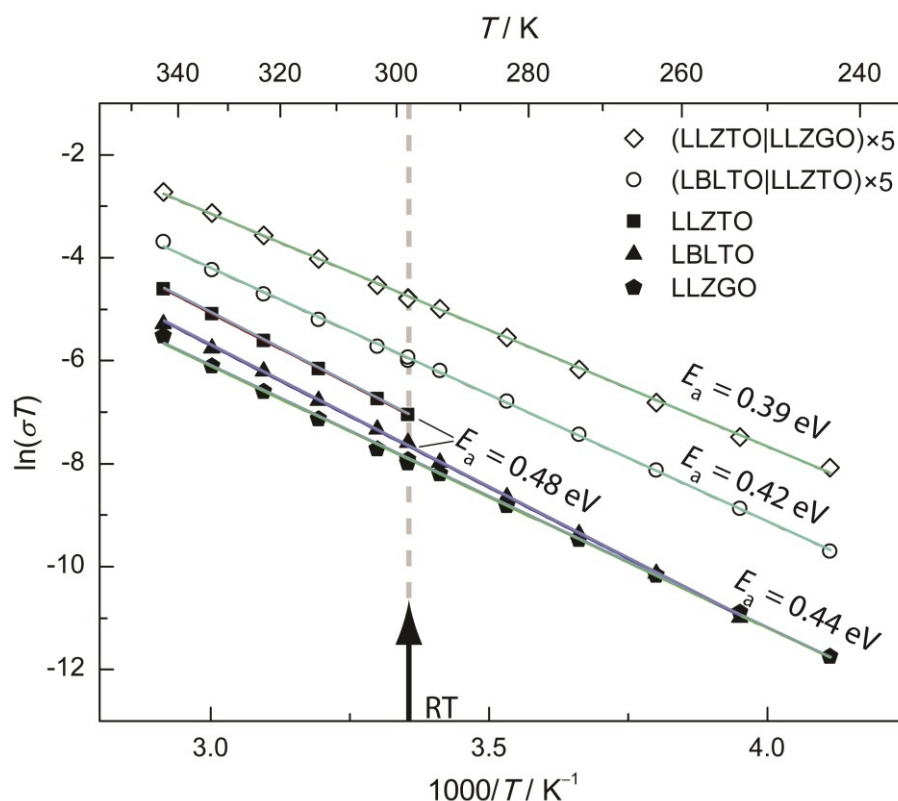


Figure 29: Total conductivity (as determined by ac impedance) of the highest conducting thin film of each kind. Depicted are from high to low conductivity (top to bottom): $(\text{Li}_{6.5}\text{La}_3\text{Zr}_{1.5}\text{Ta}_{0.5}\text{O}_{12}:\text{Al}_2\text{O}_3|\text{Li}_7\text{La}_3\text{Zr}_2\text{O}_{12}:\text{Ga}_2\text{O}_3)\times 5$ (open diamonds), $(\text{Li}_6\text{BaLa}_2\text{Ta}_2\text{O}_{12}|\text{Li}_{6.5}\text{La}_3\text{Zr}_{1.5}\text{Ta}_{0.5}\text{O}_{12}:\text{Al}_2\text{O}_3)\times 5$ (open circles), $\text{Li}_{6.5}\text{La}_3\text{Zr}_{1.5}\text{Ta}_{0.5}\text{O}_{12}:\text{Al}_2\text{O}_3$ (squares), $\text{Li}_6\text{BaLa}_2\text{Ta}_2\text{O}_{12}$ (triangles) and $\text{Li}_7\text{La}_3\text{Zr}_2\text{O}_{12}:\text{Ga}_2\text{O}_3$ (pentagons).

Furthermore, the conductivity of the multilayer thin films showed a dependence on the total number of layers and on the overall thickness of the thin films (cf. Table 7). Therefore, the overall thickness of the $(\text{Li}_6\text{BaLa}_2\text{Ta}_2\text{O}_{12}|\text{Li}_{6.5}\text{La}_3\text{Zr}_{1.5}\text{Ta}_{0.5}\text{O}_{12}:\text{Al}_2\text{O}_3)\times n$ multilayers was kept approximately constant and the amount of alternating layers was varied. The determined total conductivities were: $\sigma = 7.2 \cdot 10^{-6} \text{ S}\cdot\text{cm}^{-1}$ for a total of two bilayers - $(\text{Li}_6\text{BaLa}_2\text{Ta}_2\text{O}_{12}|\text{Li}_{6.5}\text{La}_3\text{Zr}_{1.5}\text{Ta}_{0.5}\text{O}_{12}:\text{Al}_2\text{O}_3)\times 2$ ($d = 2540$ nm), $\sigma = 7.7 \cdot 10^{-6} \text{ S}\cdot\text{cm}^{-1}$ for five bilayers - $(\text{Li}_6\text{BaLa}_2\text{Ta}_2\text{O}_{12}|\text{Li}_{6.5}\text{La}_3\text{Zr}_{1.5}\text{Ta}_{0.5}\text{O}_{12}:\text{Al}_2\text{O}_3)\times 5$ ($d = 2208$ nm) and $\sigma = 4.1 \cdot 10^{-6} \text{ S}\cdot\text{cm}^{-1}$ for 10 bilayers - $(\text{Li}_6\text{BaLa}_2\text{Ta}_2\text{O}_{12}|\text{Li}_{6.5}\text{La}_3\text{Zr}_{1.5}\text{Ta}_{0.5}\text{O}_{12}:\text{Al}_2\text{O}_3)\times 10$ ($d = 2418$ nm). These garnet-type multilayer thin films were deposited at 600°C in order to avoid decomposition due to temperature fluctuation of the substrate caused by the heater. It should be noted that the conductivity of the

multilayer thin films decreased again when 10 garnet-type bilayers were prepared, although the overall thickness of these three samples was kept almost constant. This indicates that the interface density between both garnet-type materials has an influence on the conductivity. The decreased conductivity of the multilayer thin film with 10 bilayers shows that the interface, which is an introduced grain boundary, between the two different garnet-type materials is an area of increased resistance.

To further investigate the influence of the multilayer microstructure on the conductivity, two bilayers consisting of $\text{Li}_6\text{BaLa}_2\text{Ta}_2\text{O}_{12}$ and $\text{Li}_{6.5}\text{La}_3\text{Zr}_{1.5}\text{Ta}_{0.5}\text{O}_{12}:\text{Al}_2\text{O}_3$ - $(\text{Li}_6\text{BaLa}_2\text{Ta}_2\text{O}_{12}|\text{Li}_{6.5}\text{La}_3\text{Zr}_{1.5}\text{Ta}_{0.5}\text{O}_{12}:\text{Al}_2\text{O}_3)\times 2$ - were prepared on a $\text{MgO}(100)$ substrate, with the characteristic that each single layer was about 100 nm (1000 pulses) in thickness. Then, a $\text{Li}_{6.5}\text{La}_3\text{Zr}_{1.5}\text{Ta}_{0.5}\text{O}_{12}:\text{Al}_2\text{O}_3$ thin film was deposited with 30,000 pulses on top of the four previously deposited garnet-type thin films (34,000 pulses in total), so that the last deposited single $\text{Li}_{6.5}\text{La}_3\text{Zr}_{1.5}\text{Ta}_{0.5}\text{O}_{12}:\text{Al}_2\text{O}_3$ thin film should have the highest impact on the measured conductivity of the prepared structure - $(\text{Li}_6\text{BaLa}_2\text{Ta}_2\text{O}_{12}|\text{Li}_{6.5}\text{La}_3\text{Zr}_{1.5}\text{Ta}_{0.5}\text{O}_{12}:\text{Al}_2\text{O}_3)\times 2|\text{Li}_{6.5}\text{La}_3\text{Zr}_{1.5}\text{Ta}_{0.5}\text{O}_{12}:\text{Al}_2\text{O}_3$. For the $\text{Li}_{6.5}\text{La}_3\text{Zr}_{1.5}\text{Ta}_{0.5}\text{O}_{12}:\text{Al}_2\text{O}_3$ thin film ($d_{\text{LLZTO}} \sim 2342$ nm) on a $(\text{Li}_6\text{BaLa}_2\text{Ta}_2\text{O}_{12}|\text{Li}_{6.5}\text{La}_3\text{Zr}_{1.5}\text{Ta}_{0.5}\text{O}_{12}:\text{Al}_2\text{O}_3)\times 2$ substrate - $(\text{Li}_6\text{BaLa}_2\text{Ta}_2\text{O}_{12}|\text{Li}_{6.5}\text{La}_3\text{Zr}_{1.5}\text{Ta}_{0.5}\text{O}_{12}:\text{Al}_2\text{O}_3)\times 2|\text{Li}_{6.5}\text{La}_3\text{Zr}_{1.5}\text{Ta}_{0.5}\text{O}_{12}:\text{Al}_2\text{O}_3$ ($d_{\text{tot}} = 2742$ nm) - a total conductivity of $\sigma = 7.2 \cdot 10^{-6} \text{ S}\cdot\text{cm}^{-1}$ was determined. This implies the strong dependence of the conductivity on the microstructure of the thin film, whereby the microstructure of the thin film is primarily depending on the substrate material (the substrate can also be a previously deposited garnet-type thin film). This characteristic was also found by Kim et al. [56]. The two introduced bilayers serve as a buffer layer for the last deposited layer. It is thereby shown that the increase of conductivity is no direct effect of the multilayer structure since one layer solely determines the conductivity. The increased conductivity is enabled by lattice relaxation due to a lattice matched growth of the last “thick” garnet-type layer, which probably leads to a less distinctive columnar growth (cf. chapter 5.2.6).

The $(\text{Li}_{6.5}\text{La}_3\text{Zr}_{1.5}\text{Ta}_{0.5}\text{O}_{12}:\text{Al}_2\text{O}_3|\text{Li}_7\text{La}_3\text{Zr}_2\text{O}_{12}:\text{Ga}_2\text{O}_3)\times n$ thin films behaved similar to the $(\text{Li}_6\text{BaLa}_2\text{Ta}_2\text{O}_{12}|\text{Li}_{6.5}\text{La}_3\text{Zr}_{1.5}\text{Ta}_{0.5}\text{O}_{12}:\text{Al}_2\text{O}_3)\times n$ thin films. Since the $(\text{Li}_6\text{BaLa}_2\text{Ta}_2\text{O}_{12}|\text{Li}_{6.5}\text{La}_3\text{Zr}_{1.5}\text{Ta}_{0.5}\text{O}_{12}:\text{Al}_2\text{O}_3)\times 5$ multilayer thin film with five bilayers showed the highest conductivity, the number of bilayers was kept constant at five for the

following three $(\text{Li}_{6.5}\text{La}_3\text{Zr}_{1.5}\text{Ta}_{0.5}\text{O}_{12}:\text{Al}_2\text{O}_3|\text{Li}_7\text{La}_3\text{Zr}_2\text{O}_{12}:\text{Ga}_2\text{O}_3)\times 5$ thin films which were prepared with different film thicknesses. Hereby, the intention was to investigate the influence of the overall film thickness on the conductivity. The following conductivities were obtained: $\sigma = 7.3 \cdot 10^{-6} \text{ S}\cdot\text{cm}^{-1}$ ($d = 2215 \text{ nm}$), $\sigma = 6.2 \cdot 10^{-6} \text{ S}\cdot\text{cm}^{-1}$ ($d = 1612 \text{ nm}$) and $\sigma = 2.6 \cdot 10^{-6} \text{ S}\cdot\text{cm}^{-1}$ ($d = 1424 \text{ nm}$). This shows that the conductivity of the thin films decreased as a result of decreasing overall thickness and increasing interface density (grain boundaries). By increasing the deposition temperature from 600°C to 620°C a $(\text{Li}_{6.5}\text{La}_3\text{Zr}_{1.5}\text{Ta}_{0.5}\text{O}_{12}:\text{Al}_2\text{O}_3|\text{Li}_7\text{La}_3\text{Zr}_2\text{O}_{12}:\text{Ga}_2\text{O}_3)\times 5$ multilayer thin film with a conductivity of $\sigma = 2.9 \cdot 10^{-5} \text{ S}\cdot\text{cm}^{-1}$ ($d = 2742 \text{ nm}$) was obtained (it was proven by XRD that the thin film was phase-pure). This is the highest conductivity of all prepared garnet-type thin films measured in lateral geometry. The results of the conductivity measurements are summarized in Table 7. The respective acronym of each garnet-type material was used in this table: LLZGO - $\text{Li}_7\text{La}_3\text{Zr}_2\text{O}_{12}:\text{Ga}_2\text{O}_3$, LLZTO - $\text{Li}_{6.5}\text{La}_3\text{Zr}_{1.5}\text{Ta}_{0.5}\text{O}_{12}:\text{Al}_2\text{O}_3$ and LBLTO - $\text{Li}_6\text{BaLa}_2\text{Ta}_2\text{O}_{12}$.

Table 7: Summarized total conductivities of garnet-type thin films in dependence of the deposition temperature, the amount of alternating layers, overall thickness and thickness per layer.

Type of thin film	$\sigma_{ac}(298 \text{ K})$ / $\text{S}\cdot\text{cm}^{-1}$	Deposition ϑ / $^\circ\text{C}$	Overall thickness / nm	Thickness per layer / nm
LLZGO	$1.2 \cdot 10^{-6}$	600	1956	1956
LBLTO	$1.7 \cdot 10^{-6}$	550	2000	2000
LLZTO	$2.9 \cdot 10^{-6}$	600	1861	1861
(LBLTO LLZTO) $\times 2$	$7.2 \cdot 10^{-6}$	600	2540	635
(LBLTO LLZTO) $\times 5$	$7.7 \cdot 10^{-6}$	600	2208	221
(LBLTO LLZTO) $\times 10$	$4.1 \cdot 10^{-6}$	600	2418	121
(LBLTO LLZTO) $\times 2$ LLZTO	$7.2 \cdot 10^{-6}$	600	2742	$\sim 100/2342$
(LLZTO LLZGO) $\times 5$	$7.3 \cdot 10^{-6}$	600	2215	222
(LLZTO LLZGO) $\times 5$	$6.2 \cdot 10^{-6}$	600	1612	161
(LLZTO LLZGO) $\times 5$	$2.6 \cdot 10^{-6}$	600	1424	142
(LLZTO LLZGO) $\times 5$	$2.9 \cdot 10^{-5}$	620	2742	274

It was demonstrated that garnet-type $\text{Li}_7\text{La}_3\text{Zr}_2\text{O}_{12}:\text{Ga}_2\text{O}_3$, $\text{Li}_{6.5}\text{La}_3\text{Zr}_{1.5}\text{Ta}_{0.5}\text{O}_{12}:\text{Al}_2\text{O}_3$ and $\text{Li}_6\text{BaLa}_2\text{Ta}_2\text{O}_{12}$ single layer garnet-type thin films deposited via PLD have electrical conductivities comparable to “LiPON” [50, 51]. If garnet-type thin films with two

alternating garnet-type phases were prepared, an increase in conductivity and a decrease in activation energy of the conductivity were observed compared to the single layer thin films when measuring in lateral geometry. However, this increase in conductivity is actually only an approach towards bulk conductivity. This means that the conductivity of multilayer garnet-type thin films is only increased relative to the single layer thin films. The single layer thin films show a decreased conductivity relative to the bulk material. The increase in conductivity of the multilayer thin films appears to be an effect of the microstructure of the films. The microstructure effect is probably caused by a sequential increase of “substrate quality” (lattice matching) for each subsequently deposited layer due to the multilayer structure. Each layer acts as a buffer layer for the next one. Thereby, a lattice relaxation is possible and the columnar growth is less distinctive. It is assumed that this next layer has a lower density of grain boundaries (columns are wider). Impedance measurements in lateral geometry determine the contributions of the grain boundary and the bulk resistance in series due to the columnar growth of the thin film. A summed up resistance of both contributions parallel to the substrate capacity determines the impedance behavior. Furthermore, it was demonstrated that transport across grain boundaries leads to higher resistances. Therefore, a higher contribution of the bulk compared to the grain boundaries leads to a reduced overall resistance. Hence, a high density of grain boundaries/interfaces leads to a low conductivity. A decreasing density of grain boundaries results in an increase of the conductivity finally approaching the bulk ceramic conductivity.

It was observed that four alternating layers (two bilayers) provide a sufficient increase in “substrate quality” for an increase of over 100 % in conductivity compared to the respective single layer thin film. Even if the four layers were only about 400 nm thick and a fifth layer on top was about 2 μm in thickness, thereby determining the resistance of the material (83 % of the garnet-type thin film thickness is caused by the fifth layer), the same increase in conductivity was observed. The $(\text{Li}_{6.5}\text{La}_3\text{Zr}_{1.5}\text{Ta}_{0.5}\text{O}_{12}:\text{Al}_2\text{O}_3|\text{Li}_7\text{La}_3\text{Zr}_2\text{O}_{12}:\text{Ga}_2\text{O}_3)\times 5$ multilayer thin film prepared at 620 °C shows an increase in conductivity of about one order of magnitude compared to a single layer $\text{Li}_{6.5}\text{La}_3\text{Zr}_{1.5}\text{Ta}_{0.5}\text{O}_{12}:\text{Al}_2\text{O}_3$ thin film and a factor 24 compared to a single layer $\text{Li}_7\text{La}_3\text{Zr}_2\text{O}_{12}:\text{Ga}_2\text{O}_3$ thin film. A decrease in conductivity was observed for multilayer thin films with a homogenous distribution of layers if the thickness per layer was below 160 nm. In this case, the increase in the number of layers (lattice relaxation)

cannot compensate the effect of high resistances at the layer interfaces (charge transport resistance at the grain boundaries). This demonstrates that the garnet/garnet interfaces have a higher resistance compared to the “bulk” of the thin film. Therefore, thin film interfaces are not desirable due to the high resistance, but the resulting lattice relaxation superimposes this effect if the density of interfaces is kept low. These results show that the conductivity of garnet-type thin films strongly depends on deposition temperature and on substrate quality (lattice matching). A detailed model for the different conductivity behavior of the garnet-type thin films will be introduced in chapter 5.2.6 after the conductivity measurements in lateral geometry.

Similar results were obtained by Kim et al. [56] who prepared $\text{Li}_7\text{La}_3\text{Zr}_2\text{O}_{12}:\text{Al}_2\text{O}_3$ garnet-type thin films by PLD on garnet-type $\text{Gd}_3\text{Ga}_5\text{O}_{12}$ (GGG) substrates and observed a dependence of the conductivity on the substrate orientation. For (100) oriented GGG they obtained conductivities of $\sigma = 2.5 \cdot 10^{-6} \text{ S}\cdot\text{cm}^{-1}$ and $\sigma = 1.0 \cdot 10^{-5} \text{ S}\cdot\text{cm}^{-1}$ for (111) oriented GGG with activation energies of 0.55 eV and 0.52 eV, respectively. The conductivities were measured in lateral geometry. These results show the impact of the substrate on the conductivity of the garnet-type thin film. The conductivity determined by Kim et al. for a (100) oriented $\text{Li}_7\text{La}_3\text{Zr}_2\text{O}_{12}:\text{Al}_2\text{O}_3$ is in good agreement to the measured conductivity of a single layer garnet-type $\text{Li}_{6.5}\text{La}_3\text{Zr}_{1.5}\text{Ta}_{0.5}\text{O}_{12}:\text{Al}_2\text{O}_3$ thin film on $\text{MgO}(100)$. The conductivity of the $\text{Li}_7\text{La}_3\text{Zr}_2\text{O}_{12}:\text{Al}_2\text{O}_3$ thin film prepared by Kim et al. on a (111) oriented GGG is comparable to the conductivity of the multilayer garnet-type thin films presented in this study. However, the activation energies of the conductivity differ by about 0.1 eV. The temperature region for the determination of activation energies by the group of Kim et al. was quite narrow (25 °C - 80 °C) and the impedance was only measured at five different temperatures.

5.2.5 Conductivity measurements in axial geometry

The axial conductivity of garnet-type thin films on top of ITO substrates was determined by electrochemical impedance spectroscopy and by dc polarization. The activation energy of the conductivity was determined by measuring the electrochemical impedance as a function of temperature. An impedance measurement for a $\text{Li}_6\text{BaLa}_2\text{Ta}_2\text{O}_{12}$ garnet-type thin film with a thickness of 1 μm can be seen in Figure 30. The depicted measurements

were taken at 0 °C and at 70 °C with an applied amplitude of 10 mV. The measurement was conducted using an extended ITO electrode (1 cm²) and a 1 mm circular gold electrode. Figure 30 a) and b) show the Nyquist plot of the measurements at 0 °C and 70 °C, respectively. The measured data are shown as open circles whereas the fitted data are shown as red, solid line. The equivalent circuit used for the fit is displayed in the upper left corner of the plots. The equivalent circuit consists of a resistor parallel to a constant phase element (RQ) which was used to fit the high frequency term of the impedance data. The semicircle at lower frequencies was fitted using again a constant phase element connected parallel to a resistance. Figure 30 c) and d) show the respective Bode plots of the garnet-type thin film sample. It can be seen that the temperature dependence of the total resistance is small in a temperature range from 0 °C to 70 °C. Nevertheless, the sample showed a reduced total resistance with increasing temperature.

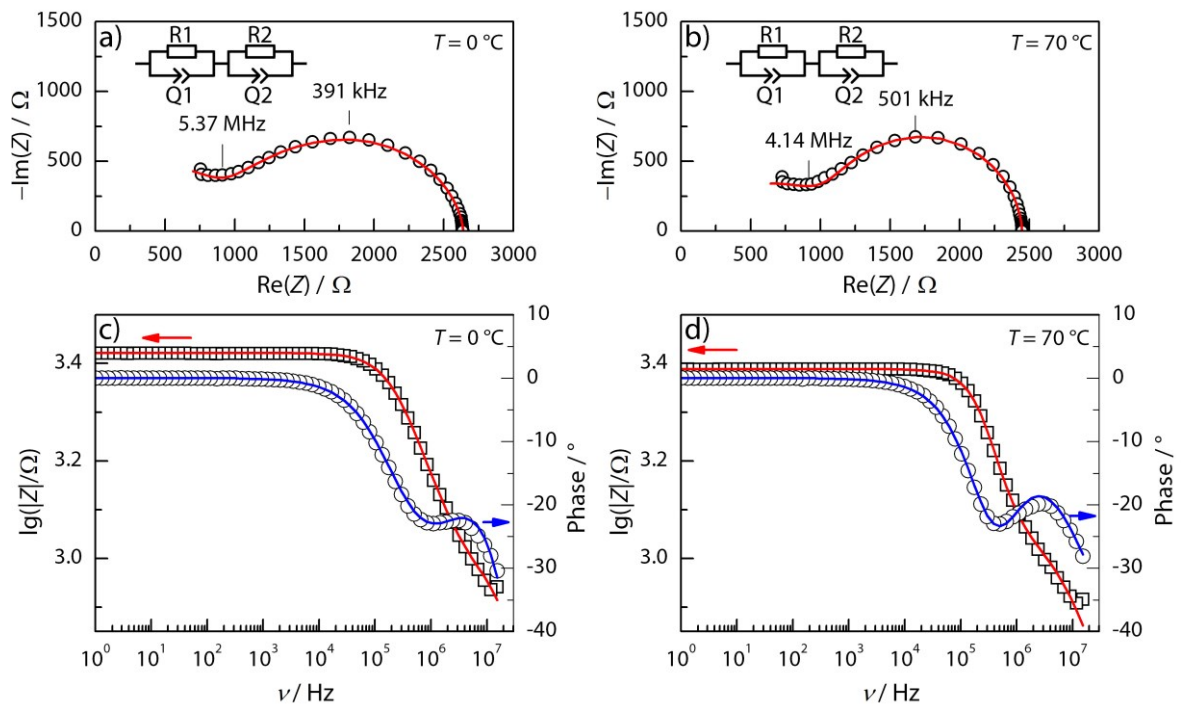


Figure 30: The electrochemical impedance behavior of a garnet-type $\text{Li}_6\text{BaLa}_2\text{Ta}_2\text{O}_{12}$ thin film sample on an ITO substrate is shown. The measurements were taken at 0 °C and at 70 °C. a) and c) show the impedance measurement at 0 °C as and b) and d) show the respective measurement at 70 °C as Nyquist and Bode plots.

The conductivity determined from the total resistance was $\sigma = 6 \cdot 10^{-6} \text{ S} \cdot \text{cm}^{-1}$ ($R = 2584 \text{ } \Omega$) at $25 \text{ } ^\circ\text{C}$. The conductivity is thereby higher compared to a $\text{Li}_6\text{BaLa}_2\text{Ta}_2\text{O}_{12}$ garnet-type thin film measured lateral, but lower than the conductivity of the bulk ceramic samples [43, 44, 105]. The activation energy of the conductivity was calculated to be $E_a = 0.04 \text{ eV}$ from the fit of the slope of $\ln(\sigma T)$ versus $(1/T)$, as seen in Figure 31 (here $1000/T$ was used for the abscissa). This result is unexpected since the typical activation energy of the conductivity of $\text{Li}_6\text{BaLa}_2\text{Ta}_2\text{O}_{12}$ garnet-type thin films is about $E_a \approx (0.4 - 0.5) \text{ eV}$ and the activation energy for garnet-type bulk materials ranges between $0.2 \text{ eV} - 0.5 \text{ eV}$ [9, 18, 39, 42, 44, 118, 119]. Hence, it can be assumed that the determined activation energy does not represent ionic transport across the garnet-type thin film. The measured activation energy of 0.04 eV belongs more likely to the ITO substrate for which an activation energy of the conductivity of 0.02 eV was determined in a separate measurement.

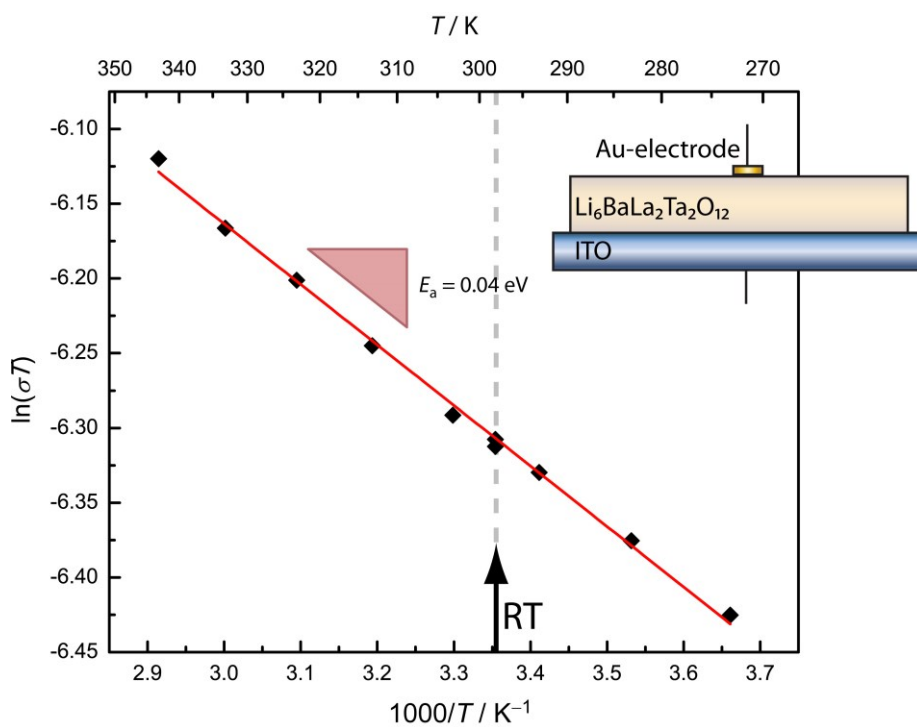


Figure 31: Total conductivity (from ac impedance) of an axially measured $\text{Li}_6\text{BaLa}_2\text{Ta}_2\text{O}_{12}$ garnet-type thin film. The conductivity was calculated from the slope of the linear fit. The black squares represent the measured data, the red solid line represents the linear fit. Additionally, an arrow with a dashed grey line indicates room temperature.

In order to specify the measured conductivity, ionic or electronic, dc polarization measurements with blocking electrodes (Pt and Au) were conducted. The 1 μm thick sample was polarized in a range from -1 V to 1 V , at $25\text{ }^\circ\text{C}$, showing ohmic behavior with a resistance of $2586\text{ }\Omega$ (Figure 32) which is in good agreement with the electrochemical impedance measurement at $25\text{ }^\circ\text{C}$ being $2584\text{ }\Omega$. It has to be remembered that the electrochemical impedance measurement gives the total resistance, whereas the dc polarization measurement with blocking electrodes yields the electronic resistance. Since the obtained resistance values agree well one can consequently assume that the determined conductivity is mainly caused by electrons/electron holes meaning that a short circuit has occurred. This behavior could be observed throughout all axial conductivity measurements of single garnet-type thin films on ITO and on platinum coated $\text{MgO}(100)$ substrates.

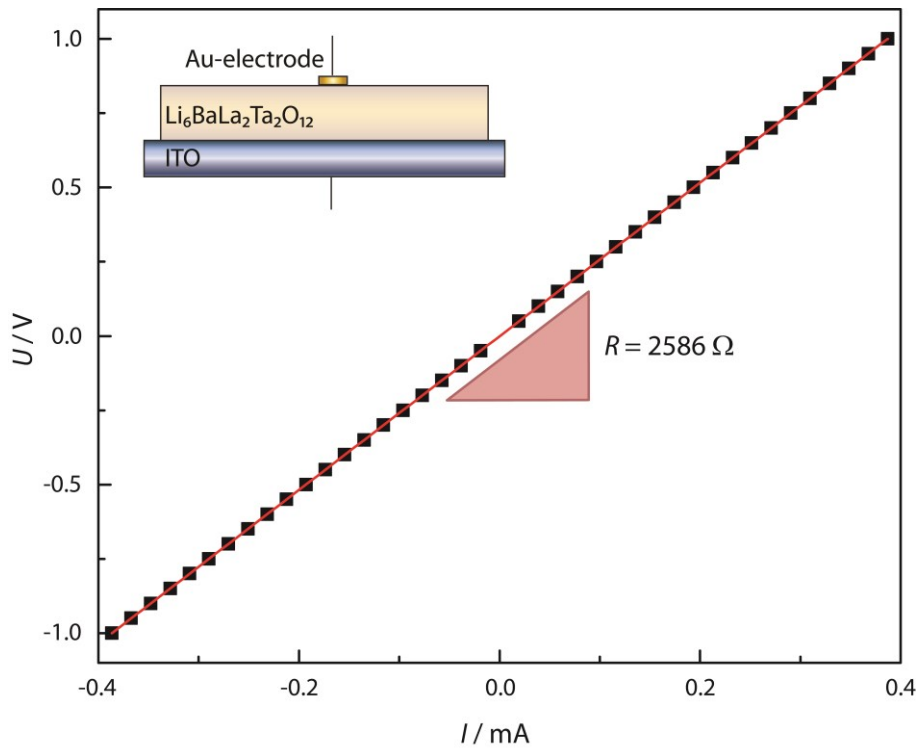


Figure 32: dc polarization measurement of a 1 μm thick garnet-type $\text{Li}_6\text{BaLa}_2\text{Ta}_2\text{O}_{12}$ thin film sample with blocking electrodes ($\vartheta = 25\text{ }^\circ\text{C}$). An ohmic resistance was received.

In the end, axial conductivity measurements of $\text{Li}_6\text{BaLa}_2\text{Ta}_2\text{O}_{12}$ garnet-type thin films were successful when multiple $\text{Li}_6\text{BaLa}_2\text{Ta}_2\text{O}_{12}$ thin films were deposited on top of each

other. For this purpose a platinum coated MgO(100) substrate was heated to the deposition temperature of $\text{Li}_6\text{BaLa}_2\text{Ta}_2\text{O}_{12}$ and 10,000 pulses were applied. Thereafter, the substrate was cooled to 50 °C from ~550 °C with a rate of 15 °C/min. After reaching 50 °C, the substrate was heated again and the next $\text{Li}_6\text{BaLa}_2\text{Ta}_2\text{O}_{12}$ thin film (10,000 pulses) was deposited. This process was continued until a total of four $\text{Li}_6\text{BaLa}_2\text{Ta}_2\text{O}_{12}$ garnet-type thin films ($d_{\text{tot}} \approx 3.5 \mu\text{m}$) were deposited onto each other. The impedance spectrum of a $\text{Li}_6\text{BaLa}_2\text{Ta}_2\text{O}_{12}$ thin film prepared in such a manner is shown in Figure 33 at 0 °C and at 70 °C as Nyquist and as Bode plot, respectively. Figure 33 a) and b) shows the Nyquist plot of the sample at 0 °C and 70 °C. The measured frequency range was larger than displayed in the Nyquist plot. An enlarged selection of data points is presented in order to show the semicircle of the material, otherwise the scaling due to the electrode impedance would not allow an observation. The measured data is shown as open circles. The fit of the measured data is shown as a red line. The equivalent circuit model used for the fit comprised of a resistance parallel to a constant phase element in series with a constant phase element $(R_1Q_1)Q_2$. This equivalent circuit was the simplest equivalent circuit that is mathematically capable of describing the measured data. The resistance parallel to the constant phase element describes the non-ideal semicircle of the sample at high frequencies. The constant phase element in series to the (RQ) describes the blocking behavior of the electrodes and was used instead of a capacity due to the fact that the phase angle slightly differs from -90° . The obliterated semicircle resulting from the garnet-type material and the constant phase element of the blocking electrode have similar time constants, which lead to a merged impedance response. This complicates the fit as only half the data points of a semicircle are accessible at low temperatures. Furthermore, the number of data points that originate from the garnet-type material (semicircle) decrease with increasing temperature. This is caused by a non-equivalent shift of the time constants of the garnet-type material (semicircle) and of the gold electrode (constant phase element) to higher frequencies with increasing temperature. Subsequently, the data at 70 °C could not be fitted because there were not enough data points that belonged to the garnet material semicircle as can be seen from the inset in Figure 33 b). The corresponding Bode plots of the impedance spectra of a $\text{Li}_6\text{BaLa}_2\text{Ta}_2\text{O}_{12}$ garnet-type thin film measured in axial geometry at 0 °C and at 70 °C are shown in Figure 33 c) and d), respectively.

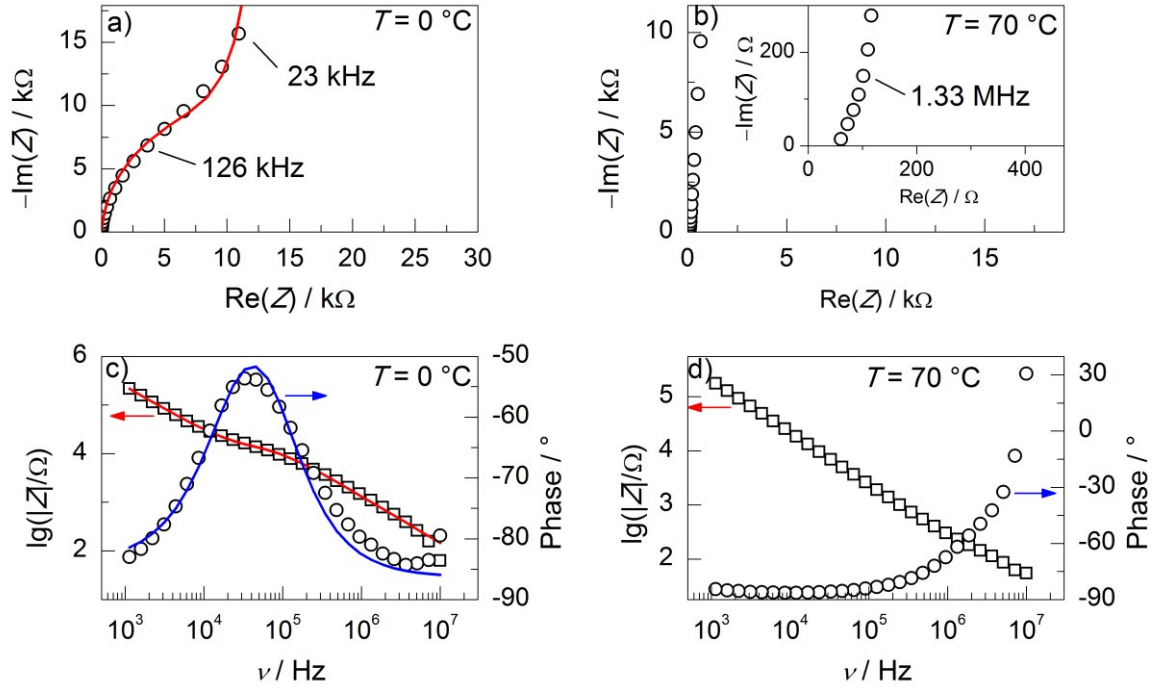


Figure 33: The electrochemical impedance behavior of a garnet-type $\text{Li}_6\text{BaLa}_2\text{Ta}_2\text{O}_{12}$ thin film sample deposited in four consecutive steps on a platinum coated $\text{MgO}(100)$ substrate is shown. The measurements were taken at $0\text{ }^\circ\text{C}$ and at $70\text{ }^\circ\text{C}$. a) and c) show the impedance measurement at $0\text{ }^\circ\text{C}$ as Nyquist and Bode plot. b) and d) show the respective measurement at $70\text{ }^\circ\text{C}$ as Nyquist and Bode plot.

The resulting conductivity of the sample at $0\text{ }^\circ\text{C}$ was determined to be $\sigma = 5 \cdot 10^{-6}\text{ S}\cdot\text{cm}^{-1}$ ($R_1 = 10.08\text{ k}\Omega$; $Q_1 = 2.67 \cdot 10^{-10}\text{ Fs}^{(a-1)}$, exponent $a = 0.97$; $Q_2 = 1.18 \cdot 10^{-9}\text{ Fs}^{(a-1)}$, exponent $a = 0.93$), with a sample thickness of $3.2\text{ }\mu\text{m}$ (determined from secondary electron microscopy cross section) and an electrode area of $6.36 \cdot 10^{-3}\text{ cm}^2$ ($\pi \cdot 0.045^2\text{ cm}^2$), which was derived from the small circular gold electrode. The reduced electrode area compared to the 0.5 mm radius of the mask is caused by shading during thermal evaporation.

The conductivity at $25\text{ }^\circ\text{C}$ was determined to be $\sigma = 3.3 \cdot 10^{-5}\text{ S}\cdot\text{cm}^{-1}$. The specimen had an activation energy of the conductivity of $E_a = 0.5\text{ eV}$. The activation energy was derived from the slope of the linear fit from $\ln(\sigma T)$ versus $(1/T)$ in the temperature range from $-24\text{ }^\circ\text{C}$ to $65\text{ }^\circ\text{C}$. The respective Arrhenius plot is shown in Figure 34.

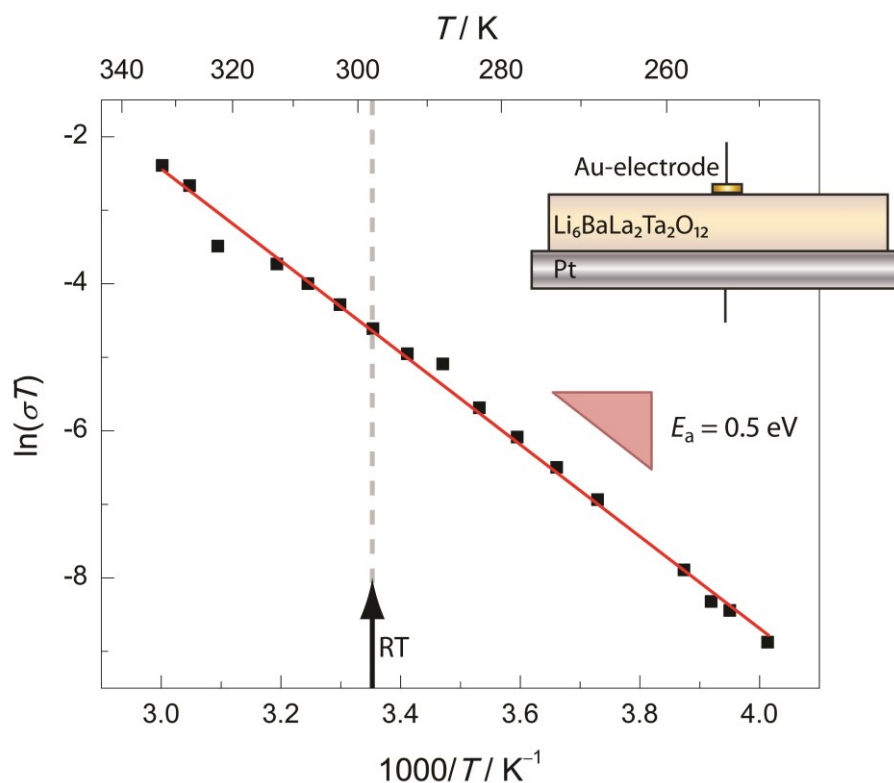


Figure 34: Arrhenius plot of an axially measured $\text{Li}_6\text{BaLa}_2\text{Ta}_2\text{O}_{12}$ garnet-type thin film ($3.2 \mu\text{m}$ thick). The thin film was deposited in four consecutive steps on a $\text{MgO}|\text{Pt}$ substrate. The activation energy of the charge transfer was calculated from the slope of the linear fit. The black squares represent the measured data; the red, solid line represents the fit. Additionally, an arrow with a dashed grey line indicates room temperature.

dc polarization measurements were performed on the garnet-type $\text{Li}_6\text{BaLa}_2\text{Ta}_2\text{O}_{12}$ thin film sample that was deposited in four consecutive steps. The large platinum counter electrode (1 cm^2) was polarized positively relative to the small, circular gold working electrode ($6.36 \cdot 10^{-3} \text{ cm}^2$). The potential difference between the two electrodes was raised in 0.2 V steps from 0 V until 5 V were reached. The potential difference applied in each step was constant for 20 minutes, which was sufficient to receive a steady state current. Figure 35 a) shows the current transient (current as a function of time) at a potential difference of 2 V . It can be seen that a stable steady state current was received after at least 15 minutes. In order to determine the value of the steady state current a linear fit with a fixed slope of $0 \text{ A} \cdot \text{s}^{-1}$ was carried out at the last 5 minutes of the respective current transient. The steady state current of each polarization potential was then plotted as a function of the applied voltage as is shown in Figure 35 b). The current response can be

separated in three parts. Part I (0 V - 1.6 V) shows a plateau. Here, the current is a linear function of the applied voltage and has a value of about $I = 3.6 \cdot 10^{-11}$ A at $U = 0.2$ V, resulting in an electronic conductivity of $\sigma_{el} = 3.6 \cdot 10^{-11}$ S·cm⁻¹. Part II (1.6 V - 3.8 V) shows a strong increase of the current as a function of the applied voltage. Part I and part II together look like a Hebb-Wagner polarization plot with the exception that two blocking electrodes were used. The reason for the shape of part I and part II is the same as for the Hebb-Wagner polarization plot of the bulk garnet-type sample (cf. chapter 5.1.2). In part I the contribution from electrons and electron holes was almost equal and both compensate each other. The current increase in part II was caused by polarization of lithium ions towards the gold electrode, which lead to an electron hole dominance as described in Eq. 5.6.

$$\text{Li}_{\text{Li}}^{\times} = \text{V}_{\text{Li}}' + \text{h}^{\bullet} + \text{Li}_{\text{S}} \quad (5.6)$$

A maximum of the current $I_{\text{max}} = 3 \cdot 10^{-9}$ A is reached at $U = 3.8$ V, resulting in an electronic conductivity of $\sigma_{el} = 4 \cdot 10^{-11}$ S·cm⁻¹. The increase in electronic conductivity is marginal, yet distinct.

The current decreased again for potential differences greater than 3.8 V (part III). This is probably caused by a decomposition of the garnet-type material. The resulting (decomposed) material has a lower electronic conductivity (in sum) in comparison to the initial garnet-type material. The decomposition of the garnet-type material starts at about 3.8 V applied between the platinum and the gold electrode. A reference potential cannot be given for this process as the responsible redox couple is unknown. The local current minimum is reached at $U = 5$ V with $I = 2.6 \cdot 10^{-9}$ A. The calculated electronic conductivity is $\sigma_{el} = 2.6 \cdot 10^{-11}$ S·cm⁻¹. The error of each data point was deduced from the error of the intercept from the linear fit of the current versus time plot. As a guide to the eye a red line is indicated in part I and part II of the plot (the indicated line does not represent a mathematical model).

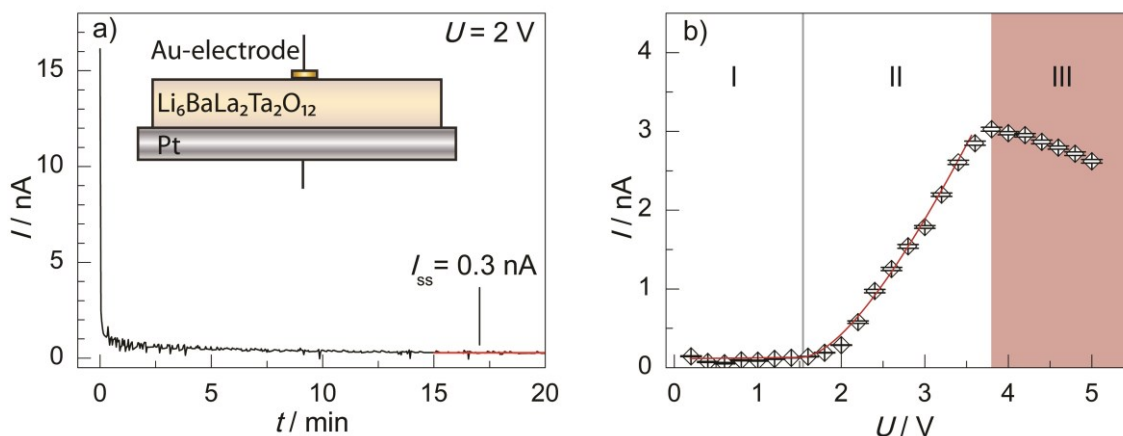


Figure 35: dc polarization measurement of an axially measured Li₆BaLa₂Ta₂O₁₂ garnet-type thin film (3.2 μ m thick) deposited in four consecutive steps on a platinum coated MgO(100) substrate with a circular gold electrode on top. a) Current transient at a potential difference of 2 V between the gold and the platinum electrode. The steady state current was deduced from a linear fit of the last 5 minutes. b) Plot of the steady state current versus the applied voltage. The red line is only a guide to the eye and does not represent a mathematical model.

5.2.6 Conductivity model

Garnet-type thin films show a columnar microstructure in growth direction. Furthermore, grain boundaries and interfaces appear to have higher impedance than the bulk of the grains. These two characteristics are the basis for the conductivity model outlined schematically in Figure 36. Figure 36 a) is a detail of a garnet-type thin film where a grain in contact with other grains can be seen. The inner regions of a grain (yellow) show bulk (ceramic) conductivity. Grain boundaries (black) are surrounded by regions of reduced conductivity (red). In general the pictograms show by their color distribution whether the respective thin film has a high (high fraction of yellow in the pictogram) or low (high fraction of red in the pictogram) conductivity.

A single layer thin film with a columnar microstructure (Figure 36 b) has many grain boundaries perpendicular to the substrate. The resistances of the grains and of the grain boundaries sum up to one resistance if the conductivity is determined in lateral geometry (parallel to the substrate). Due to the capacity of the substrate which is parallel to this

resistance only one semicircle can be seen in the impedance measurement. If conductivity measurements are performed in axial geometry, the bulk resistance is parallel to the larger grain boundary resistance, thereby the total resistance is smaller compared to the resistance in lateral geometry. The conductivity determined in axial geometry is thereby higher. In axial geometry only one semicircle can be seen because the grains and the grain boundaries are parallel to each other resulting in one (RC) with contributions of grains and grain boundaries. The substrate impedance is not measured in this geometry.

If the columnar microstructure is interrupted by the deposition of multilayers (Figure 36 c) lattice matched growth and relaxation of strain is possible. Each layer acts as a buffer layer for the subsequent layer. Thereby the crystallite size is increased (the columns get wider) and the density of grain boundaries is reduced. As an effect a higher conductivity of the multilayer structures compared to single layer thin films can be measured in lateral geometry. This conductivity approaches the conductivity of the bulk ceramic material. Conductivity measurements have shown only one semicircle due to the capacity of the substrate (lateral geometry).

If the number of multilayers (Figure 36 d) is further increased while maintaining the film thickness the interface/grain boundary density is raised. The number of grain boundaries is reduced due to the multilayer structure in xy -direction but as a consequence an increase of grain boundaries in z -direction is achieved. This is the reason why conductivity measurements conducted on multilayer thin films in lateral geometry showed a decreasing conductivity with increasing interface/grain boundary density.

If one thick garnet-type layer is deposited onto multiple thin garnet-type buffer layers (Figure 36 e) the crystallite size increases with each layer. This leads to an increased conductivity of the thin film compared to a single layer thin film in lateral direction.

For verification, a determination of the crystallite size of multilayer thin films would be necessary. This is not possible by XRD because the different garnet-type materials have a slightly different lattice constant which leads to a broadening of the reflexes as can be seen in Figure 22. Hence, to verify this conductivity model high resolution TEM studies would be necessary.

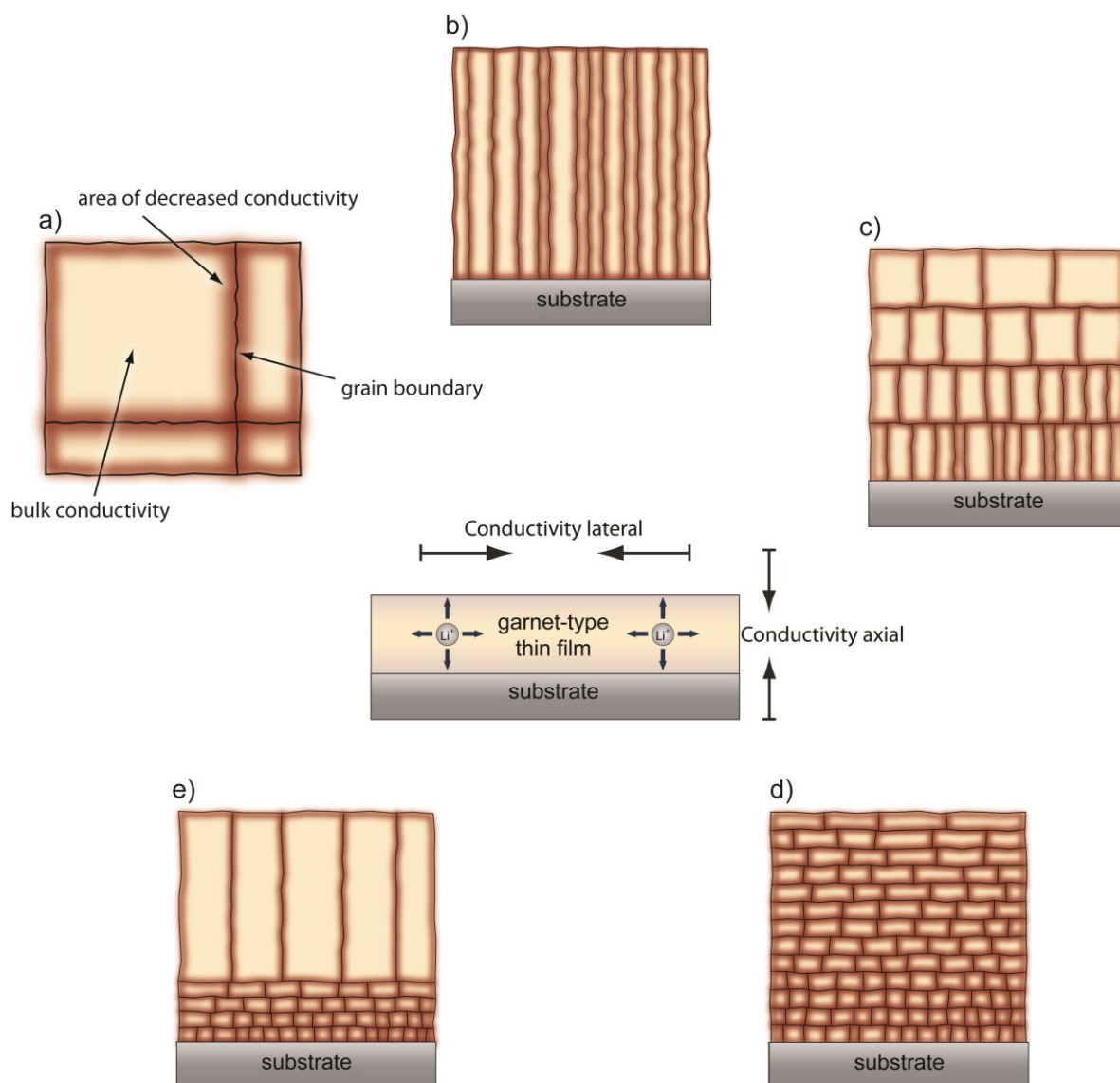


Figure 36: Illustration of the conductivity model for garnet-type thin films prepared by pulsed laser deposition. a) Detail of a garnet-type thin film. The grain boundaries show decreased conductivity. b) Single layer thin film with columnar growth. c) Multilayer thin film with interrupted columnar growth. d) Multilayer thin film with a high interface/grain boundary density. e) Four garnet-type buffer layers with a garnet-type thin film on top.

5.2.7 Protective coatings

There are several variants possible for the use of garnet-type thin films as protective coatings. There can be either a coating of the electrode(s), in particular the coating of the positive or/and negative electrode(s). Another option is to apply a coating on the surface of another solid electrolyte which is not stable versus a specific component of the cell e.g., metallic lithium. The advantage hereby is to benefit from the properties of both materials – the protective coating material and the material that is thereby coated. The combination should of course yield more beneficial material properties than the unprotected material has itself.

Figure 37 shows a good example of such a beneficial combination. Here, a commercially available Ohara electrolyte (Ohara Inc., Kanagawa, Japan), which is a NASICON-type glass ceramic, was coated with a thin layer of garnet-type $\text{Li}_6\text{BaLa}_2\text{Ta}_2\text{O}_{12}$. The deposited thin film had a thickness of about 200 nm and was applied as two circular areas. Figure 37 a) shows the pristine Ohara electrolyte sample where the $\text{Li}_6\text{BaLa}_2\text{Ta}_2\text{O}_{12}$ covered areas are indicated by arrows. Metallic lithium was mechanically pressed onto the sample surface and remained there for 12 h. The lithium was peeled off afterwards. It can be seen from Figure 37 b) that the $\text{Li}_6\text{BaLa}_2\text{Ta}_2\text{O}_{12}$ covered areas remain white and unchanged after being exposed to metallic lithium. The unprotected areas of the Ohara electrolyte in contrast show a discoloration, the material gets blackened. Thereby, it can be seen that Ohara electrolyte is chemically unstable versus metallic lithium, but a thin layer of a garnet-type material can be applied as protective coating. Figure 37 c) shows a cross section of the $\text{Li}_6\text{BaLa}_2\text{Ta}_2\text{O}_{12}$ garnet-type thin film with a thickness of about 200 nm on top of the Ohara electrolyte in a SEM. The garnet-type coating forms a smooth, dense and electron blocking barrier on top of the Ohara electrolyte.

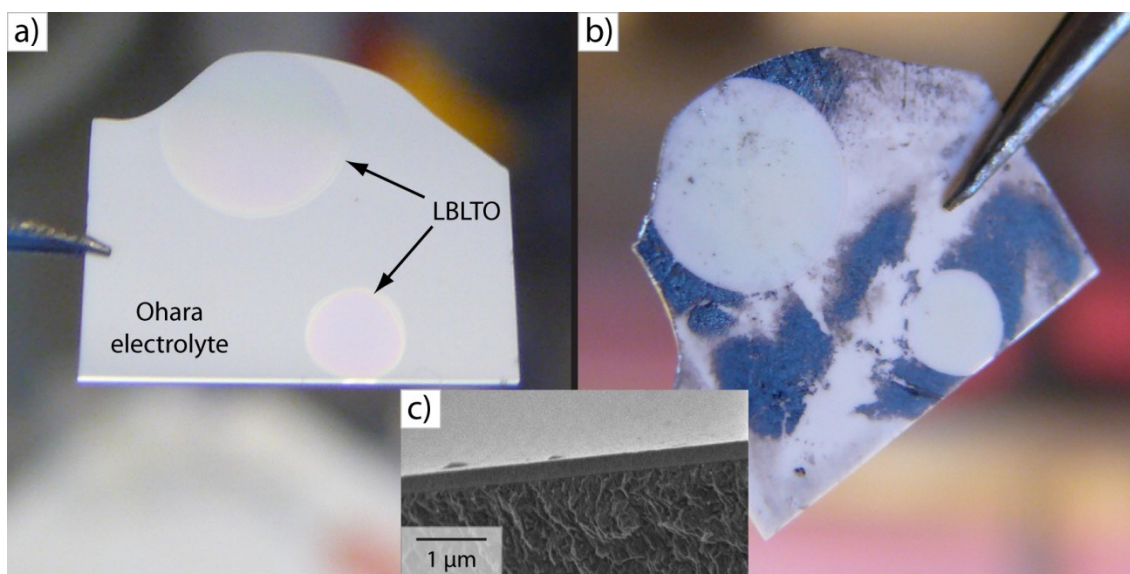


Figure 37: An Ohara glass ceramic electrolyte was coated in two circular areas with a $\text{Li}_6\text{BaLa}_2\text{Ta}_2\text{O}_{12}$ thin film. The Ohara electrolyte with NASICON structure is chemically not stable versus metallic lithium. a) Pristine Ohara sample before it was in contact with metallic lithium. b) The sample after 12 h in contact with metallic lithium. The areas with $\text{Li}_6\text{BaLa}_2\text{Ta}_2\text{O}_{12}$ coating remain white, whereas the uncoated areas show a color change. The inset c) at the bottom of the figure shows a cross section of the 200 nm thick $\text{Li}_6\text{BaLa}_2\text{Ta}_2\text{O}_{12}$ film on top of the Ohara electrolyte viewed in a SEM.

In addition to the coating of another solid electrolyte by a garnet-type thin film, coatings of electrode materials are also possible. For this example a $\text{Li}_4\text{Ti}_5\text{O}_{12}$ ceramic pellet that could be used as anode material was polished and a layer of $\text{Li}_6\text{BaLa}_2\text{Ta}_2\text{O}_{12}$ was applied via pulsed laser deposition. Figure 38 shows the results of the SEM measurement. Figure 38 a) shows an illustration of the prepared sample and gives an overview of the different SEM pictures that were taken. Figure 38 b) depicts a cross section image in which the well-covering $\text{Li}_6\text{BaLa}_2\text{Ta}_2\text{O}_{12}$ thin film with a thickness of about $1.5\ \mu\text{m}$ is shown on top of the $\text{Li}_4\text{Ti}_5\text{O}_{12}$ bulk sample. Pores resulting from the sintering process can be observed in the cross section of the $\text{Li}_4\text{Ti}_5\text{O}_{12}$ sample. Figure 38 c) represents a top view SEM picture of the sample. Here, the border between the $\text{Li}_6\text{BaLa}_2\text{Ta}_2\text{O}_{12}$ thin film and the $\text{Li}_4\text{Ti}_5\text{O}_{12}$ bulk sample is shown. The $\text{Li}_6\text{BaLa}_2\text{Ta}_2\text{O}_{12}$ thin film is on the left hand side of the picture and the $\text{Li}_4\text{Ti}_5\text{O}_{12}$ bulk sample is on the right hand side. It can be seen that the pores in the bulk $\text{Li}_4\text{Ti}_5\text{O}_{12}$ sample can also be observed in the top view SEM picture (uncovered area) but that the pores get covered by the garnet-type thin film in the coated

area. Figure 38 d) shows a SEM top view picture taken from the middle of the sample. The $\text{Li}_6\text{BaLa}_2\text{Ta}_2\text{O}_{12}$ thin film seems to be highly crystalline and appears to have no pores, pinholes or cracks. The garnet-type material forms a dense layer on top of the $\text{Li}_4\text{Ti}_5\text{O}_{12}$ pellet.

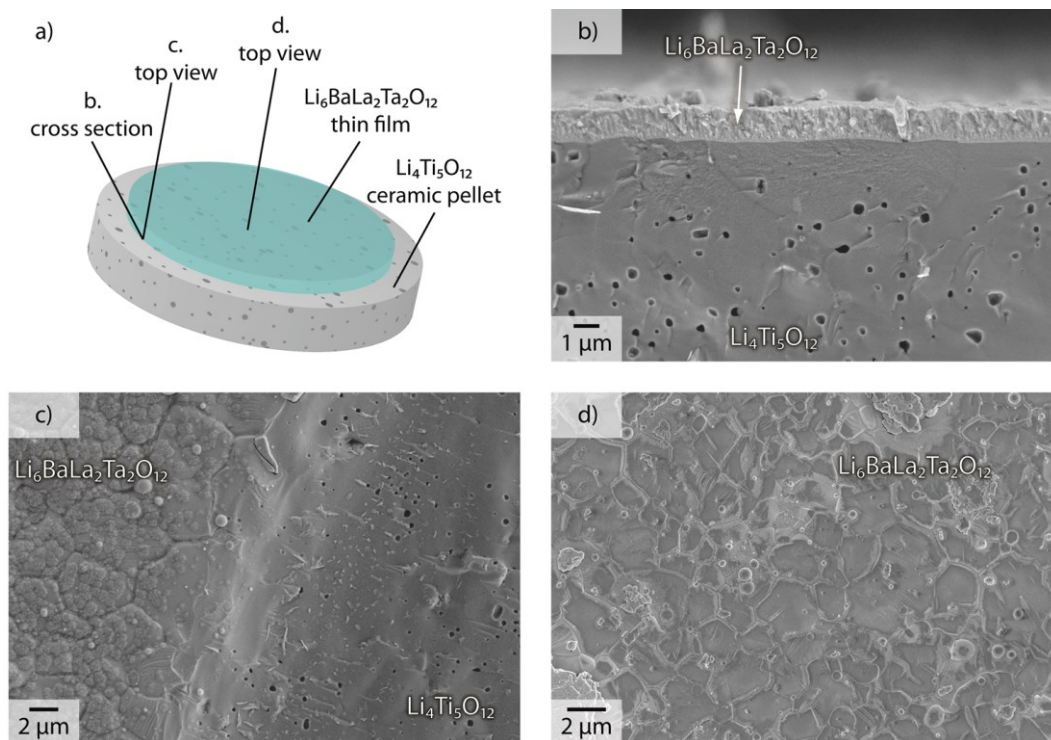


Figure 38: $\text{Li}_6\text{BaLa}_2\text{Ta}_2\text{O}_{12}$ thin film applied to a $\text{Li}_4\text{Ti}_5\text{O}_{12}$ ceramic pellet. a) Illustration of the sample. The different areas of the SEM pictures are indicated. b) Cross section of the garnet-type thin film (top – light grey) on top of the $\text{Li}_4\text{Ti}_5\text{O}_{12}$ bulk material (bottom – dark grey). Many pores can be seen in the $\text{Li}_4\text{Ti}_5\text{O}_{12}$ bulk material. c) Top view of the sample at the border between the $\text{Li}_6\text{BaLa}_2\text{Ta}_2\text{O}_{12}$ thin film coating (left) and the $\text{Li}_4\text{Ti}_5\text{O}_{12}$ bulk material (right). d) Top view SEM picture taken from the middle of the sample depicting the garnet-type thin film coating.

This sample was not used as a battery electrode and served only to demonstrate the ability of garnet-type thin films to cover bulk electrode materials.

Hence, it was shown that garnet-type thin film coatings can be successfully deposited on a variety of other materials. These coatings can be used on other solid electrolyte materials or on electrode materials. Thereby, the thin film coating can increase chemical

stability as shown for the Ohara electrolyte and is furthermore capable to even out small pores. However, only materials that are stable during the deposition process ($p_{O_2} = 5 \cdot 10^{-2}$ mbar, $\vartheta \approx 500$ °C - 600 °C) can be used as substrate.

5.2.8 Ion-selective membranes

Anodized aluminum oxide coated with garnet-type material was subject of permeation testing before applying the ion-selective membranes to galvanic cells. Therefore, a dye concentration cell was used where one side contained methyl red and the other side was filled with 2-propanol. The two liquid-containing compartments were separated by a $\text{Li}_6\text{BaLa}_2\text{Ta}_2\text{O}_{12}$ coated anodized aluminum oxide membrane.

Figure 39 shows the dye concentration experiment where a), b) and c) show the starting time of the experiment and d), e) and f) show the measurement after a certain time. The experiment was performed with three different membranes. The first set (Figure 39 a) served as reference for the following experiments. It contained a laminated but uncoated anodized aluminum oxide membrane as separator between the two liquid compartments. It can be seen that mixing of both liquids took place immediately. The right compartment already showed an orange discoloration at $t = 0$ s. During the filling of the concentration cell the dye already entered the 2-propanol compartment. The uncoated membrane is unable to prevent a mixing of the liquids (Figure 39 d).

Figure 39 b) shows a coated anodized aluminum oxide membrane that was laminated and placed between the two glass tubes. It was possible to fill the cell with both liquids without mixing. However, after 25 minutes a diffusion of the dye was observed (Figure 39 e). An anodized aluminum oxide membrane coated with garnet-type material that was additionally sealed as described in the experimental section was used for the dye concentration experiment in Figure 39 c). No mixing of the dye and 2-propanol could be observed over a longer period of time. Figure 39 f) shows the status of the experiment after 24 hours.

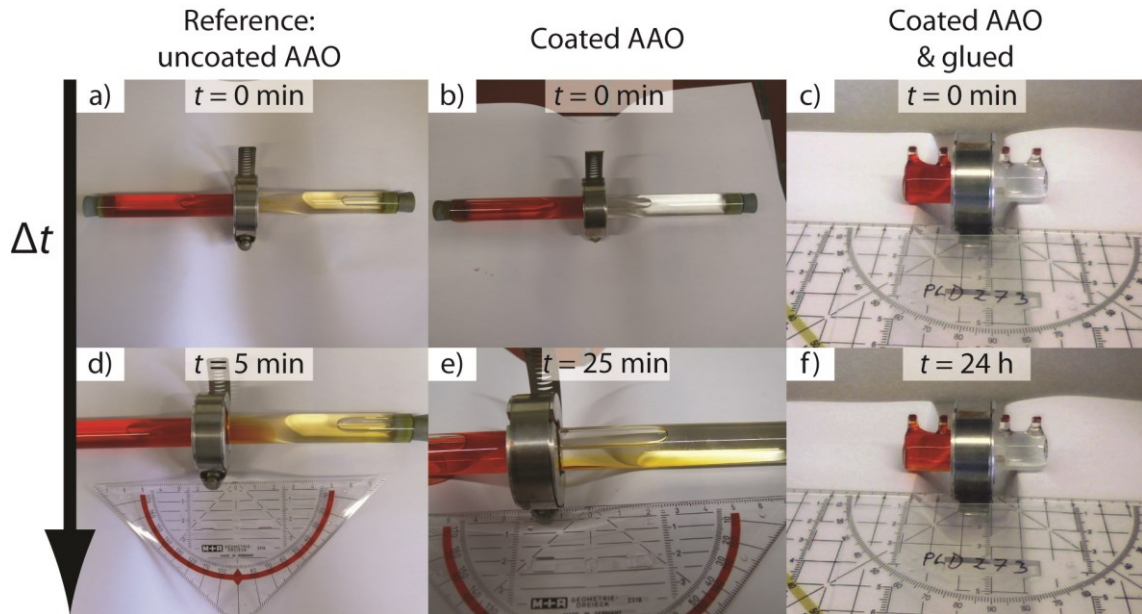


Figure 39: Dye concentration experiment for permeation testing. a) Uncoated anodized aluminum oxide. b) Anodized aluminum oxide coated with garnet-type material. c) Anodized aluminum oxide coated with garnet-type material. The transition between membrane and lamination foil was not sealed additionally. d) Uncoated anodized aluminum oxide after 5 minutes. e) Anodized aluminum oxide coated with garnet-type material after 25 minutes. f) Anodized aluminum oxide coated with garnet-type material with additional sealing.

The anodized aluminum oxide membrane coated with garnet-type material seen in Figure 39 b) and e) was examined after the experiment to find the cause of the dye diffusion. It turned out that the dye was able to flow around the coated membrane area. Figure 40 shows this membrane after the dye concentration experiment. The dye was able to creep in between the lamination foil and the membrane. Thereby, the liquids were able to flow around the garnet coated area whereby the liquids gained access to the pore system of the anodized aluminum oxide.

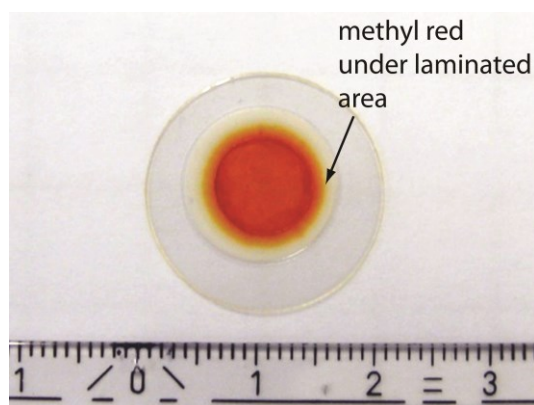


Figure 40: Coated anodized aluminum oxide without additional sealing. The liquids were able to creep under the lamination foil. Thereby, the liquids could flow around the coated area.

Hence, an additional sealing of the transition between lamination foil and membrane was necessary in order prevent the mixing of the liquids.

After verifying that the ion-selective membranes were dense they were applied to Li-S cells in cooperation with Dr. Heino Sommer (BELLA, KIT). The liquid electrolyte consisted of DME, DOL and LiTFSI without shuttle preventing additives like LiNO_3 . The discharge-charge behavior was observed for a total of 30 cycles (Figure 41). Figure 41 a) shows the evolution of the discharge-charge voltage profiles. Depicted are the cycles 1, 2, 10 and 30. It can be seen that the upper charge potential limit of 2.5 V versus Li^+/Li is reached during each cycle. Although an ion-selective membrane was used the Li-S cell still shows capacity loss during cycling. Figure 41 b) shows the specific capacity during charge and discharge as blue triangles (tip pointing upwards) and as red triangles (tip pointing downwards), respectively. Additionally, the coulombic efficiency (specific discharge divided by the specific charge) is shown as black, connected diamonds. After the first cycle the Li-S cell shows a typical drop of the specific charge. Beginning with the second cycle the specific charge is stabilized, resulting in a coulombic efficiency of 98 % after 30 cycles. Noticeable is the small specific capacity of the cell, which is caused by an increased cell resistance due to the ion-selective membrane. Thus, the cut off potential is reached faster which leads to an incomplete discharge-charge behavior, limiting the capacity.

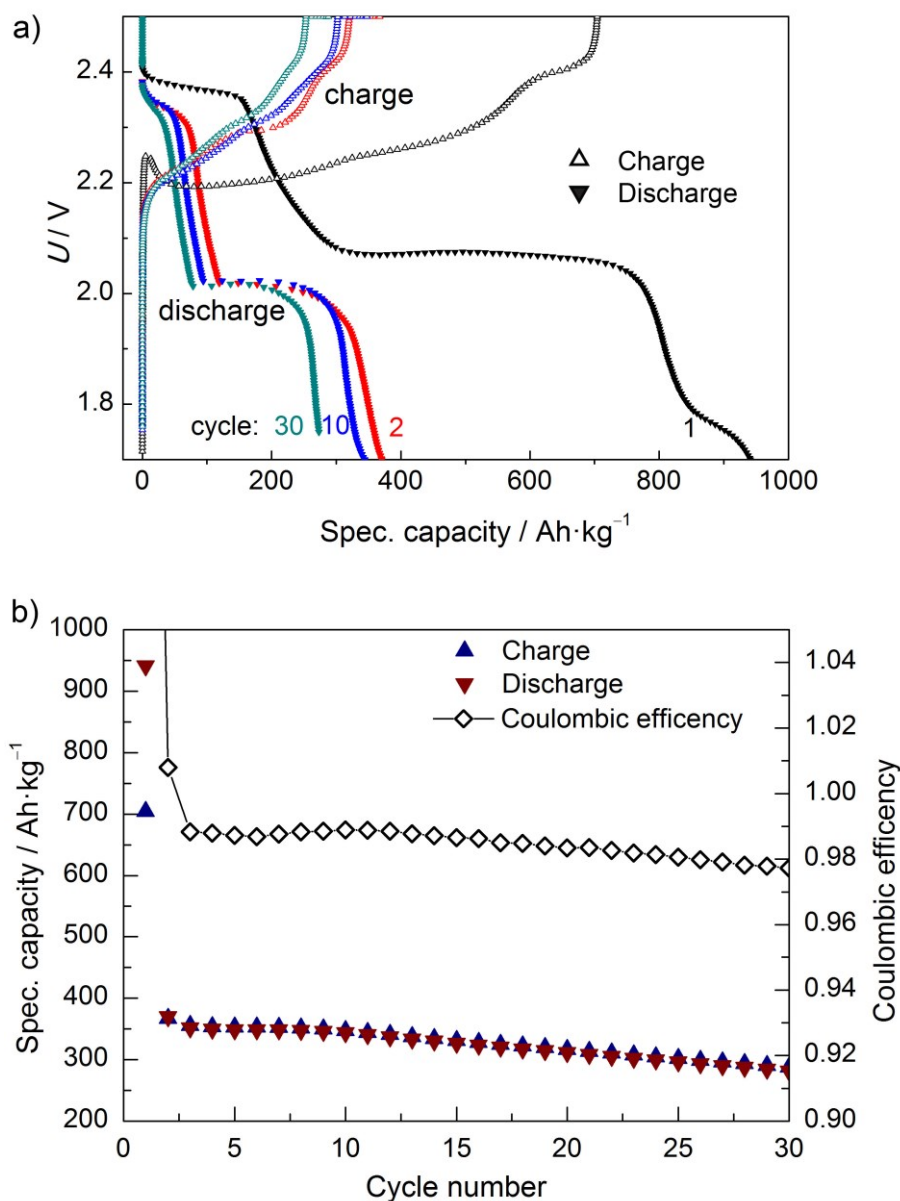


Figure 41: Discharge-charge behavior of a Li-S cell with garnet-type membrane ($\vartheta = 25\text{ }^{\circ}\text{C}$, without LiNO₃). a) Evolution of the voltage profiles. b) Specific capacity in dependence of the cycle number. Additionally, the coulombic efficiency is displayed.

In order to evaluate the discharge-charge behavior of the Li-S cell with ion-selective membrane a comparison to a Li-S cell without ion-selective membrane was conducted. Figure 42 shows the discharge-charge behavior of a Li-S cell without garnet-type coated anodized aluminum oxide membrane, or a shuttle preventing additive, over a period of five cycles. Figure 42 a) shows the evolution of the discharge-charge voltage profiles. Depicted are the cycles 1, 2 and 5. It can be seen that the upper charge potential limit of

2.5 V versus Li^+/Li is not reached due to the polysulfide shuttle. The charge process was stopped after 10 h which explains the big discrepancy between the charge and discharge capacity of the cell (Figure 42 b). The calculated coulombic efficiency is about 35 %. The comparably small coulombic efficiency is a result of the undesirable polysulfide shuttle. Nevertheless, the specific charge-discharge capacity is higher as a result of a lower cell resistance caused by omission of the ion-selective membrane.

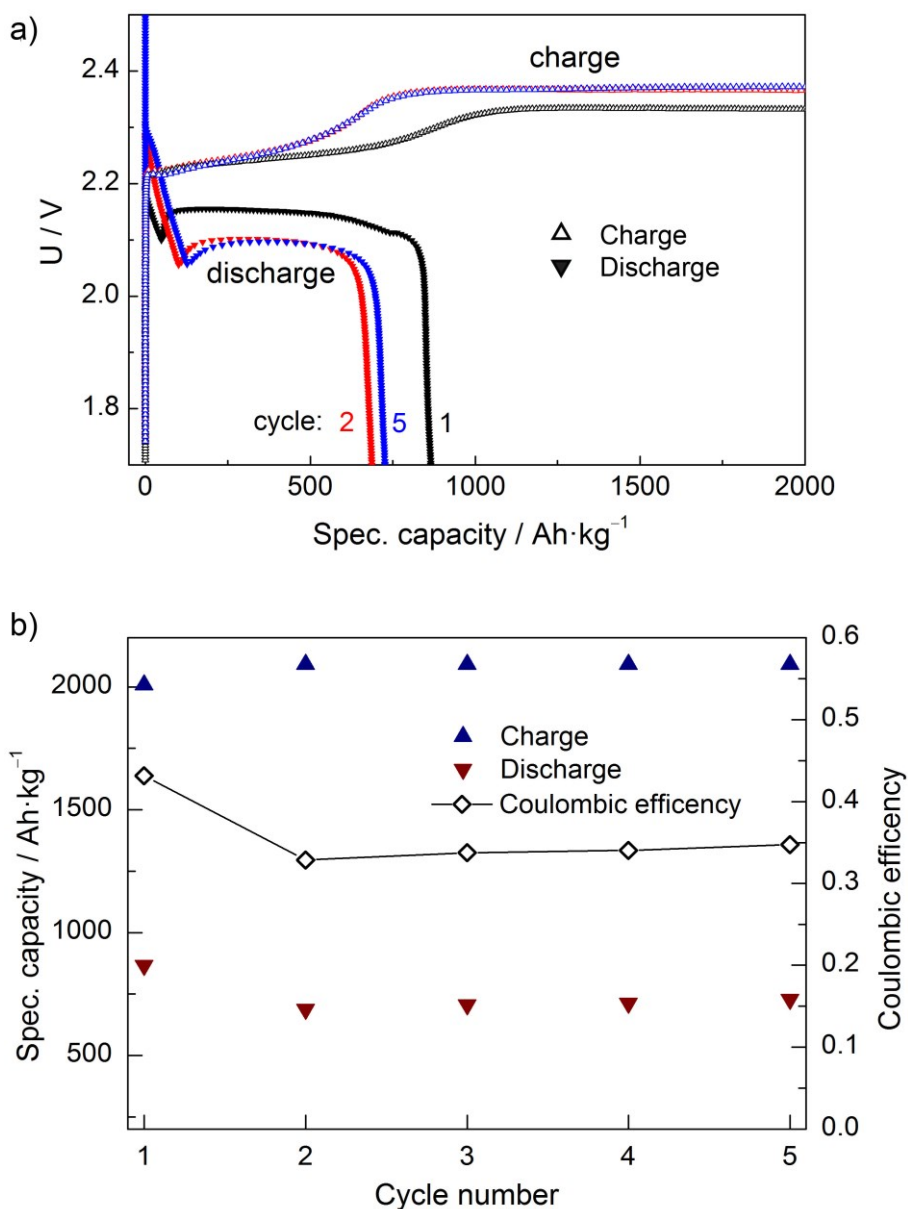


Figure 42: Discharge-charge behavior of a Li-S reference cell without ion-selective membrane ($\vartheta = 25\text{ }^{\circ}\text{C}$, without LiNO_3). a) Evolution of the voltage profiles. b) Specific capacity in dependence of the cycle number. Additionally, the coulombic efficiency is displayed.

6. Summary and Conclusions

Six different lithium ion conducting garnet-type bulk materials ($\text{Li}_6\text{BaLa}_2\text{Ta}_2\text{O}_{12}$, $\text{Li}_7\text{La}_3\text{Zr}_2\text{O}_{12}:\text{Ga}_2\text{O}_3$, $\text{Li}_{6.5}\text{La}_3\text{Zr}_{1.5}\text{Ta}_{0.5}\text{O}_{12}:\text{Al}_2\text{O}_3$, $\text{Li}_{7-x}\text{La}_3\text{Zr}_{2-x}\text{Ta}_x\text{O}_{12}$ for $x = 0.5, 1.0$ and 1.5) were synthesized by high temperature solid state processing. The garnet-type structure was verified by x-ray diffraction. Among those different garnet-type bulk materials special attention was given to $\text{Li}_6\text{BaLa}_2\text{Ta}_2\text{O}_{12}$ which showed a total conductivity of about $\sigma = 5.8 \cdot 10^{-5} \text{ S}\cdot\text{cm}^{-1}$ at room temperature with an activation energy of $E_a = 0.45 \text{ eV}$. The electronic partial conductivity of the material was determined by Hebb-Wagner polarization measurements to be between $\sigma = 3.1 \cdot 10^{-13} \text{ S}\cdot\text{cm}^{-1}$ and $\sigma = 3.7 \cdot 10^{-10} \text{ S}\cdot\text{cm}^{-1}$ in the voltage range from 2.85 V to 4.3 V. This leads to an electronic transference number in a range from $t_{el} = 5.34 \cdot 10^{-9}$ to $6.4 \cdot 10^{-6}$. Hence, the transference number for lithium ions is nearly unity. The proposed defect formation (cf. Eq. 5.6) for the $\text{Li}_6\text{BaLa}_2\text{Ta}_2\text{O}_{12}$ garnet-type material leads to the conclusion that at higher polarization potentials mainly electron holes contribute to the electronic current. As Ba, La and Ta are present in their highest oxidation states, these holes will be formed in the O2p band.

By ablation of the respective garnet-type bulk materials via pulsed laser deposition each garnet-type material could be prepared as thin film. However, only $\text{Li}_6\text{BaLa}_2\text{Ta}_2\text{O}_{12}$, $\text{Li}_{6.5}\text{La}_3\text{Zr}_{1.5}\text{Ta}_{0.5}\text{O}_{12}:\text{Al}_2\text{O}_3$ and $\text{Li}_7\text{La}_3\text{Zr}_2\text{O}_{12}:\text{Ga}_2\text{O}_3$ garnet-type thin films were phase pure. The origin of the phase impurities in the $\text{Li}_{7-x}\text{La}_3\text{Zr}_{2-x}\text{Ta}_x\text{O}_{12}$ ($x = 0.5, 1.0$ and 1.5) thin films is not entirely clear. It seems that garnet-type thin films in general need a higher amount of stabilization than the respective bulk material. The stabilization of the garnet-type thin film structure can either be achieved by addition of Al_2O_3 or Ga_2O_3 or by a reduced Zr content, thereby raising the Ta content. For this reason $\text{Li}_6\text{BaLa}_2\text{Ta}_2\text{O}_{12}$, $\text{Li}_{6.5}\text{La}_3\text{Zr}_{1.5}\text{Ta}_{0.5}\text{O}_{12}:\text{Al}_2\text{O}_3$ and $\text{Li}_7\text{La}_3\text{Zr}_2\text{O}_{12}:\text{Ga}_2\text{O}_3$ garnet-type thin films were studied more intensively in this thesis. Of the deposited garnet-type single layer thin films the measured in lateral geometry lowest total conductivity was observed for $\text{Li}_7\text{La}_3\text{Zr}_2\text{O}_{12}:\text{Ga}_2\text{O}_3$ ($\sigma_{\text{lat}} = 1.2 \cdot 10^{-6} \text{ S}\cdot\text{cm}^{-1}$) whereas the highest total conductivity was observed for $\text{Li}_{6.5}\text{La}_3\text{Zr}_{1.5}\text{Ta}_{0.5}\text{O}_{12}:\text{Al}_2\text{O}_3$ ($\sigma_{\text{lat}} = 2.9 \cdot 10^{-6} \text{ S}\cdot\text{cm}^{-1}$). The $\text{Li}_6\text{BaLa}_2\text{Ta}_2\text{O}_{12}$ garnet-type thin films showed an intermediate total conductivity of $\sigma_{\text{lat}} = 1.7 \cdot 10^{-6} \text{ S}\cdot\text{cm}^{-1}$ and an activation energy of $E_a = 0.48 \text{ eV}$. The conductivities were determined by electrochemical impedance spectroscopy in lateral geometry and are comparable to the

conductivity of “LiPON”. Hebb-Wagner polarization experiments could not be performed in lateral geometry as the measured currents were too low. However, in situ dc polarization within a SEM in lateral geometry using a lithium counter electrode and a platinum microelectrode visually proved the ion conductivity of the garnet-type thin films. A significant influence of the substrate and of the thin film microstructure on the conductivity of the prepared garnet-type thin films was observed. In case of a MgO(100) single crystal substrate the garnet-type thin films were free of cracks, in contrast to garnet-type material deposited on ITO or on platinum coated MgO(100) substrates. Cracks appeared due to unmatched thermal expansion coefficients during cooling from $\vartheta \approx 550\text{ }^{\circ}\text{C}$ after the thin film deposition. Furthermore, TEM experiments revealed that droplets can also be a source of short circuits, because a subsequent ablated material can be deposited between the droplet and the surrounding thin film as the subsequent material is often deposited at another temperature.

A successful strategy to avoid short circuits is the deposition of multiple garnet-type layers as demonstrated with $\text{Li}_6\text{BaLa}_2\text{Ta}_2\text{O}_{12}$ on a platinum coated MgO(100) substrate. Therefore, the substrate was cooled after the first $\text{Li}_6\text{BaLa}_2\text{Ta}_2\text{O}_{12}$ layer was deposited until a temperature of $50\text{ }^{\circ}\text{C}$ was reached. This was followed by a repetition of the deposition process: Heating, deposition and cooling, until four subsequently deposited $\text{Li}_6\text{BaLa}_2\text{Ta}_2\text{O}_{12}$ layers were achieved. Thereby, already formed cracks in the previous garnet-type thin film were filled by the following garnet-type layer. Temperature dependent electrochemical impedance measurements revealed a total conductivity of $\sigma_{\text{axial}} = 3.3 \cdot 10^{-5}\text{ S}\cdot\text{cm}^{-1}$ at room temperature for $\text{Li}_6\text{BaLa}_2\text{Ta}_2\text{O}_{12}$ measured in an axial geometry between a large platinum counter electrode and a circular gold electrode.

The determined total conductivity in axial geometry across the thin film is in accordance with the total conductivity of the bulk material. By comparing the conductivity of the $\text{Li}_6\text{BaLa}_2\text{Ta}_2\text{O}_{12}$ thin films in lateral and axial geometry the influence of the thin film microstructure is revealed. The anisotropic conductivity behavior of garnet-type thin films is most likely caused by a columnar microstructure. Columnar growth appears to form grain boundaries with high impedance perpendicular to the substrate. Thereby, the grain boundaries have a bigger influence on conductivity measurements performed in lateral geometry than on conductivity measurements performed in axial geometry as long as the film is formed by long columns perpendicular to the substrate. However, the conductivity

model introduced in chapter 5.2.6 needs further verification by high resolution TEM measurements. The activation energy of the conductivity was determined to be $E_a = 0.5$ eV in axial geometry which is comparable to the activation energies determined in lateral geometry ($E_a = 0.48$ eV). For the conductivity measurements in axial geometry a self-made measurement setup with 26 circular electrodes ($\varnothing = 0.9$ mm) and a Peltier element was constructed.

The electronic conductivity was determined to $\sigma_{el} = 3.6 \cdot 10^{-11}$ S·cm⁻¹ at $U = 0.2$ V in lateral geometry by dc polarization using two blocking electrodes (platinum and gold) and had its maximum at a polarization potential of $U = 3.8$ V with an electronic conductivity of $\sigma_{el} = 4 \cdot 10^{-11}$ S·cm⁻¹. A further increase of the applied potential caused a material decomposition as a consequence the current was decreased. The resulting electronic conductivity was $\sigma_{el} = 2.6 \cdot 10^{-11}$ S·cm⁻¹ at $U = 5$ V.

By depositing garnet-type multilayer structures with two different, alternating garnet-type materials the columnar growth was interrupted and the substrate quality was increased by improved lattice matching with each subsequent layer. A (Li₆BaLa₂Ta₂O₁₂|Li_{6.5}La₃Zr_{1.5}Ta_{0.5}:Al₂O₃)×5 garnet type thin film prepared at 600 °C showed a lateral conductivity of $\sigma_{lat} = 7.7 \cdot 10^{-6}$ S·cm⁻¹ which indicates an increase compared to the conductivity of the garnet-type single layers. This increase in conductivity was also observed for a deposition of four alternating garnet-type layers with a total film thickness of $d \approx 400$ nm, followed by an additional layer of Li_{6.5}La₃Zr_{1.5}Ta_{0.5}:Al₂O₃ with a thickness of $d \approx 2300$ nm. Therefore, the last layer determines the conductivity. The measured lateral conductivity of this thin film was $\sigma_{lat} = 7.2 \cdot 10^{-6}$ S·cm⁻¹, which is in accordance with the conductivity of a (Li₆BaLa₂Ta₂O₁₂|Li_{6.5}La₃Zr_{1.5}Ta_{0.5}:Al₂O₃)×5 garnet-type multilayer thin film.

In order to investigate the influence of layer thickness on the total conductivity, (Li_{6.5}La₃Zr_{1.5}Ta_{0.5}:Al₂O₃|Li₇La₃Zr₂O₁₂:Ga₂O₃)×5 thin films with a constant number of five bilayers were prepared at 600 °C by pulsed laser deposition. The highest lateral conductivity of $\sigma_{lat}(220 \text{ nm/layer}) = 7.3 \cdot 10^{-6}$ S·cm⁻¹ was achieved for a single layer thickness of ≈ 220 nm and decreased for approximately 160 nm per layer ($\sigma_{lat}(160 \text{ nm/layer}) = 6.2 \cdot 10^{-6}$ S·cm⁻¹) to a value comparable to that of a single layer ($\sigma_{lat}(\text{single layer}) = 1.7 \cdot 10^{-6}$ S·cm⁻¹) thin film at ≈ 140 nm per layer

($\sigma_{\text{lat}}(140 \text{ nm/layer}) = 2.6 \cdot 10^{-6} \text{ S} \cdot \text{cm}^{-1}$). This decrease in conductivity with decreasing layer thickness showed that the interfaces between the two different garnet-type materials have a higher resistance than the “bulk” of the thin film. Hence, thin film interfaces are in general not desirable due to the additional resistance generated at the interface, but the resulting lattice relaxation and the less distinctive columnar growth superimpose this effect if the density of interfaces is kept low.

The highest lateral conductivity of $\sigma_{\text{lat}} = 2.9 \cdot 10^{-5} \text{ S} \cdot \text{cm}^{-1}$ was observed for a $(\text{Li}_{6.5}\text{La}_3\text{Zr}_{1.5}\text{Ta}_{0.5}:\text{Al}_2\text{O}_3|\text{Li}_7\text{La}_3\text{Zr}_2\text{O}_{12}:\text{Ga}_2\text{O}_3) \times 5$ multilayer structure deposited at 620 °C. This conductivity is comparable to that of an axially measured $\text{Li}_6\text{BaLa}_2\text{Ta}_2\text{O}_{12}$ garnet-type thin film showing that multilayer structures can overcome the anisotropic conductivity of garnet-type thin films. Transmission electron microscopy of multilayer structures revealed that the multilayer thin films possess smooth interfaces between the different garnet-type phases and that the single layers show a columnar growth.

An overview of the determined conductivities for the different garnet-type thin films is displayed by means of an Arrhenius plot in Figure 43. Depicted are the lateral conductivities of $\text{Li}_6\text{BaLa}_2\text{Ta}_2\text{O}_{12}$ (LBLTO) and of a $(\text{Li}_{6.5}\text{La}_3\text{Zr}_{1.5}\text{Ta}_{0.5}:\text{Al}_2\text{O}_3|\text{Li}_7\text{La}_3\text{Zr}_2\text{O}_{12}:\text{Ga}_2\text{O}_3) \times 5$ ((LLZTO|LLZGO) $\times 5$) multilayer structure prepared at 620 °C. The filled area between the Arrhenius plots of those two garnet-type thin films indicates the conductivity region of the different garnet-type multilayer structures. Furthermore, the conductivity measurement of $\text{Li}_6\text{BaLa}_2\text{Ta}_2\text{O}_{12}$ in axial geometry is shown. The temperature dependent conductivity data of $\text{Li}_6\text{BaLa}_2\text{Ta}_2\text{O}_{12}$ and $(\text{Li}_{6.5}\text{La}_3\text{Zr}_{1.5}\text{Ta}_{0.5}:\text{Al}_2\text{O}_3|\text{Li}_7\text{La}_3\text{Zr}_2\text{O}_{12}:\text{Ga}_2\text{O}_3) \times 5$ garnet-type thin films is shown in the context of other lithium ion conducting thin films taken from literature (the respective reference is stated in the figure and is also displayed in Table 1).

Possible applications for lithium ion conducting thin films besides the use in all solid state batteries are their utilization as protective coatings. It was proven that $\text{Li}_6\text{BaLa}_2\text{Ta}_2\text{O}_{12}$ thin films are able to prevent the reduction of materials that are chemically not stable versus metallic lithium, as shown for an Ohara electrolyte (cf. chapter 5.2.7). Besides the protection of another electrolyte material the coating of electrode materials could also be a possible field of application. Therefore, a bulk pellet of $\text{Li}_4\text{Ti}_5\text{O}_{12}$ was covered with a garnet-type thin film. The deposited thin film was able to cover smaller pores on top of the ceramic $\text{Li}_4\text{Ti}_5\text{O}_{12}$ pellet.

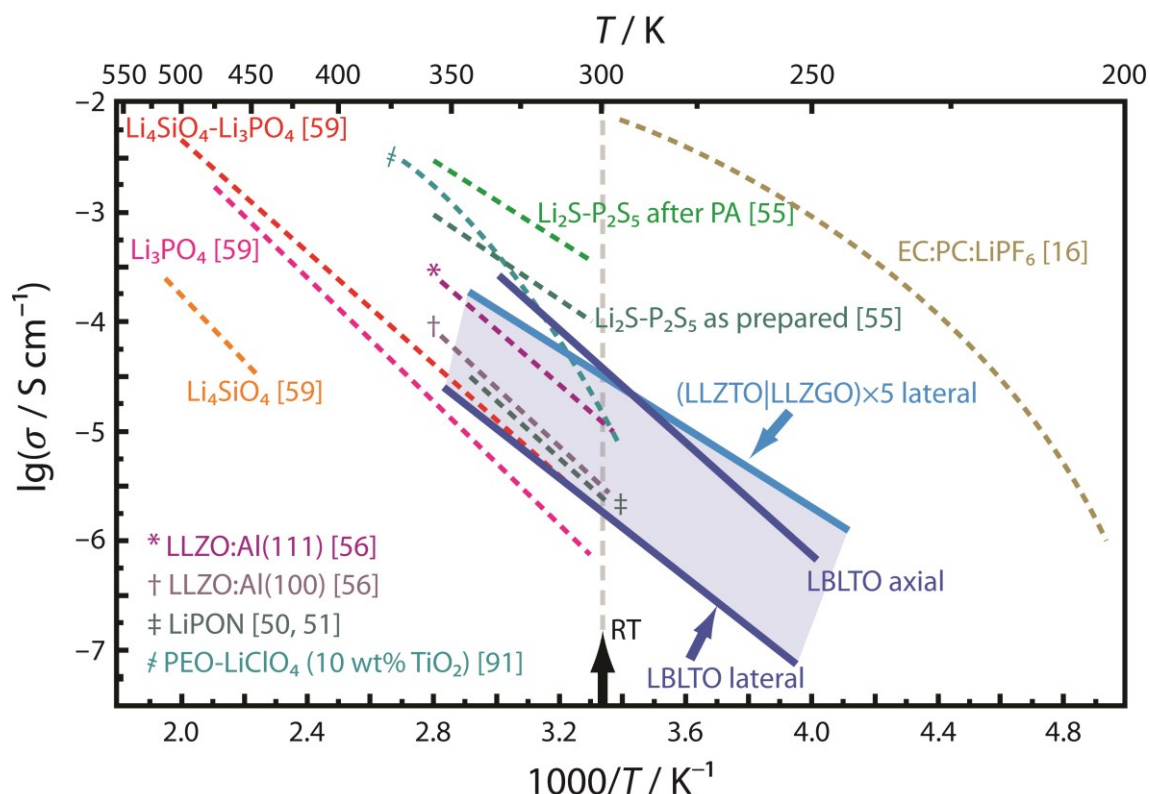


Figure 43: Survey of lithium ion conducting thin films by means of an Arrhenius plot. Own measurements are represented by solid lines. The filled area indicates the conductivity region of the different garnet-type multilayer structures. Reference data taken from literature is shown as dotted lines. PA stands for post anneal.

Encouraged by these results, $\text{Li}_6\text{BaLa}_2\text{Ta}_2\text{O}_{12}$ garnet-type thin films were deposited onto porous anodized aluminum oxide substrates. Pores with a diameter of 100 nm were successfully sealed. Hereby, lithium ion-selective membranes were constructed. Dye concentration experiments proved that the membranes were impermeable for 2-propanol and methyl red in ethanol. A subsequent employment in Li-S cells showed that the resistance of the cell was increased compared to a cell without an ion-selective membrane. This effect led to low specific capacities caused by fast reached voltage limits during discharge and charge. However, the coulombic efficiency was raised compared to a reference Li-S cell from around 35 % to 98 % in the first cycles. Thereby, ion-selective membranes could help to establish next generation cells. Furthermore, the utilization of ion-selective membranes in hybrid cells would enable high cell capacities by the use of standard electrodes coupled with a liquid electrolyte system. Shuttle mechanisms of undesired redox active species could be suppressed by the ion selectivity of the

membrane. In addition to that, different liquid electrolytes could be applied in two mechanically separated electrode compartments. This could then lead to improved cell characteristics as the liquid electrolyte can be adjusted suiting one particular electrode material and does not have to be a compromise for both electrode materials.

Another application of ion-selective membranes could be waste recycling. This would be especially beneficial for the recovery of lithium from used batteries. Here, lithium ions could be separated from a solution or from a melt, as these membranes are temperature stable up to 500 °C.

However, lithium ion conducting garnet-type thin films have several severe disadvantages. One main disadvantage is the preparation by pulsed laser deposition. It is not possible to cover big areas with this technique and the deposition is challenging as well as expensive. Additionally, the substrate needs to be stable during the deposition ($T > 500\text{ °C}$ in a $5 \cdot 10^{-2}$ mbar O_2 atmosphere) and one has to take into account that the substrate might have a big influence on the conductivity. Furthermore, the preparation of crack free garnet-type thin films is demanding, but by deposition of multiple garnet-type layers crack formation can be overcome. In general solid electrolyte thin films should be free of cracks and droplets, whereby both requests are difficult to achieve by pulsed laser deposition. An ideal lithium ion conducting thin film, in addition to the characteristics stated in chapters 3.1 and 3.2, needs to be processed easily, e.g., by sputter deposition at room temperature on flexible substrates for roll to roll processing. Thus, a commercial application of garnet-type thin films seems unlikely at this time and further research would be necessary.

So far, “LiPON” is the only commercially used lithium ion conducting thin film, and a replacement by a thin film material with higher ion conductivities is desirable. A successor will probably be either an amorphous or a glass ceramic, as these materials can often be deposited at room temperature, possibly by sputter deposition, and the stoichiometry does not have to be satisfied as for crystalline materials.

The most likely application of garnet-type materials, as long as sputter deposition is not successful, would be as bulk electrolyte for all solid state thick film batteries, since the garnet-type phases are stable versus metallic lithium and combine good lithium ion conductivity with a low electronic conductivity.

7. References

- [1] X. Ji, and L. F. Nazar, "Advances in Li-S batteries," *Journal of Materials Chemistry*, vol. 20, pp. 9821-9826, 2010.
- [2] Y. V. Mikhaylik, and J. R. Akridge, "Polysulfide shuttle study in the Li/S battery system," *Journal of the Electrochemical Society*, vol. 151, pp. A1969-A1976, 2004.
- [3] P. Knauth, "Inorganic solid Li ion conductors: An overview," *Solid State Ionics*, vol. 180, pp. 911-916, 2009.
- [4] A. Patil, V. Patil, D. W. Shin *et al.*, "Issue and challenges facing rechargeable thin film lithium batteries," *Materials Research Bulletin*, vol. 43, pp. 1913-1942, 2008.
- [5] P. G. Bruce, S. A. Freunberger, L. J. Hardwick *et al.*, "Li-O₂ and Li-S batteries with high energy storage," *Nature Materials*, vol. 11, pp. 19-29, 2012.
- [6] M. Z. A. Munshi, "Handbook of Solid State Batteries & Capacitors," World Scientific Publishing Co. Pte Ltd, 1995.
- [7] C. A. C. Sequeira, and A. E. Hooper, "Solid State Batteries," Springer, 1985.
- [8] T. Minami, M. Tatsumisago, M. Wakihara *et al.*, *Solid State Ionics for Batteries*, Tokyo: Springer, 2005.
- [9] H. Buschmann, J. Dolle, S. Berendts *et al.*, "Structure and dynamics of the fast lithium ion conductor "Li₇La₃Zr₂O₁₂", " *Physical Chemistry Chemical Physics*, vol. 13, pp. 19378-19392, 2011.
- [10] C. Galven, J. L. Fourquet, M. P. Crosnier-Lopez *et al.*, "Instability of the lithium garnet Li₇La₃Sn₂O₁₂: Li⁺/H⁺ exchange and structural study," *Chemistry of Materials*, vol. 23, pp. 1892-1900, 2011.
- [11] C. Galven, J. Dittmer, E. Suard *et al.*, "Instability of lithium garnets against moisture. Structural characterization and dynamics of Li_{7-x}H_xLa₃Sn₂O₁₂ and Li_{5-x}H_xLa₃Nb₂O₁₂," *Chemistry of Materials*, vol. 24, pp. 3335-3345, 2012.
- [12] L. Truong, M. Howard, O. Clemens *et al.*, "Facile proton conduction in H⁺/Li⁺ ion-exchanged garnet-type fast Li-ion conducting Li₅La₃Nb₂O₁₂," *Journal of Materials Chemistry A*, vol. 1, pp. 13469-13475, 2013.
- [13] G. Larraz, A. Orera, and M. L. Sanjuan, "Cubic phases of garnet-type Li₇La₃Zr₂O₁₂: the role of hydration," *Journal of Materials Chemistry A*, vol. 1, pp. 11419-11428, 2013.
- [14] G. Y. Adachi, N. Imanaka, and H. Aono, "Fast Li-circle plus conducting ceramic electrolytes," *Advanced Materials*, vol. 8, pp. 127-135, 1996.

-
- [15] J. B. Goodenough, and Y. Kim, "Challenges for Rechargeable Li Batteries," *Chemistry of Materials*, vol. 22, pp. 587-603, 2010.
- [16] P. E. Stallworth, J. J. Fontanella, M. C. Wintersgill *et al.*, "NMR, DSC and high pressure electrical conductivity studies of liquid and hybrid electrolytes," *Journal of Power Sources*, vol. 81, pp. 739-747, 1999.
- [17] S. Zugmann, M. Fleischmann, M. Amereller *et al.*, "Measurement of transference numbers for lithium ion electrolytes via four different methods, a comparative study," *Electrochimica Acta*, vol. 56, pp. 3926-3933, 2011.
- [18] V. Thangadurai, H. Kaack, and W. J. F. Weppner, "Novel fast lithium ion conduction in garnet-type $\text{Li}_5\text{La}_3\text{M}_2\text{O}_{12}$ ($\text{M} = \text{Nb}, \text{Ta}$)," *Journal of the American Ceramic Society*, vol. 86, pp. 437-440, 2003.
- [19] V. Thangadurai, S. Narayanan, and D. Pinzaru, "Garnet-type solid-state fast Li ion conductors for Li batteries: critical review," *Chemical Society Reviews*, 2014.
- [20] V. Thangadurai, J. Schwenzel, and W. Weppner, "Tailoring ceramics for specific applications: A case study of the development of all-solid-state lithium batteries," *Ionics*, vol. 11, pp. 11-23, 2005.
- [21] J. A. Alonso, J. Sanz, J. Santamaria *et al.*, "On the location of Li^+ cations in the fast Li-cation conductor $\text{La}_{0.5}\text{Li}_{0.5}\text{TiO}_3$ perovskite," *Angewandte Chemie-International Edition*, vol. 39, pp. 619-621, 2000.
- [22] H. Geng, J. Lan, A. Mel *et al.*, "Effect of sintering temperature on microstructure and transport properties of $\text{Li}_{3x}\text{La}_{2/3-x}\text{TiO}_3$ with different lithium contents," *Electrochimica Acta*, vol. 56, pp. 3406-3414, 2011.
- [23] O. Bohnke, "The fast lithium-ion conducting oxides $\text{Li}_{3x}\text{La}_{2/3-x}\text{TiO}_3$ from fundamentals to application," *Solid State Ionics*, vol. 179, pp. 9-15, 2008.
- [24] S. Stramare, V. Thangadurai, and W. Weppner, "Lithium lanthanum titanates: A review," *Chemistry of Materials*, vol. 15, pp. 3974-3990, 2003.
- [25] L. O. Hagman, and Kierkega.P, "The Crystal Structure of $\text{NaM}_2^{\text{IV}}(\text{PO}_4)_3$; $\text{Me}^{\text{IV}} = \text{Ge}, \text{Ti}, \text{Zr}$," *Acta Chemica Scandinavica*, vol. 22, pp. 1822-1832, 1968, 1968.
- [26] H. Aono, E. Sugimoto, Y. Sadaoka *et al.*, "Ionic conductivity of the lithium titanium phosphate $(\text{Li}_{1+x}\text{Al}_x\text{Ti}_{2-x}(\text{PO}_4)_3)$, $(\text{Li}_{1+x}\text{Sc}_x\text{Ti}_{2-x}(\text{PO}_4)_3)$, $(\text{Li}_{1+x}\text{Y}_x\text{Ti}_{2-x}(\text{PO}_4)_3)$, $(\text{Li}_{1+x}\text{La}_x\text{Ti}_{2-x}(\text{PO}_4)_3)$ systems," *Journal of the Electrochemical Society*, vol. 136, pp. 590-591, 1989.
- [27] P. Hartmann, T. Leichtweiss, M. R. Busche *et al.*, "Degradation of NASICON-type materials in contact with lithium metal: Formation of mixed conducting interphases (MCI) on solid electrolytes," *Journal of Physical Chemistry C*, vol. 117, pp. 21064-21074, 2013.

- [28] H. Y. P. Hong, "Crystal-structure and ionic-conductivity of $\text{Li}_{14}\text{Zn}(\text{GeO}_4)_4$ and other new Li^+ superionic conductors," *Materials Research Bulletin*, vol. 13, pp. 117-124, 1978.
- [29] P. G. Bruce, and A. R. West, "Ionic-conductivity of LISICON solid-solutions, $\text{Li}_{2+2x}\text{Zn}_{1-x}\text{GeO}_4$," *Journal of Solid State Chemistry*, vol. 44, pp. 354-365, 1982.
- [30] R. Kanno, T. Hata, Y. Kawamoto *et al.*, "Synthesis of a new lithium ionic conductor, thio-LISICON-lithium germanium sulfide system," *Solid State Ionics*, vol. 130, pp. 97-104, 2000.
- [31] M. Murayama, R. Kanno, M. Irie *et al.*, "Synthesis of new lithium ionic conductor thio-LISICON - Lithium silicon sulfides system," *Journal of Solid State Chemistry*, vol. 168, pp. 140-148, 2002.
- [32] M. Murayama, N. Sonoyama, A. Yamada *et al.*, "Material design of new lithium ionic conductor, thio-LISICON, in the $\text{Li}_2\text{S-P}_2\text{S}_5$ system," *Solid State Ionics*, vol. 170, pp. 173-180, 2004.
- [33] U. V. Alpen, A. Rabenau, and G. H. Talat, "Ionic-conductivity in Li_3N single-crystals," *Applied Physics Letters*, vol. 30, pp. 621-623, 1977.
- [34] B. A. Boukamp, and R. A. Huggins, "Fast ionic conductivity in lithium nitride," *Materials Research Bulletin*, vol. 13, pp. 23-32, 1978.
- [35] A. Rabenau, "Lithium nitride and related materials - Case-study of the use of modern solid-state research techniques," *Solid State Ionics*, vol. 6, pp. 277-293, 1982, 1982.
- [36] M. Ribes, B. Barrau, and J. L. Souquet, "Sulfide glasses - Glass forming region, structure and ionic-conduction of glasses in $\text{Na}_2\text{S-SiS}_2$, $\text{Na}_2\text{S-P}_2\text{S}_5$ and $\text{Li}_2\text{S-GeS}_2$ Systems," *Journal of Non-Crystalline Solids*, vol. 38-9, pp. 271-276, 1980.
- [37] T. Minami, A. Hayashi, and M. Tatsumisago, "Recent progress of glass and glass-ceramics as solid electrolytes for lithium secondary batteries," *Solid State Ionics*, vol. 177, pp. 2715-2720, 2006.
- [38] H. Muramatsu, A. Hayashi, T. Ohtomo *et al.*, "Structural change of $\text{Li}_2\text{S-P}_2\text{S}_5$ sulfide solid electrolytes in the atmosphere," *Solid State Ionics*, vol. 182, pp. 116-119, 2011.
- [39] H. Buschmann, S. Berendts, B. Mogwitz *et al.*, "Lithium metal electrode kinetics and ionic conductivity of the solid lithium ion conductors " $\text{Li}_7\text{La}_3\text{Zr}_2\text{O}_{12}$ " and $\text{Li}_{7-x}\text{La}_3\text{Zr}_{2-x}\text{Ta}_x\text{O}_{12}$ with garnet-type structure," *Journal of Power Sources*, vol. 206, pp. 236-244, 2012.
- [40] R. D. Shannon, and C. T. Prewitt, "Effective ionic radii in oxides and fluorides," *Acta Crystallographica Section B*, vol. 25, pp. 925-946, 1969.

-
- [41] H. El Shinawi, and J. Janek, "Stabilization of cubic lithium-stuffed garnets of the type $\text{Li}_7\text{La}_3\text{Zr}_2\text{O}_{12}$ " by addition of gallium," *Journal of Power Sources*, vol. 225, pp. 13-19, 2013.
- [42] J. L. Allen, J. Wolfenstine, E. Rangasamy *et al.*, "Effect of substitution (Ta, Al, Ga) on the conductivity of $\text{Li}_7\text{La}_3\text{Zr}_2\text{O}_{12}$," *Journal of Power Sources*, vol. 206, pp. 315-319, 2012.
- [43] V. Thangadurai, and W. Weppner, " $\text{Li}_6\text{ALa}_2\text{Nb}_2\text{O}_{12}$ (A = Ca, Sr, Ba): A new class of fast lithium ion conductors with garnet-like structure," *Journal of the American Ceramic Society*, vol. 88, pp. 411-418, 2005.
- [44] V. Thangadurai, and W. Weppner, " $\text{Li}_6\text{ALa}_2\text{Nb}_2\text{O}_{12}$ (A= Sr, Ba): Novel garnet-like oxides for fast lithium ion conduction," *Advanced Functional Materials*, vol. 15, pp. 107-112, 2005.
- [45] E. J. Cussen, "The structure of lithium garnets: cation disorder and clustering in a new family of fast Li^+ conductors," *Chemical Communications*, pp. 412-413, 2006.
- [46] M. P. O'Callaghan, and E. J. Cussen, "Lithium dimer formation in the Li-conducting garnets $\text{Li}_{5+x}\text{Ba}_x\text{La}_{3-x}\text{Ta}_2\text{O}_{12}$ ($0 < x \leq 1.6$)," *Chemical Communications*, pp. 2048-2050, 2007.
- [47] E. J. Cussen, "Structure and ionic conductivity in lithium garnets," *Journal of Materials Chemistry*, vol. 20, pp. 5167-5173, 2010.
- [48] A. Logéat, T. Köhler, U. Eisele *et al.*, "From order to disorder: The structure of lithium-conducting garnets $\text{Li}_{7-x}\text{La}_3\text{Ta}_x\text{Zr}_{2-x}\text{O}_{12}$ ($x=0-2$)," *Solid State Ionics*, vol. 206, pp. 33-38, 2012.
- [49] Y. Zhu, V. Thangadurai, and W. Weppner, "Garnet-like solid state electrolyte $\text{Li}_6\text{BaLa}_2\text{Ta}_2\text{O}_{12}$ based potentiometric CO_2 gas sensor," *Sensors and Actuators B: Chemical*, vol. 176, pp. 284-289, 2013.
- [50] J. B. Bates, N. J. Dudney, G. R. Gruzalski *et al.*, "Electrical properties of amorphous lithium electrolyte thin films," *Solid State Ionics*, vol. 53, pp. 647-654, 1992.
- [51] X. H. Yu, J. B. Bates, G. E. Jellison *et al.*, "A stable thin-film lithium electrolyte: Lithium phosphorus oxynitride," *Journal of the Electrochemical Society*, vol. 144, pp. 524-532, 1997.
- [52] J. B. Bates, N. J. Dudney, B. Neudecker *et al.*, "Thin-film lithium and lithium-ion batteries," *Solid State Ionics*, vol. 135, pp. 33-45, 2000.
- [53] B. J. Neudecker, N. J. Dudney, and J. B. Bates, "'Lithium-free" thin-film battery with in situ plated Li anode," *Journal of the Electrochemical Society*, vol. 147, pp. 517-523, 2000.

-
- [54] K. H. Joo, H. J. Sohn, P. Vinatier *et al.*, "Lithium ion conducting lithium sulfur oxynitride thin film," *Electrochemical and Solid State Letters*, vol. 7, pp. A256-A258, 2004.
- [55] A. Sakuda, A. Hayashi, S. Hama *et al.*, "Preparation of highly lithium-ion conductive $80\text{Li}_2\text{S} \cdot 20\text{P}_2\text{S}_5$ thin-film electrolytes using pulsed laser deposition," *Journal of the American Ceramic Society*, vol. 93, pp. 765-768, 2010.
- [56] S. Kim, M. Hirayama, S. Taminato *et al.*, "Epitaxial growth and lithium ion conductivity of lithium-oxide garnet for an all solid-state battery electrolyte," *Dalton Transactions*, vol. 42, no. 36, pp. 13112-13117, 2013.
- [57] D. J. Kalita, S. H. Lee, K. S. Lee *et al.*, "Ionic conductivity properties of amorphous Li-La-Zr-O solid electrolyte for thin film batteries," *Solid State Ionics*, vol. 229, pp. 14-19, 2012.
- [58] J. Tan, and A. Tiwari, "Fabrication and Characterization of $\text{Li}_7\text{La}_3\text{Zr}_2\text{O}_{12}$ Thin Films for Lithium Ion Battery," *ECS Solid State Letters*, vol. 1, pp. Q57-Q60, 2012.
- [59] Y. Sakurai, A. Sakuda, A. Hayashi *et al.*, "Preparation of amorphous Li_4SiO_4 - Li_3PO_4 thin films by pulsed laser deposition for all-solid-state lithium secondary batteries," *Solid State Ionics*, vol. 182, pp. 59-63, 2011.
- [60] J. B. Bates, N. J. Dudney, B. J. Neudecker *et al.*, "Preferred orientation of polycrystalline LiCoO_2 films," *Journal of The Electrochemical Society*, vol. 147, pp. 59-70, 2000.
- [61] S. D. Jones, J. R. Akridge, and F. K. Shokoohi, "Thin-film rechargeable Li batteries," *Solid State Ionics*, vol. 69, pp. 357-368, 1994.
- [62] E. Jeong, C. Hong, Y. Tak *et al.*, "Investigation of interfacial resistance between LiCoO_2 cathode and LiPON electrolyte in the thin film battery," *Journal of Power Sources*, vol. 159, pp. 223-226, 2006.
- [63] J. Schwenzel, V. Thangadurai, and W. Weppner, "Developments of high-voltage all-solid-state thin-film lithium ion batteries," *Journal of Power Sources*, vol. 154, pp. 232-238, 2006.
- [64] J. Schwenzel, V. Thangadurai, and W. Weppner, "Investigation of thin film all-solid-state lithium ion battery materials," *Ionics*, vol. 9, pp. 348-356, 2003.
- [65] Y. Hamon, A. Douard, F. Sabary *et al.*, "Influence of sputtering conditions on ionic conductivity of LiPON thin films," *Solid State Ionics*, vol. 177, pp. 257-261, 2006.
- [66] B. Fleutot, B. Pecquenard, H. Martinez *et al.*, "Investigation of the local structure of LiPON thin films to better understand the role of nitrogen on their performance," *Solid State Ionics*, vol. 186, pp. 29-36, 2011.

-
- [67] N. Suzuki, T. Inaba, and T. Shiga, "Electrochemical properties of LiPON films made from a mixed powder target of Li_3PO_4 and Li_2O ," *Thin Solid Films*, vol. 520, pp. 1821-1825, 2012.
- [68] L. Le Van-Jodin, F. Ducroquet, F. Sabary *et al.*, "Dielectric properties, conductivity and Li^+ ion motion in LiPON thin films," *Solid State Ionics*, vol. 253, pp. 151-156, 2013.
- [69] N. Mascaraque, J. L. G. Fierro, A. Durán *et al.*, "An interpretation for the increase of ionic conductivity by nitrogen incorporation in LiPON oxynitride glasses," *Solid State Ionics*, , pp. 73-79, 2013.
- [70] K. Kanehori, K. Matsumoto, K. Miyauchi *et al.*, "Thin-film solid electrolyte and its application to secondary lithium cell," *Solid State Ionics*, pp. 1445-1448, 1983.
- [71] M. Baba, N. Kumagai, H. Kobayashi *et al.*, "Fabrication and electrochemical characteristics of all- solid-state lithium-ion batteries using V_2O_5 thin films for both electrodes," *Electrochemical and Solid State Letters*, vol. 2, pp. 320-322, 1999.
- [72] H. Ohtsuka, S. Okada, and J. Yamaki, "Solid-State Battery with Li_2O - V_2O_5 - SiO_2 Solid Electrolyte Thin-Film," *Solid State Ionics*, vol. 40-1, pp. 964-966, 1990.
- [73] N. J. Dudney, J. B. Bates, R. A. Zuhr *et al.*, "Nanocrystalline $\text{Li}_x\text{Mn}_{2-y}\text{O}_4$ cathodes for solid-state thin-film rechargeable lithium batteries," *Journal of the Electrochemical Society*, vol. 146, pp. 2455-2464, 1999.
- [74] B. Wang, J. B. Bates, F. X. Hart *et al.*, "Characterization of thin-film rechargeable lithium batteries with lithium cobalt oxide cathodes," *Journal of the Electrochemical Society*, vol. 143, pp. 3203-3213, 1996.
- [75] B. J. Neudecker, R. A. Zuhr, J. D. Robertson *et al.*, "Lithium manganese nickel oxides $\text{Li}_x(\text{Mn}_y\text{Ni}_{1-y})_{2-x}\text{O}_2$ - II. Electrochemical studies on thin-film batteries," *Journal of the Electrochemical Society*, vol. 145, pp. 4160-4168, 1998.
- [76] N. Kuwata, J. Kawamura, K. Toribami *et al.*, "Thin-film lithium-ion battery with amorphous solid electrolyte fabricated by pulsed laser deposition," *Electrochemistry Communications*, vol. 6, pp. 417-421, 2004.
- [77] M. Ogawa, R. Kanda, K. Yoshida *et al.*, "High-capacity thin film lithium batteries with sulfide solid electrolytes," *Journal of Power Sources*, vol. 205, pp. 487-490, 2012.
- [78] H. Rickert, and C. D. O'Brian, "Elektroschemische Untersuchungen über den Durchtritt von Silber durch die Phasengranze festes Silber/festes Silbersulfid bei höheren Temperaturen," *Zeitschrift für Physikalische Chemie Neue Folge*, pp. 71-86, 1962.
- [79] H. Rickert, and C. Wagner, "Zur Kinetik der Sulfidierung von Silber, " *Zeitschrift für Physikalische Chemie Neue Folge*, pp. 32-39, 1962.

-
- [80] M. Meyer, H. Rickert, and U. Schwaitzer, "Investigations on the kinetics of the anodic dissolution of lithium at the interface Li/Li₃N," *Solid State Ionics*, vol. 9–10, pp. 689-693, 1983.
- [81] J. Janek, and S. Majoni, "Investigation of charge transport across the Ag|AgI-interface: (I) Occurrence of periodic phenomena during anodic dissolution of silver," *Berichte der Bunsengesellschaft für physikalische Chemie*, vol. 99, pp. 14-20, 1995.
- [82] J. Janek, and S. Majoni, "Investigation of charge transport across The Ag|AgI-interface 1. occurrence of periodic phenomena during anodic-dissolution of silver," *Berichte Der Bunsen-Gesellschaft-Physical Chemistry Chemical Physics*, vol. 99, pp. 14-20, 1995.
- [83] S. Majoni, and J. Janek, "Periodic electrochemical oscillations at a solid-solid electrode," *Solid State Ionics*, vol. 85, pp. 247-250, 1996.
- [84] J. Janek, "Zum Ladungsdurchtritt an Phasengrenzen in Festkörpern," Habilitationsschrift, Hannover, 1997.
- [85] S. Majoni, and J. Janek, "Investigation of charge transport across the Ag/AgI-interface: (II) - Dilatometric study of the anodic dissolution of silver," *Berichte Der Bunsen-Gesellschaft-Physical Chemistry Chemical Physics*, vol. 102, pp. 756-762, 1998.
- [86] J. Corish, and C. D. O'Briain, "The growth and dissolution of silver whiskers," *Journal of Crystal Growth*, vol. 13–14, pp. 62-67, 1972.
- [87] M. Tatsumisago, and A. Hayashi, "Superionic glasses and glass–ceramics in the Li₂S–P₂S₅ system for all-solid-state lithium secondary batteries," *Solid State Ionics*, vol. 225, pp. 342-345, 2012.
- [88] M. Nagao, A. Hayashi, and M. Tatsumisago, "Bulk-type lithium metal secondary battery with indium thin layer at interface between Li electrode and Li₂S–P₂S₅ solid electrolyte," *Electrochemistry*, vol. 80, pp. 734-736, 2012.
- [89] A. Sakuda, A. Hayashi, T. Ohtomo *et al.*, "Bulk-type all-solid-state lithium secondary battery with Li₂S–P₂S₅ thin-film separator," *Electrochemistry*, vol. 80, pp. 839-841, 2012.
- [90] M. Kotobuki, K. Kanamura, Y. Sato *et al.*, "Fabrication of all-solid-state lithium battery with lithium metal anode using Al₂O₃-added Li₇La₃Zr₂O₁₂ solid electrolyte," *Journal of Power Sources*, vol. 196, pp. 7750-7754, 2011.
- [91] L. Edman, A. Ferry, and M. M. Doeff, "Slow recrystallization in the polymer electrolyte system poly(ethylene oxide)_n-LiN(CF₃SO₂)₂," *Journal of Materials Research*, vol. 15, pp. 1950-1954, 2000.

-
- [92] M. Kotobuki, Y. Suzuki, H. Munakata *et al.*, "Fabrication of three-dimensional battery using ceramicelectrolyte with honeycomb structure by sol-gel process," *Journal of the Electrochemical Society*, vol. 157, pp. A493-A498, 2010.
- [93] T. Matsuyama, A. Sakuda, A. Hayashi *et al.*, "Electrochemical properties of all-solid-state lithium batteries with amorphous titanium sulfide electrodes prepared by mechanical milling," *Journal of Solid State Electrochemistry*, vol. 17, pp. 2697-2701, 2013.
- [94] T. Ohtomo, A. Hayashi, M. Tatsumisago *et al.*, "All-solid-state batteries with Li_2O - Li_2S - P_2S_5 glass electrolytes synthesized by two-step mechanical milling," *Journal of Solid State Electrochemistry*, vol. 17, pp. 2551-2557, 2013.
- [95] T. Uemura, K. Goto, M. Ogawa *et al.*, "All-solid secondary batteries with sulfide-based thin film electrolytes," *Journal of Power Sources*, vol. 240, pp. 510-514, 2013.
- [96] M. Nagao, Y. Imade, H. Narisawa *et al.*, "All-solid-state Li-sulfur batteries with mesoporous electrode and thio-LISICON solid electrolyte," *Journal of Power Sources*, vol. 222, no. 0, pp. 237-242, 2013.
- [97] J. Kim, M. Eom, S. Noh *et al.*, "Effect of mixing method on the properties of composite cathodes for all-solid-state lithium batteries using Li_2S - P_2S_5 solid electrolytes," *Journal of Power Sources*, vol. 244, pp. 476-481, 2013.
- [98] S. Ohta, S. Komagata, J. Seki *et al.*, "All-solid-state lithium ion battery using garnet-type oxide and Li_3BO_3 solid electrolytes fabricated by screen-printing," *Journal of Power Sources*, vol. 238, pp. 53-56, 2013.
- [99] Y. Jin, and P. J. McGinn, " $\text{Li}_7\text{La}_3\text{Zr}_2\text{O}_{12}$ electrolyte stability in air and fabrication of a $\text{Li}/\text{Li}_7\text{La}_3\text{Zr}_2\text{O}_{12}/\text{Cu}_{0.1}\text{V}_2\text{O}_5$ solid-state battery," *Journal of Power Sources*, vol. 239, pp. 326-331, 2013.
- [100] M. R. Busche, P. Adelhelm, H. Sommer *et al.*, "Systematical electrochemical study on the parasitic shuttle-effect in lithium-sulfur-cells at different temperatures and different rates," *Journal of Power Sources*, vol. 259, pp. 289-299, 2014.
- [101] S. S. Zhang, "Liquid electrolyte lithium/sulfur battery: Fundamental chemistry, problems, and solutions," *Journal of Power Sources*, vol. 231, pp. 153-162, 2013.
- [102] A. Manthiram, Y. Fu, and Y.-S. Su, "Challenges and prospects of lithium-sulfur batteries," *Accounts of Chemical Research*, vol. 46, pp. 1125-1134, 2012.
- [103] M. R. Busche, T. Drossel, M. Reich *et al.*, "Validation of hybrid battery concepts with solid electrolyte membranes – Interface ion transfer kinetics measured by 4-point impedance," to be submitted in *The Journal of Physical Chemistry C*, 2014.
- [104] R. Shannon, "Revised effective ionic radii and systematic studies of interatomic distances in halides and chalcogenides," *Acta Crystallographica Section A*, vol. 32, pp. 751-767, 1976.

-
- [105] J. Awaka, N. Kijima, Y. Takahashi *et al.*, "Synthesis and crystallographic studies of garnet-related lithium-ion conductors $\text{Li}_6\text{CaLa}_2\text{Ta}_2\text{O}_{12}$ and $\text{Li}_6\text{BaLa}_2\text{Ta}_2\text{O}_{12}$," *Solid State Ionics*, vol. 180, pp. 602-606, 2009.
- [106] A. Peters, C. Korte, D. Hesse *et al.*, "Ionic conductivity and activation energy for oxygen ion transport in superlattices - The multilayer system CSZ (ZrO_2+CaO)/ Al_2O_3 ," *Solid State Ionics*, vol. 178, pp. 67-76, 2007.
- [107] C. Korte, A. Peters, J. Janek *et al.*, "Ionic conductivity and activation energy for oxygen ion transport in superlattices - the semicoherent multilayer system YSZ ($\text{ZrO}_2+9.5 \text{ mol\% Y}_2\text{O}_3$)/ Y_2O_3 ," *Physical Chemistry Chemical Physics*, vol. 10, pp. 4623-4635, 2008.
- [108] N. Schichtel, C. Korte, D. Hesse *et al.*, "Elastic strain at interfaces and its influence on ionic conductivity in nanoscaled solid electrolyte thin films-theoretical considerations and experimental studies," *Physical Chemistry Chemical Physics*, vol. 11, pp. 3043-3048, 2009.
- [109] N. Schichtel, C. Korte, D. Hesse *et al.*, "On the influence of strain on ion transport: microstructure and ionic conductivity of nanoscale YSZ/ Sc_2O_3 multilayers," *Physical Chemistry Chemical Physics*, vol. 12, pp. 14596-14608, 2010.
- [110] H. Aydin, C. Korte, and J. Janek, " O^{18} -tracer diffusion along nanoscaled Sc_2O_3 /yttria stabilized zirconia (YSZ) multilayers: on the influence of strain," *Science and Technology of Advanced Materials*, vol. 14, 2013.
- [111] H. Aydin, C. Korte, M. Rohnke *et al.*, "Oxygen tracer diffusion along interfaces of strained Y_2O_3 /YSZ multilayers," *Physical Chemistry Chemical Physics*, vol. 15, pp. 1944-1955, 2013.
- [112] C. Korte, "Zur Wechselwirkung von Ionentransport und Mikrostruktur in inneren Grenzflächen," Habilitationsschrift, Gießen, 2008.
- [113] M. H. Hebb, "Electrical conductivity of silver sulfide," *Journal of Chemical Physics*, vol. 20, pp. 185-190, 1952.
- [114] C. Wagner, "Investigations on Silver Sulfide," *Journal of Chemical Physics*, vol. 21, pp. 1819-1827, 1953.
- [115] D. Mazza, "Remarks on a ternary phase in the $\text{La}_2\text{O}_3\text{-Me}_2\text{O}_5\text{-Li}_2\text{O}$ system ($\text{Me}=\text{Nb, Ta}$)," *Materials Letters*, vol. 7, pp. 205-207, 1988.
- [116] Y. X. Wang, and W. Lai, "High ionic conductivity lithium garnet oxides of $\text{Li}_{7-x}\text{La}_3\text{Zr}_{2-x}\text{Ta}_x\text{O}_{12}$ compositions," *Electrochemical and Solid State Letters*, vol. 15, , pp. A68-A71, 2012.
- [117] L. Vegard, "Die Konstitution der Mischkristalle und die Raumfüllung der Atome," *Zeitschrift für Physik*, vol. 5, pp. 17-26, 1921.

- [118] R. Murugan, V. Thangadurai, and W. Weppner, "Fast lithium ion conduction in garnet-type $\text{Li}_7\text{La}_3\text{Zr}_2\text{O}_{12}$," *Angewandte Chemie-International Edition*, vol. 46, pp. 7778-7781, 2007.
- [119] R. Murugan, V. Thangadurai, and W. Weppner, "Lithium ion conductivity of $\text{Li}_{5+x}\text{Ba}_x\text{La}_{3-x}\text{Ta}_2\text{O}_{12}$ ($x=0-2$) with garnet-related structure in dependence of the barium content," *Ionics*, vol. 13, pp. 195-203, 2007.

8. Appendix

8.1 List of abbreviations

(X Y) $\times n$	Multilayer thin film with alternating layers of material X and Y; n indicates the amount of deposited bilayers.
AAO	Anodized aluminum oxide
ac	Alternating current
CAD	Computer-aided design
CMK-3	Carbon mesostructures at Korea Advanced Institute of Science and Technology number 3
CVD	Chemical vapor deposition
dc	Direct current
DME	1,2-dimethoxyethane
DOL	1,3-dioxolane
E_a	Activation energy of charge transfer
EDX	Energy dispersive x-ray spectroscopy
EIS	Electrochemical impedance spectroscopy
ESB	Energy selective backscatter detector
FIB	Focused ion beam
GGG	Gallium gadolinium garnet – $\text{Ga}_3\text{Gd}_5\text{O}_{12}$
HRSEM	High resolution scanning electron microscopy
Inlens	Inlens detector

IR	Infrared
ITO	Indium tin oxide
LATP	Lithium aluminum titanium phosphate – a NASICON-type electrolyte
LBLTO	$\text{Li}_6\text{BaLa}_2\text{Ta}_2\text{O}_{12}$ – garnet-type electrolyte
LLZTO	$\text{Li}_{6.5}\text{La}_3\text{Zr}_{1.5}\text{Ta}_{0.5}\text{O}_{12}:\text{Al}_2\text{O}_3$
LLZGO	$\text{Li}_7\text{La}_3\text{Zr}_2\text{O}_{12}:\text{Ga}_2\text{O}_3$
LFP	LiFePO_4 – a positive electrode material
Li-O ₂	Lithium-oxygen galvanic cell
“LiPON”	nitrogen doped glassy Li_3PO_4
Li-S	Lithium-sulfur galvanic cell
LISICON	Lithium super ionic conductor
“LiSON”	Nitrogen doped glassy Li_2SO_4
LiTFSI	Lithium bis(trifluoromethanesulfonyl)imide
LLT	$\text{Li}_{3x}\text{La}_{2/3x}\text{TiO}_3$ – a perovskite-type electrolyte
LLZGO	Cubic $\text{Li}_7\text{La}_3\text{Zr}_2\text{O}_{12}$ stabilized by addition of Ga_2O_3
LLZTO	$\text{Li}_{7-x}\text{La}_3\text{Zr}_{2-x}\text{Ta}_x\text{O}_{12}$ stabilized by addition of Al_2O_3
MS	Magnetron sputtering
NASICON	Sodium super ionic conductor
PA	Post anneal
PLD	Pulsed laser deposition
Pt100	Thin film resistance thermometer

PTFE	Polytetrafluoroethylene
rf	Radio frequency
RT	Room temperature
S	Sputter deposition
SE2	Secondary electron detector
SEM	Scanning electron microscopy
TE	Thermal evaporation
TEM	Transmission electron microscopy
thio-LISICON	LISICON-type electrolyte in which oxygen is replaced by sulfur
XRD	X-ray diffraction

8.2 List of symbols

(RQ)	A resistance parallel to a constant phase element
$(RQ)C$	A resistance parallel to a constant phase element in series to a capacity
\square	Vacancy in the chemical Formula of the perovskite $\text{Li}_{3x}\text{La}_{2/3x}\square_{1/3-2x}\text{TiO}_3$.
μ	Mobility of species
A	Area
a	<ul style="list-style-type: none"> • Lattice constant • Exponent of constant phase element
C	Capacity

c	Concentration
d	Thickness
ΔG	Gibbs free energy
E	Electromotive force
F	Faraday constant
h	Electron hole
I	Current
j	Current density
l	Distance (between electrodes)
n_i	Amount of a species
P	Electrical power
Q	Constant phase element
R	Ohmic resistance
σ	Conductivity
θ	Scattering angle
T	Temperature in K
t	Time
g	Temperature in °C
τ	Time constant (impedance)
U	Voltage
V	Vacancy in Kröger-Vink notation

x	Variable for amount of a chemical species in sum formula
z	Elementary charge

8.3 List of peer-reviewed publications

- Reinacher, J.; Berendts, S.; Janek, J., Preparation and electrical properties of garnet-type $\text{Li}_6\text{BaLa}_2\text{Ta}_2\text{O}_{12}$ lithium solid electrolyte thin films prepared by pulsed laser deposition. *Solid State Ionics* 2014, 258, 1-7.
- Reitz, C.; Reinacher, J.; Hartmann, P.; Brezesinski, T., Polymer-templated ordered large-pore mesoporous anatase–rutile $\text{TiO}_2\text{:Ta}$ nanocomposite films: Microstructure, electrical conductivity, and photocatalytic and photoelectrochemical properties. *Catalysis Today* 2014, 225, 55-63.
- Yuan, J.; Garcia Marquez, A.; Reinacher, J.; Giordano, C.; Janek, J.; Antonietti, M., Nitrogen-doped carbon fibers and membranes by carbonization of electrospun poly(ionic liquid)s. *Polymer Chemistry* 2011, 2, 1654-1657.
- Lee, D.-K.; Fischer, C. C.; Valov, I.; Reinacher, J.; Stork, A.; Lerch, M.; Janek, J., An EMF cell with a nitrogen solid electrolyte-on the transference of nitrogen ions in yttria-stabilized zirconia. *Physical Chemistry Chemical Physics* 2011, 13, 1239-1242.

Declaration

Ich erkläre: Ich habe die vorgelegte Dissertation selbständig und ohne unerlaubte fremde Hilfe und nur mit den Hilfen angefertigt, die ich in der Dissertation angegeben habe. Alle Textstellen, die wörtlich oder sinngemäß aus veröffentlichten Schriften entnommen sind, und alle Angaben, die auf mündlichen Auskünften beruhen, sind als solche kenntlich gemacht. Bei den von mir durchgeführten und in der Dissertation erwähnten Untersuchungen habe ich die Grundsätze guter wissenschaftlicher Praxis, wie sie in der „Satzung der Justus-Liebig-Universität Gießen zur Sicherung guter wissenschaftlicher Praxis“ niedergelegt sind, eingehalten.